Validation and Assimilation of Aeolus Wind Observations

Anne Martin

Munich - 2023

Validation and Assimilation of Aeolus Wind Observations

Anne Martin

Dissertation
an der Fakultät für Physik
der Ludwig–Maximilians–Universität
München

vorgelegt von
Anne Martin
aus Wangen im Allgäu

München, 11. Januar, 2023

Erstgutachter: Prof. Dr. Martin Weissmann
Zweitgutachter: Prof. Dr. George Craig
Datum der Abgabe: 11. Januar, 2023
Datum der mündlichen Prüfung: 27. Februar, 2023

Parts of this thesis are included in (see Appendix A):

Martin, A, M. Weissmann, and O. Reitebuch, and M. Rennie, and A. Geiß, and A. Cress 2021: Validation of Aeolus winds using radiosonde observations and numerical weather prediction model equivalents. *Atmospheric Measurement Techniques*; 14: 2167–2183. https://doi.org/10.5194/amt-14-2167-2021

Martin, A, M. Weissmann, and A. Cress 2022: Impact of assimilating Aeolus observations in the global model ICON: A global statistical overview. *Quarterly Journal of the Royal Meteorological Society*; (submitted)

Martin, A, M. Weissmann, and A. Cress 2022: Investigation of links between dynamical scenarios and particularly high impact of Aeolus on NWP forecasts. *Weather and Climate Dynamics Discussions*; https://doi.org/10.5194/egusphere-2022-1150 (preprint)

Zusammenfassung

Neben wissenschaftlichen und technologischen Fortschritten war die Weiterentwicklung des globalen Beobachtungssystems einer der wichtigsten Faktoren, die in den letzten Jahren zur Verbesserung der numerischen Wettervorhersage (engl. Numerical Weather Prediction, kurz NWP) beigetragen haben. Die Anfangsbedingungen einer Vorhersage werden in der Regel durch Datenassimilationssysteme bereitgestellt, wobei die neuste Kurzfristvorhersage mit einer Auswahl atmosphärischer Beobachtungen kombiniert wird. Das Fehlen globaler Windprofilbeobachtungen stellt derzeit eine der größten Einschränkungen in der meteorologischen Datenassimilation dar; insbesondere in Regionen und für räumliche Skalen, in denen eine schwache geostrophische Masse-Wind-Kopplung vorherrscht. Die Doppler Wind Lidar (DWL) Satellitenmission Aeolus der Europäischen Weltraumorganisation (engl. European Space Agency, kurz ESA) liefert einen neuartigen Datensatz von Windprofilen mit quasi-globaler Abdeckung, der diese Datenlücke im aktuellen globalen Beobachtungssystem schließen soll. Ziel dieser Arbeit ist es, den Einfluss der Aeolus Beobachtungen auf die numerische Wettervorhersage abzuschätzen und somit den potenziellen Nutzen von derartigen satellitengestützten DWL-Missionen zu demonstrieren.

Eine entscheidende Voraussetzung für die Verwendung meteorologischer Beobachtungen in NWP-Datenassimilationssystemen ist die Kenntnis und Charakterisierung ihrer Fehler. Daher wird im ersten Teil dieser Arbeit eine Validierungsstudie zur Untersuchung der Qualität der Aeolus Windprofile durchgeführt. Hierbei ermöglichen Vergleiche mit drei unabhängigen Referenzdatensätzen - kollokierte Radiosonden Beobachtungen sowie Modelläquivalente des globalen ICOsahedral Nonhydrostatic (ICON) Modells des Deutschen Wetterdienstes (DWD) und des Integrated Forecast System (IFS) Modells des Europäischen Zentrums für mittelfristige Wettervorhersage (ECMWF) - eine umfassende Abschätzung der systematischen und zufälligen Fehler der Aeolus Beobachtungen. Darüber hinaus werden die systematischen Fehler auf ihre Abhängigkeiten hin untersucht und Korrekturansätze getestet, die in Datenassimilationssystemen im Rahmen der Qualitätskontrolle eingesetzt werden können. Abweichungen zwischen den Radiosonden- und modellbasierten Validierungsergebnissen, die bei der Bestimmung des zufälligen Fehlers auftreten, sind hauptsächlich auf Unterschiede der räumlichen und zeitlichen Repräsentativität zurückzuführen. Die einzelnen Komponenten des Repräsentativitätsfehler können mithilfe von hochauflösenden regionalen Modellsimulationen abgeschätzt werden und somit bei der Ermittlung des Aeolus Instrumentenfehlers berücksichtigt werden. Die Ergebnisse liefern wichtige Informationen über das Ausmaß und die vertikale Struktur des Rayleigh- und Mie-Windfehlers von Aeolus, die als Grundlage für den zugewiesenen Beobachtungsfehler bei der Datenassimilation dienen.

Der zweite Teil dieser Arbeit untersucht, inwiefern die numerische Wettervorhersage von der Assimilation der neuartigen DWL-Beobachtungen des Aeolus Satelliten profitiert. Dazu wird ein Beobachtungssystem Experiment basierend auf dem operationellen globalen Assimilationssystem ICON am DWD mit und ohne Assimilation von Aeolus Beobachtungen analysiert. Neben globalen Statistiken werden Regionen und Zeiträume mit besonders ausgeprägtem Einfluss genauer betrachtet, um die dynamischen Prozesse, die dem insgesamt positiven Einfluss zugrunde liegen, zu verstehen. Die größten Auswirkungen der Assimilation von Aeolus Beobachtungen treten in der 2-3-tägigen Wind- und Temperaturvorhersage in der tropischen oberen Troposphäre und unteren Stratosphäre sowie in der südlichen Hemisphäre auf. Der Einfluss der Aeolus Beobachtungen auf der Nordhalbkugel ist weniger ausgeprägt, aber im Vergleich zu anderen Beobachtungssystemen immer noch relativ groß. Diese Dissertation bespricht drei Beispiele atmosphärischer Phänomene, welche dynamische Szenarien für eine signifikante Reduzierung von Vorhersagefehlern darstellen: Der Wechsel der Oszillationsphase zweier großräumiger tropischer Zirkulationssysteme - der quasi-zweijährige Schwingung (engl. Quasi-Biennial Oscillation, kurz QBO) und der El Niño-Southern Oscillation (ENSO) - und die Wechselwirkung von tropischen Wirbelstürmen, die einen extratropischen Übergang durchlaufen und dabei mit dem Wellenleiter der mittleren Breiten interagieren. Die gefundenen Hinweise auf dynamische Veränderungen und Prozesse im Zusammenhang mit dem besonders hohen Einfluss von Aeolus auf die numerische Wettervorhersage liefern wichtige Informationen für die Weiterentwicklung von Beobachtungs- und NWP-Systemen und werden als Grundlage für zukünftige Studien über Möglichkeiten zur Verbesserung von NWP Vorhersagen durch zusätzliche Beobachtungen dienen.

Abstract

Along with scientific and technological developments, the advancement of the Global Observing System (GOS) has been one of the most important factors contributing to the increase in numerical weather forecasting (NWP) skill in recent years. The initial conditions of a forecast are provided by data assimilation systems, combining the latest short-range forecast with a selection of atmospheric observations. One of the current major limitations is the lack of global wind profile observations, particularly in regions and for spatial scales where geostrophic mass-wind coupling is weak. The European Space Agency's (ESA) Doppler Wind Lidar (DWL) satellite mission Aeolus provides a novel data set of wind profiles with quasi-global coverage intended to fill this gap in the GOS. This thesis aims to assess the impact of the Aeolus observations in NWP to demonstrate the potential value of such satellite-based DWL missions.

A crucial prerequisite for using meteorological observations in NWP data assimilation systems is the knowledge and characterization of their errors. Therefore, in the first part of this work, a validation study is conducted to investigate the quality of the Aeolus wind profiles. Comparisons with three independent reference data sets - collocated radiosonde observations as well as model equivalents of the global ICOsahedral Nonhydrostatic (ICON) model of the German Weather Service (DWD) and the Integrated Forecast System (IFS) model of the European Centre for Medium-Range Weather Forecasts (ECMWF) - enable a comprehensive estimation of the systematic and random errors of the Aeolus observations. In addition, the systematic errors are examined for their dependencies, and correction approaches that can be used in data assimilation systems as part of quality control are tested. Discrepancies between the radiosonde and model-based validation results that occur in determining the random error are mainly due to differences in spatial and temporal representativeness. The representativeness error components can be estimated using high-resolution regional model simulations and thus can be taken into account in determining the Aeolus observational error. The results provide important information on the magnitude and vertical structure of the Aeolus Rayleigh and Mie wind error, which serves as the basis for the assigned observational error in the data assimilation.

The second part of this thesis examines how numerical weather forecasting benefits from the assimilation of the novel DWL observations from the Aeolus satellite. For this purpose, an Observing System Experiment (OSE) based on the operational global assimilation system of ICON at DWD with and without the assimilation of Aeolus observations is analyzed. Besides global impact statistics, regions and periods with particularly pronounced impact are investigated further to understand the underlying dynamics leading to the overall beneficial impact. The largest impact of assimilating Aeolus observations occurs in the 2-3 day wind and temperature forecast in the tropical upper troposphere and lower stratosphere and in the Southern Hemisphere. The influence of the Aeolus observations in the Northern

Hemisphere is less pronounced but still relatively large compared to other observing systems. Furthermore, this thesis illustrates three examples of atmospheric phenomena that constitute dynamical scenarios for significant forecast error reduction: the change of the oscillatory phase of two large-scale tropical circulation systems - the quasi-biennial oscillation (QBO) and the El Niño–Southern Oscillation (ENSO) - and the interaction of tropical cyclones undergoing extratropical transition (ET) with the midlatitude waveguide. These indications of dynamical changes and processes related to the particularly high impact of Aeolus on NWP forecasts provide important information for the advancement of observing and NWP systems and will serve as the basis for future studies on opportunities to improve NWP forecasts by additional observations.

Contents

Chapter 1

Introduction

1.1 State of the art

1.1.1 Importance of atmospheric wind observations for NWP

Along with temperature, pressure, and humidity, wind is one of the fundamental variables that describe the physical state of the atmosphere. A familiar characteristic of winds is that they change from hour to hour, day to day, and from place to place. This variability on a wide range of temporal and spatial scales associated with weather systems, storms, or fronts is of great importance for meteorological forecasting (Goody and Walker, 1972). The average overall structure of large-scale atmospheric motion is usually defined as the general circulation. It results from the differential solar heating between the equatorial regions and the poles in conjunction with the Earth's rotation. Due to mutual interactions, the general circulation is closely related to variable winds on smaller scales. Variations in small-scale atmospheric phenomena can significantly change the average flow pattern, mainly associated with the evolution of atmospheric waves. On the other hand, there are a variety of stationary or seasonal wind systems on Earth that can affect the small-scale weather pattern. In the following, an overview of the main wind-driven dynamical processes in the atmosphere is first given to illustrate the general importance of wind observations. Then, the role and need for direct wind field information in Numerical weather prediction (NWP) are discussed.

Atmospheric wind-driven dynamical processes

In the tropics, seasonally varying monsoon circulations play an important role in the annual evolution of precipitation and temperature patterns. The major monsoon systems around the equator are the Indian, East Asian, and West African Monsoons, which are associated with the latitudinal variation of the Intertropical Convergence Zone (ITCZ). Their variability may be significantly related to jet streams such as the Tropical Easterly Jet (TEJ) in the upper troposphere and the mid-level African Easterly Jet (AEJ). Furthermore, one of the main sources of tropical predictability on the weekly to monthly time scale is the intraseasonal wave-like convective system Madden-Julian Oscillation (MJO). Besides the tropics, the MJO can also impact the weather in the extratropics by inducing Rossby waves. Another central teleconnection system on the interannual time scale is the El Niño-Southern Oscillation (ENSO). It manifests as changes in the east-west circulation over the tropical

Pacific Ocean and leads to large-scale redistribution in oceanic temperature precipitation patterns. The shift in the ENSO conditions is associated with a major change in the wind patterns and can affect the extratropics through various tropospheric and stratospheric pathways. In the stratospheric layer around the equator, the two- to three-year cycle in downward propagating zonal wind, referred to as the Quasi-Biennial Oscillation (QBO), is an essential interacting circulation system. It is suggested that wave-mean flow interactions of upward propagating waves from the troposphere drive this large-scale circulation. Both the ENSO and the QBO can potentially impact the variability of the Indian Monsoon and the activity of tropical cyclones. The QBO is also important for the dynamics in the polar regions due to teleconnections via the global stratospheric circulation.

The extratropics are generally dominated by a westerly flow. Within the westerly tropospheric jets, large-scale turbulent disturbance movements can occur, controlling the high and low pressure systems in the middle latitudes. These disturbances are essentially planetary Rossby waves that are mainly forced by momentum due to interactions with orography like the Rocky Mountains or the Himalayas, irregularities in the temperature and pressure gradient, or interactions with smaller-scale dynamical systems. The meandering air currents tend to move eastward, which is associated with the formation of cyclogenesis and anticyclogenesis downstream. Furthermore, Rossby waves can also control the track of high and low pressure systems at the Earth's surface. They are instrumental in transporting heat from the tropics to the poles and cold air to the tropics to return the atmosphere to balance.

The significant steering influences of the general atmospheric circulation on weather changes of different magnitudes can become very severe and have consequences for the population. Therefore, it is particularly necessary to observe the large-scale flow. In addition, observations of the wind field in regions of rapid changes in wind, such as in frontal zones or during the development stages of storm systems, are of great importance. Such wind systems typically influence the occurrence and distribution of extensive precipitation. Because the associated wind shear occurs both horizontally and vertically, leading to interactions and couplings with the jet stream, densely distributed information on profiles of wind speed and direction is essential.

The need for wind observations for Numerical Weather Prediction

Numerical weather prediction is based on computational models that describe the main physical processes in the atmosphere and their effects on the time evolution of the model variables, such as temperature, pressure, wind, and humidity. They consist of a set of discretized flow equations based on the conservation of momentum, mass, and energy. Furthermore, parameterization schemes are used to approximate the impact of small-scale structures that cannot be explicitly represented on the model grid. The initial state from which an NWP model is run is called the analysis and is the "best" estimate of the current atmospheric state in the given model space. From this, the prediction of a future state is derived through numerical integration. Since the atmosphere is a non-linear, chaotic system (Lorenz, 1963), the forecast quality depends strongly on the accuracy of the initial state. The concept that determines the best estimate of the initial state by combining a background forecast with the collection of atmospheric observations weighted by their errors is termed data assimilation.

Over the past 40 years, NWP skill has steadily improved. Fig. 1.1 shows that the forecast skill in the range from 3 to 10 days has increased by about one day per decade (Bauer et al., 2015). Besides scientific and technological developments, one of the major contributing factors is the increase in observational information and its effective use. Particularly, the advanced operational assimilation of satellite observations since the 1990s shows beneficial impact (Eyre et al., 2020). Due to the global coverage provided by satellites, the forecast skill of the Northern and Southern Hemispheres has been increasingly converging. However, despite these advances in the observing system in recent years, data assimilation is still a highly under-determined problem. The degrees of freedom in current NWP models are typically a factor of ten larger than the number of available observations. Moreover, the measured variables are not always directly related to the basic variables of the model, and their partitioning is strongly biased toward mass-based observations. In particular, the lack of direct wind observations is a major challenge for NWP.

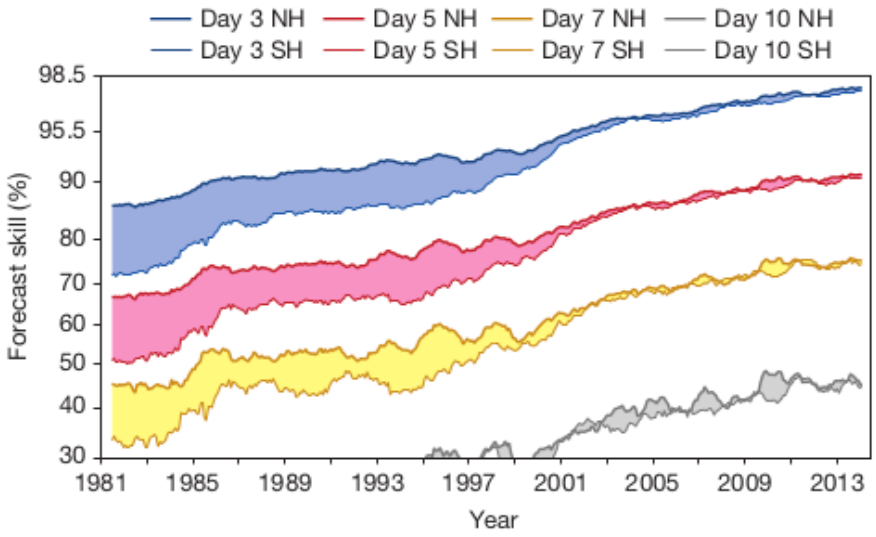

Figure 1.1: *Anomaly correlation between the 500-hPa geopotential height forecasts (three-, five-, seven- and ten-day) and the verifying analysis, with respect to the climatology as a measure for forecast skill [%]. Shown for the extratropical Northern and Southern Hemispheres as a running mean from 1981 to 2014. From Bauer et al. (2015).*

In the absence of direct wind observations, typically, the geostrophic adjustment theory is used to indirectly derive some information about the large-scale wind field from observations of temperature and pressure. However, this theory is limited to a certain extent. To illustrate the relative importance of directly measured wind data, the definition of the Rossby radius of deformation is useful. It describes the horizontal length scale at which the wind and mass field are approximately in geostrophic balance. Simplified, the Rossby radius of deformation R can be expressed as:

$$R = \frac{\sqrt{gh}}{f} = \frac{\sqrt{gh}}{2\Omega sin(\Phi)}, \tag{1.1}$$

with g being the gravitational acceleration and h being the vertical scale of an atmospheric motion system. The denominator represents the Coriolis parameter f with Ω being the Earth's angular velocity and Φ being the latitude. At horizontal length scales smaller

than R, the mass field adjusts to equilibrium with the wind field. At horizontal length scales larger than R, the large-scale wind field can only be derived from the mass field information with reasonable accuracy. Close to the equator, where the Coriolis parameter converges to zero, R goes to infinity. There, the coupling between mass and wind is mainly determined by atmospheric wave features rather than geostrophic balance. In addition to latitude, the geostrophic mass-wind coupling also depends on the spatial scales, which is illustrated for the extratropics in Fig. 1.2. The wind field primarily dominates horizontally small-scale (L $\ll$ R) and vertically deep structures (large h), shown as the open white area. This corresponds mainly to orographically determined flow features or circulation systems, such as fronts at higher latitudes. In summary, for NWP, direct information on the wind field is particularly important for determining tropical dynamics at all scales as well as smaller-scale structures at higher latitudes.

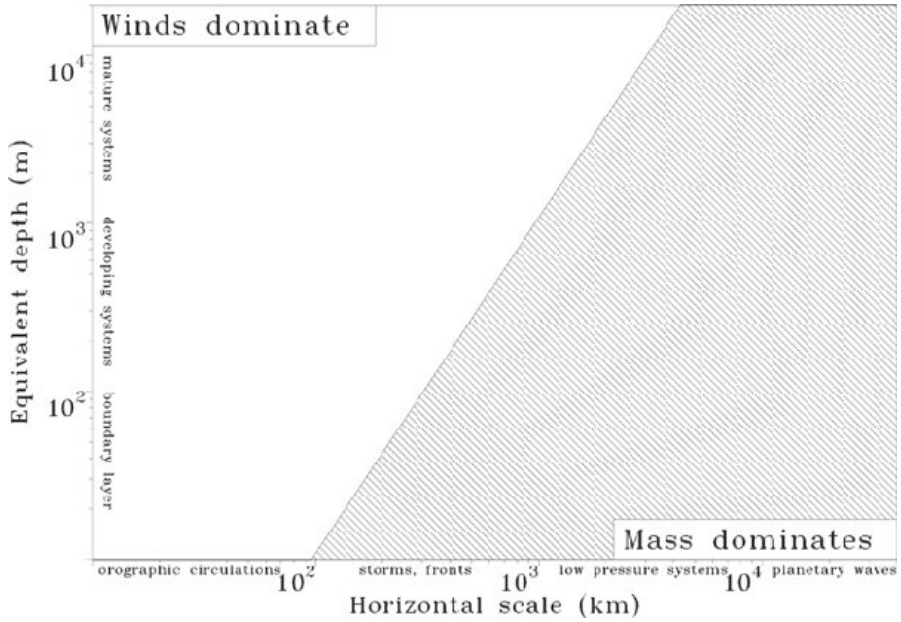

Figure 1.2: *The straight diagonal line represents the Rossby radius of deformation (R) for a latitude of $\Phi = 45°$ as a function of the horizontal and vertical scale. It separates the range within the wind field dominates (open white area), and the range within the mass field dominates (shaded grey area). From ESA (1999).*

1.1.2 Deficiencies in the global observing system

The Global Observing System (GOS), coordinated by the World Meteorological Organization (WMO), consists of a wide variety of observation methods that provide routinely available data for NWP data assimilation. The types of currently used wind observations can be roughly grouped into single-level surface, single-level upper-air, and multi-level upper-air data. They are described below, along with their individual deficiencies. Overall, the most significant limitation is the lack of availability of direct wind data on a global scale.

Information on surface winds is relatively abundant over both land, and the oceans, e.g., scatterometer wind vectors from satellites, synoptic wind reports from land stations and ships or moored and drifting buoys. However, none of these observations can provide

crucial information about the vertical profile of atmospheric winds.

(a) AMV winds

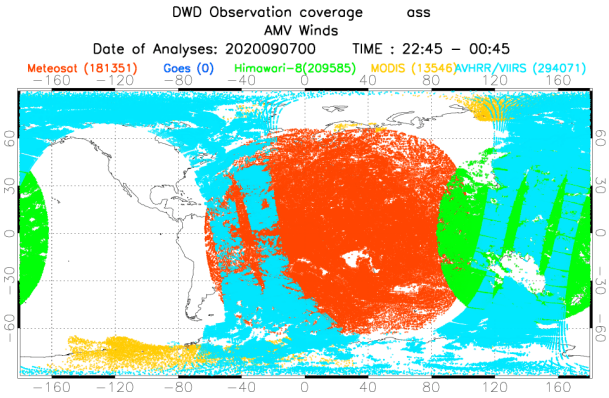

(b) Aircraft observations

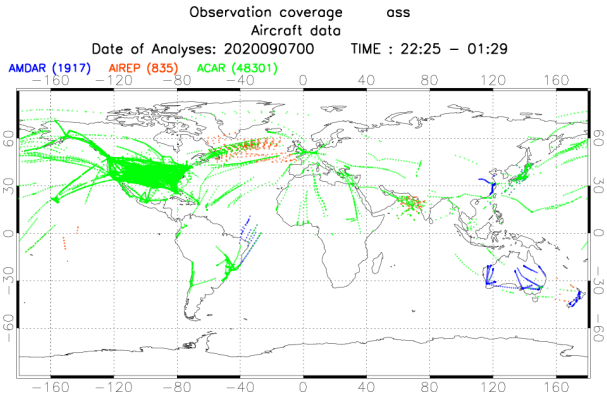

(c) Radiosonde observations

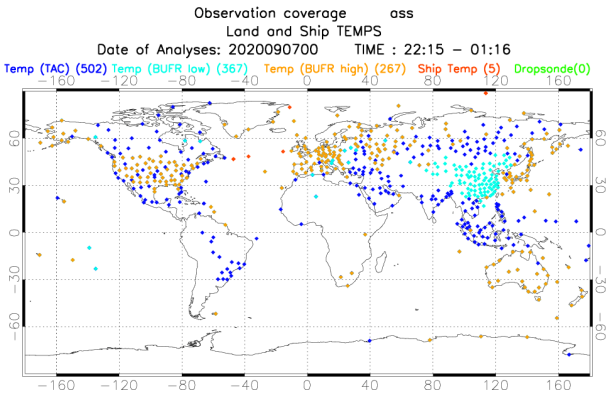

(d) ATOVS radiances

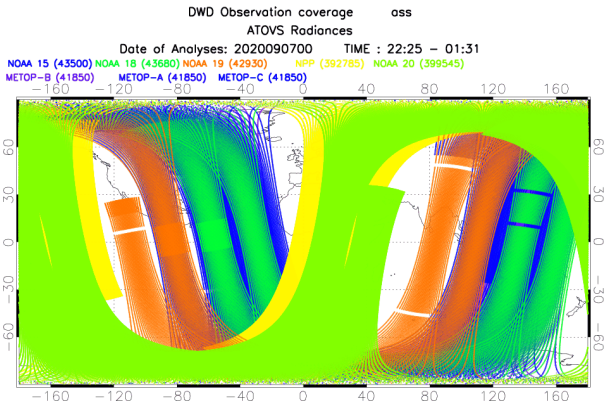

Figure 1.3: *Geographical data coverage of the observations assimilated at DWD: (a) AMV winds, (b) aircraft observations, (c) radiosonde observations, and (d) observations of radiances from satellites using the instrument ATOVS. The coverage is valid for 07 September 2020 00 UTC (± 1.5 h). From* `https://rcccm.dwd.de/DE/leistungen/nwv_obsloc/nwv_obsloc.html`

Atmospheric motion vectors (AMVs) derived from tracking cloud and water vapor structures in geostationary or polar orbiting satellite imagery observe the wind field in upper-air single-levels with nearly global coverage (Fig. 1.3a). At Deutscher Wetterdienst (DWD), every 6 h, about 500.000 observations of AMVs are available. However, due to several error sources, the amount of AMV observations actually used in NWP is much lower. AMVs exhibit deficiencies because of the assumption that the tracked features are advected by the atmospheric flow, which does not always have to be true. Furthermore, uncertainties of their height assignment can lead to significant systematic and correlated errors (Folger and Weissmann, 2014). Another mainly single-level observation type is wind reports from aircraft. They can only provide information about the vertical atmospheric structure during ascents and descents. The observations are very accurate, but the coverage is insufficient since most of the data is available at cruise level along the main air traffic routes (Fig. 1.3b).

The primary source of accurate vertical profiles of the wind field are radiosondes, pilot balloons, or radar wind profilers. However, predominantly, they are concentrated over

continents in the Northern Hemisphere (Fig. 1.3c). Only a few profiles are available over the oceans or the Southern Hemisphere.

The largest proportion of assimilated global observations consists of microwave and infrared radiance data from satellite sounders. An example of the spatial (and temporal) coverage of the Advanced TIROS (Television Infra-red Observing System) Operational Vertical Sounder (ATOVS) is shown in Fig. 1.3d with a million observations within 3 h. However, they mainly provide information on the atmospheric mass field in terms of temperature or humidity. This poses a particularly strong restriction for regions of weak geostrophic balance.

Fig. 1.4 shows the proportion of all active observations (used in the assimilation) in the global model at DWD for a 24-h period in 2022. It can be seen that the radiances clearly dominate the observing system, accounting for ∼64% of the total observations. Winds from scatterometers, satellite imagery, and GNSS signals together constitute about 18%. Conventional observations from aircraft reports, radiosondes, surface stations, buoys, pilot, and wind profilers represent ∼7% of the total number of observations. The proportion of assimilated wind profiles from the spaceborne lidar of the Aeolus mission is about 2%.

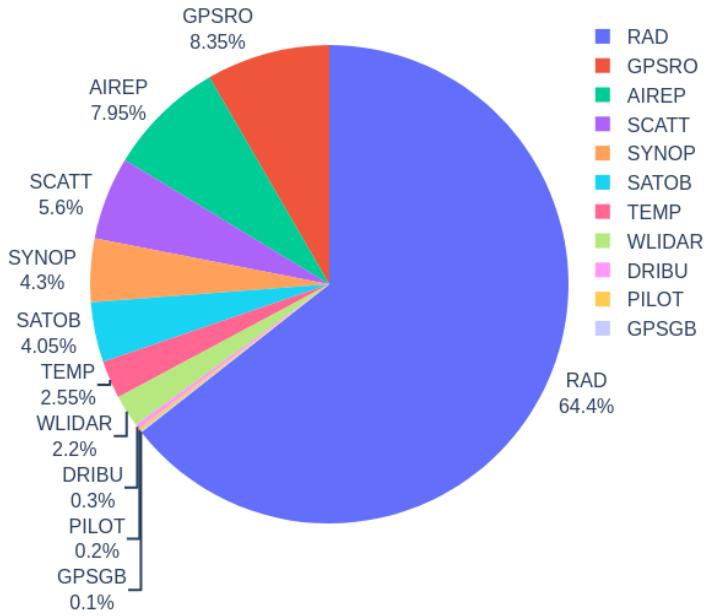

Figure 1.4: *Percentage of the total number of assimilated observations in the global ICON model at DWD for a 24-h period from 15 July 2022 (3 h assimilation window). The numbers in brackets in the following description of the acronyms are the total numbers of assimilated observations. RAD = satellite radiances (polar orbit + geostationary) (3.571.007), GPSRO = GNSS Radio Occultation (444.121), AIREP = aircrafts (AIREP, AMDAR, ACARS) (420.178), SCATT = scatterometer and alimeter (294.945), SYNOP = synoptic wind reports from land stations and ships (227.444), SATOB = satellite winds (AMVs) (215308), TEMP = radiosondes (134.941), WLIDAR = ADM Aeolus winds (116.387), DRIBU = buoys (15.315), PILOT = pilot and wind profiler (10.610), GPSGB = GNSS ground-based wind observations (7.458).*

1.1.3 Wind profile observations from space - historical scientific and technological background

Already in 1995, space programs recognized that an Atmospheric Dynamics Mission (ADM) would be needed to meet the requirements of the current GOS and the Global Climate Observing System (GCOS) (ESA, 1995). Potential ways to measure wind profiles globally from space have been extensively studied since the 1970s. In the 1980s, the first basic concepts for an operational space-based facility, a Laser Atmospheric Wind Sounder (LAWS, (Baker et al., 1995)), were defined and designed by the National Aeronautics and Space Administration (NASA). However, it turned out that bringing such wind vector observing systems into space would be extremely complex. Inspired by the LAWS concept, in 1989, the European Space Agency (ESA) published its first report concerning a Doppler Wind Lidar (DWL) providing single-component wind Line-of-sight (LOS) measurements (ESA, 1989). Lorenc et al. (1992) showed that the assimilation of a single horizontal line-of-sight (HLOS) wind component relative to an instrument line-of-sight (LOS) direction can improve forecasting skills significantly.

Several early scientific studies (e.g., Courtier et al. (1992), Lorenc et al. (1992)) supported the basic hypothesis that DWL information positively impacts data assimilation systems used for NWP, which led to the foundation for a DWL-ADM mission. Over the years, global atmospheric measurements of wind profiles and, thus, the mission gained increasing importance. In the sixth edition of the guide to meteorological instruments and methods of observation 1996, the WMO gave top priority to wind profile measurements and stated that the "realization of their requirements would represent a major step forward in improving the quality of atmospheric flow analyses" (WMO, 1996). In addition, they noted that global wind profiles are "essential for operational weather forecasting at all scales and latitudes" (WMO, 1996, Chapter 3 p.295) and emphasized the impeding progress due to the deficiencies in the current GOS and GCOS (WMO, 1998). Finally, in 1999, the now-called ADM-Aeolus mission was selected to be one of ESA's Earth Explorer Core missions as part of the Living Planet Program to observe Earth's winds from space. The development of satellite-based wind profile systems has become a priority for the future GOS. In WMO (2012), it was stated that the current GOS is too much geared towards measuring atmospheric mass, particularly satellite instruments, even though the average impact of wind observations is higher both on a single instrument and on a 'per observation' basis.

In parallel with the mission's technical development, scientific and campaign activities were carried out to evaluate the potential of ADM-Aeolus observations for NWP. The importance of wind profile observations for medium-range forecast quality over Europe has been motivated by Cress and Wergen (2001). They performed observing system experiments (OSEs) by withholding existing wind profile observations over North America, demonstrating a significant impact on the forecast quality over Europe after 11 days of assimilation. Žagar et al. (2004a) and Žagar et al. (2004b) emphasized the importance of an appropriate mass–wind relationship in the tropics, showing that direct wind measurements are much more efficient in reconstructing the structure of equatorial waves than mass field observations. Further comparisons between assimilating mass and wind field data from Horányi et al. (2015a) showed that large improvements from the Aeolus observations are mainly to be expected in the upper troposphere and lower stratosphere. Adding simulated

ADM Aeolus-like lidar observations to the GOS has been found to be beneficial for NWP by several studies (e.g., Marseille et al. (2008b), Stoffelen et al. (2006), Tan et al. (2007), Žagar (2004)). Particularly, these studies demonstrated a reduction in forecast errors for poorly predicted severe events (Marseille et al., 2008b,a), in the 500 hPa average medium-range wind forecast over the Northern Hemisphere (Stoffelen et al., 2006), for the analysis and forecasts over oceans (Tan et al., 2007) and for tropical wave dynamics (Žagar, 2004). In addition to the usefulness of Aeolus DWL HLOS wind data, the sensitivity of forecast quality with respect to random and systematic errors in HLOS wind measurements was addressed. Horányi et al. (2015b) showed that increased systematic errors (even small biases of the order of 1 m s^{-}1) can deteriorate the forecast quality and have a much larger influence than random errors. Therefore, they noted that particularly at the equator and top of the atmosphere, where observational biases, but also the impact of Aeolus is expected to be large, biases should be minimized.

In autumn 2003, during the North Atlantic "Observing System Research and Predictability Experiment" (THORPEX) Regional Campaign (A-TReC), the airborne Doppler lidar system of the Deutsches Zentrum für Luft- und Raumfahrt (DLR) onboard of the Falcon research aircraft was used for targeted wind observations. 1612 wind profiles with 5-10 km horizontal and 100 m vertical resolution were measured and compared to 33 side-by-side dropsondes, providing an experimental basis for the deployment of spaceborne DWL systems (Weissmann et al., 2005). A mean standard deviation of the DWL observations of 0.75–1 m s^{-1} was estimated, slightly higher than the general observational error of dropsondes. However, lidar winds are expected to be more representative of model wind fields since the representativeness error (that dominates the total error in data assimilation (Weissmann et al., 2005)) of a line measurement is comparatively small compared to a point measurement (Frehlich and Sharman, 2004). The A-TReC lidar wind profiles were assimilated at the European Centre for Medium-Range Weather Forecasts (ECMWF) to evaluate the impact of the additional measurements above the Atlantic Ocean within a 2-week OSE, including eight flights (Weissmann and Cardinali, 2007). Considering instrumental and representativeness errors, the assigned observation error was assumed to be 1-1.5 m s^{-1}. Since this is smaller than the observation error of most conventional observations in data assimilation at ECMWF, the lidar wind profiles were weighted relatively strongly. Weissmann and Cardinali (2007) found a significant impact on the analyses (40% higher than dropsondes) and on forecasts up to 4 days. On average, the quality of the 48–96-h forecast of 500-hPa over Europe was reduced by 3%. This motivated the use of DWL instruments at research flights during the THORPEX Pacific Asian Regional Campaign (T-PARC) in 2008. For the first time, the development of tropical cyclones was sampled by airborne DWL systems. The wind profile measurements of a three-hour interval covering the early development of the tropical storm Nuri were assimilated into the Weather Research and Forecasting model (WRF), showing improvements in the surface maximum wind forecast and reductions in the track forecast error (Pu et al., 2010). A larger data set of an 11-day period, including 2500 DWL wind profiles during the evolution of Typhoon Sinlaku in the western North Pacific, was obtained from the DWL onboard the DLR Falcon aircraft. The observations were assimilated at ECMWF as well as in the global models of the Naval Research Laboratory (NRL). At ECMWF, the 12–120-h track forecast error was reduced by 9% on average (Weissmann et al., 2012). In addition, the mean quality of the 500- and 1000-hPa geopotential height forecast was increased for both

an area around the recurvature of Sinlaku and an area covering the extratropical transition and interaction with the midlatitude dynamics. The impact was comparable to other aircraft observations but below that of radiosondes, wind profilers, AMVs, SYNOP, and scatterometer surface winds. At NRL, only higher impact was measured from synthetic TC bogus observations, total precipitable water derived from satellites, and Advanced SCATterometer (ASCAT) surface wind data. Even though the ADM-Aeolus winds have larger errors and a lower measurement resolution, the results of Weissmann et al. (2012) indicate that a DWL provides an important source of wind information for NWP, particularly in poorly observed regions during the development of tropical cyclone systems.

Altogether, the research activities of the past few years have been instrumental in understanding the important role that space-based DWL plays for NWP applications and serve as the basis and motivation for the ADM-Aeolus satellite mission.

1.1.4 Aeolus mission objectives

On 22 August 2018, the Aeolus satellite was launched successfully by ESA from the European spaceport in Kourou, French Guiana. Since 3 September 2018, it provides vertical wind profiles with global coverage in Near Real Time. Aeolus is expected to last until 2023, exceeding its nominal 3-year mission lifetime.

The long-term goal is to demonstrate the DWL technique's capability for measuring wind profiles from space. The three-dimensional global wind field observations along the instrument LOS are intended to compensate for the deficiencies of the current GOS and GCOS. Besides increased skill in NWP, the mission is also expected to contribute to some of the main issues of the World Climate Research Programme (WCRP), i.e., validation and improvement of climate models and thus quantification of climate variability. Progresses in climate research are closely linked to progress in the understanding and representation of atmospheric dynamics in operational weather forecasting.

The key benefits expected from Aeolus that are essential for this thesis can be highlighted as follows (ESA, 1999, 2008, 2016):

- the comprehensive observation of the large-scale flow will improve modeling and understanding of tropical dynamics, especially tropical circulation systems,
- improvements in the initial state in the tropics, the Southern Hemisphere, and over oceans, where direct wind measurements are rare, will lead to better analysis quality and increased forecasting skill,
- better detection of the small-scale wind field (especially vertical wind shear) will improve the short-range forecast of severe and intense storm developments,
- improvements in the characterization of planetary-scale waves will increase the medium-range forecasts for the extratropical region,
- better detection of atmospheric wave activities will lead to better analysis of scale interactions and teleconnection processes,
- the high vertical measurement coverage of the wind observations will improve the forecasts of stratospheric dynamics.

1.2 Research goals and outline of the thesis

A completely new data set of wind observations is available from the Aeolus mission, filling a significant gap in the global measuring network. This thesis aims to contribute to the optimal use of the Aeolus wind observations in NWP models and to evaluate the expected benefits for NWP using the global data assimilation system of the ICOsahedral Nonhydrostatic (ICON) model of Deutscher Wetterdienst (DWD).

The **research questions** that are addressed in this thesis can be summarized as follows:

1 What are the characteristics of the systematic and random errors of the Aeolus wind observations, and how can the Aeolus observational error be estimated?

2 How can the systematic errors be corrected to optimize the use of the Aeolus wind observations in data assimilation?

3 What is the relative benefit of the Aeolus observations in the framework of the global assimilation system at DWD? Does Aeolus fulfill the expected contribution to the GOS?

4 Which dynamical scenarios and processes are related to the particularly high impact of Aeolus on NWP forecasts?

To answer **research question 1** and **2**, the first part of this thesis is concerned with the validation of the HLOS wind profiles. The validation study is conducted for the mission's initial phase before the operational use of the data. It provides the basis for the assimilation of these novel observations in the global data assimilation system at DWD. For a comprehensive characterization of the systematic and random errors, the Aeolus HLOS wind profiles are compared to three independent reference data sets: collocated radiosonde wind profiles from the GOS and model equivalents from the ICON model of DWD and the ECMWF Integrated Forecast System (IFS) model around the collocation points. Because radiosonde observations are rare in the Southern Hemisphere and tropical band, the validation statistics initially focus on the Northern Hemisphere midlatitudes. These regional validation results are then placed in a global context, using only the model equivalents for an additional global statistic. To determine the Aeolus observational error within the validation study, the representativeness errors of the different comparisons have to be estimated. For this purpose, analysis data from the regional Consortium for Small-scale MOdeling (COSMO) model of DWD and high-resolution ICON Large Eddy Model (LEM) simulations are used to compute the individual components contributing to the uncertainties due to representativeness. The systematic differences are further examined for their dependencies, and then possible bias correction approaches that can be used for the assimilation are tested.

The second part of this thesis investigates the impact of the Aeolus HLOS wind observations in the ICON model to address **research question 3** and **4**. Therefore, an impact study based on an OSE of a three-month summer period is analyzed. The OSE consists of two continuous assimilation cycles, with and without the assimilation of Aeolus observations, using the operational setting of the global assimilation system of the ICON model with a corresponding cycled ensemble run. First, a global overview of the systematic

changes in the analysis and forecast between the two assimilation runs is provided. The impact of Aeolus HLOS winds on the short- and medium-range forecast is examined using a selection of conventional observations and ECMWF Reanalysis 5th Generation (ERA5) reanalysis as verification data. In addition to the statistical impact overview, specific periods and regions of particularly pronounced impact are investigated to better understand the underlying dynamic aspects leading to the improvements. Potential pathways for significant forecast error reduction through the assimilation of Aeolus wind observations are identified. The focus is on the change in phase of the large-scale tropical circulation systems QBO and ENSO, and the midlatitudes, where spatiotemporal surveys show large forecast error reduction following the extratropical transition (ET) of tropical cyclones and their interaction with the midlatitude waveguide.

Structure of the thesis:

The first section of **Chapter 2** summarizes the basic principles of the Aeolus observations, including the measurement concept of DWLs, and the specific characterization of the Aeolus instrument and HLOS wind data. Furthermore, the main changes in the Aeolus data set during the mission that are relevant for this thesis are outlined. The second section of **Chapter 2** provides a general introduction to data assimilation methods relevant to the DWD data assimilation system, including the Three-Dimensional Variational Assimilation and the Ensemble Kalman Filtering technique. Subsequently, a description of the DWD global data assimilation system and an overview of the main observation error components in data assimilation is given. **Chapter 3** introduces the data sets, the experimental set-up, and the statistical methods for the validation of the Aeolus wind observations and for the impact evaluation. **Chapter 4** is the first part of the main results of the thesis. Systematic and random error estimates are determined by comparing the Aeolus observations with collocated radiosonde observations and model equivalents from the DWD ICON and the ECMWF IFS model. Furthermore, the Aeolus observational error is evaluated, which includes the estimation of representativeness errors. Systematic error dependencies are then further investigated, and a simple correction approach is tested. **Chapter 5** is the second part of the main results of the thesis. It evaluates the impact of the Aeolus wind observations in the ICON model using a three-month OSE based on the operational settings of the DWD global assimilation system. Global statistical analyses of systematic changes in the analysis and forecast error are provided. Furthermore, specific high-impact time periods and regions are identified, and the dynamics behind the forecast error reduction are discussed. **Chapter 6** summarizes the main conclusions of the thesis and provides an outlook on possible continuing research.

Chapter 2

Basic principles

2.1 Aeolus observations

This section outlines the fundamentals of the Aeolus observations. The description of wind lidar observations, particularly DWLs, is mainly based on Weitkamp (2005) and Reitebuch (2012b). The specific design of the Aeolus instrument ALADIN is explained using information from Reitebuch (2012a), Reitebuch et al. (2020) and Lux et al. (2021). An overview of all Aeolus data products and the scientific data processing levels is provided by the ADM-Aeolus Science Report (ESA, 2008). The algorithms developed for the wind profile retrievals are explained in Rennie et al. (2020) and Tan et al. (2008).

2.1.1 DWL ALADIN measurement concept

Backscatter lidar observations

In lidar remote sensing, a short laser pulse is emitted at a specified wavelength, and the signal backscattered from the atmosphere is received in a time-resolved manner. The wide range of interaction processes of the actively emitted photons with the atmosphere's constituents enable detailed evaluations of atmospheric variables, such as temperature,

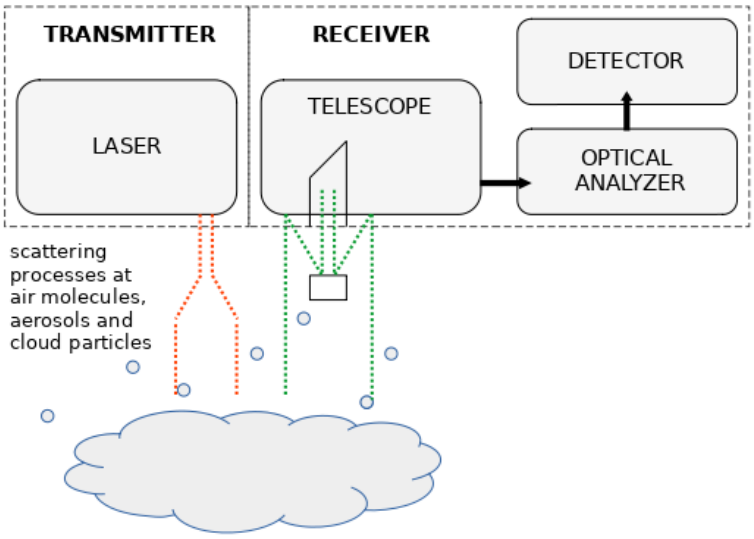

Figure 2.1: *Schematic illustration of the principle setup of a backscatter lidar system.*

pressure, humidity, and wind, as well as the determination of trace gases, aerosol, and cloud layers (Weitkamp, 2005). Lidar systems can be deployed from ground-based, airborne, ship-borne, balloon-borne, or space-based platforms. Essentially, a lidar consists of a laser transmitter and a receiving device. Fig. 2.1 shows the schematic of a basic lidar set up. The wavelength of the laser typically ranges from 250 nm to 11 μm. On the receiving end, first, a telescope collects the backscattered photons, and then the signal is analyzed with an optical receiver and recorded with a detector.

The emitted laser signal interacts with air molecules, aerosols, and cloud particles through scattering and absorption processes. The scattering takes place with different intensities in all directions so that a small part returns backward to the lidar and can be detected. Primarily, this is elastic scattering, meaning the wavelength remains unchanged during the scattering process. However, a distinction is made between the scattering from particles with sizes comparable to the wavelength of the radiation (Mie scattering) and the scattering from particles that are very small compared to the wavelength (Rayleigh scattering). The power of the total scattered signal $P(\lambda, r)$ [W] received by the detector of the lidar operating at a certain wavelength λ as function of distance r is described by the lidar equation. In simplified form, the lidar equation reads (Weitkamp, 2005):

$$P(\lambda, r) = \underbrace{K}_{(1)} \cdot \underbrace{G(r)}_{(2)} \cdot \underbrace{\beta(\lambda, r)}_{(3)} \cdot \underbrace{T^2(\lambda, r)}_{(4)}. \tag{2.1}$$

The factors (1) and (2) are fully determined by the lidar instrument; the factors (3) and (4) cover the information about the atmosphere. The constant K summarizes the signal transmission, containing the laser pulse energy, the temporal pulse length, the speed of light, the area of the telescope, and overall system efficiency. $G(r)$ describes the range-dependent terms of the measurement geometry, including a term $\propto \frac{1}{r^2}$ as the strength of the signal decreases with distance. $\beta(\lambda, r)$ is the backscatter coefficient at distance r. It determines the strength of the lidar signal by describing the probability of how much light is scattered back towards the receiver. It can be written as the sum of the molecular and the particulate scattering coefficient:

$$\beta(\lambda, r) = \beta_{mol}(\lambda, r) + \beta_{aer}(\lambda, r). \tag{2.2}$$

The term $T(\lambda, r)$ is the atmospheric transmission that takes values between 0 and 1 and describes how much light gets lost on the way from the lidar to the target at the emitted wavelength λ at a distance r. It contains the extinction coefficient, which is the sum of all transmission losses that can occur because of scattering or absorption by molecules and particles. In addition to the factors described above, the receiver detects a background signal from the sun, the moon or other light sources in the atmosphere. The error contribution due to the background signal must be determined before further evaluations.

Principles of Doppler Wind Lidars

To measure wind speed, most lidars rely on the Doppler effect phenomenon. Suppose particles move in the viewing direction of the laser, the wavelength of the scattered light is shifted, and the frequency change of the received signal relative to that emitted (Doppler shift) can be used to determine the line-of-sight wind.

For electromagnetic waves, the frequency is linked to the wavelength via the speed of light. If a laser with wavelength λ_0 and frequency $f_0 = \frac{c}{\lambda_0}$ emits light into the atmosphere and the relative velocity along the LOS is v, then the frequency observed by moving particles is:

$$f_1 = \frac{v + c}{\lambda_0} = f_0(1 + \frac{v}{c}). \tag{2.3}$$

The backscattered light that is detected by the lidar receiver is again shifted to:

$$f_2 = \frac{v + c}{\lambda_1} = f_1(1 + \frac{v}{c}) = f_0(1 + \frac{v}{c})^2 \approx f_0(1 + 2\frac{v}{c}). \tag{2.4}$$

The quadratic term $\frac{v^2}{c^2}$ is neglected since v is much smaller than the speed of light c. The total shift in frequency or wavelength is then:

$$\Delta f = f_2 - f_0 = 2f_0\frac{v}{c} \tag{2.5}$$

$$\Delta\lambda = \lambda_2 - \lambda_0 = -2\lambda_0\frac{v}{c} \tag{2.6}$$

If an observer moves towards the lidar, which corresponds to a positive LOS velocity, the wavelength is shifted to smaller wavelengths, also called "blue shift". Negative LOS velocity leads to a shift towards larger wavelengths ("red shift"). For a LOS speed of 1 m s^{-1} and $c \approx 2.998{\cdot}10^8$ m s^{-1} the relative Doppler shift $\frac{\Delta f}{f_0}$ is $6.68{\cdot}10^{-9}$. To detect such small changes in the frequency, high technical requirements in terms of measurement instrument accuracy must be met.

The mean movement of all particles within a certain atmospheric volume, which is defined as wind, is superimposed by individual thermal molecular motion (Brownian motion). In dilute gases, the wavelength of the laser is relatively small in comparison to the mean free path of gas molecules in the measurement volume so that thermal agitation is to be taken into account. This causes Doppler broadening in the backscatter return signal. The broadening can be approximately described by a Gaussian distribution with standard deviation:

$$\sigma_\nu = \sqrt{\frac{kT}{m}}, \tag{2.7}$$

where k is the Boltzmann constant, m is the particle's mass, and T is the atmospheric temperature. Because of their higher mass, the Gaussian velocity distribution is several orders of magnitude narrower for aerosols and cloud particles than for molecules. When density is larger, in addition to agitation, the collision between molecules becomes important. This can excite waves that scatter the laser light, known as Rayleigh-Brillouin scattering (Gu and Ubachs, 2014, Witschas et al., 2012). Therefore, temperature and pressure affect the Doppler shift's broadening properties and, thus, the backscattered signal's spectrum. Fig. 2.2 shows the schematic of the backscatter spectrum originating from a laser emitting pulses with $\lambda_0 = 355$ nm. For atmospheric temperatures of 15°C the Full-Width at Half Maximum (FWHM), which typically defines the spectral bandwidth, is about 1.6 pm for the broadband Rayleigh scattering from molecules and 21 fm, i.e., several orders of magnitude narrower, for aerosol and cloud particle Mie scattering. The mean wind speed of an air volume corresponds to the parallel shift of both the Mie and the Rayleigh spectrum and is described by the mean of the distribution directly reflected in the Doppler wavelength shift.

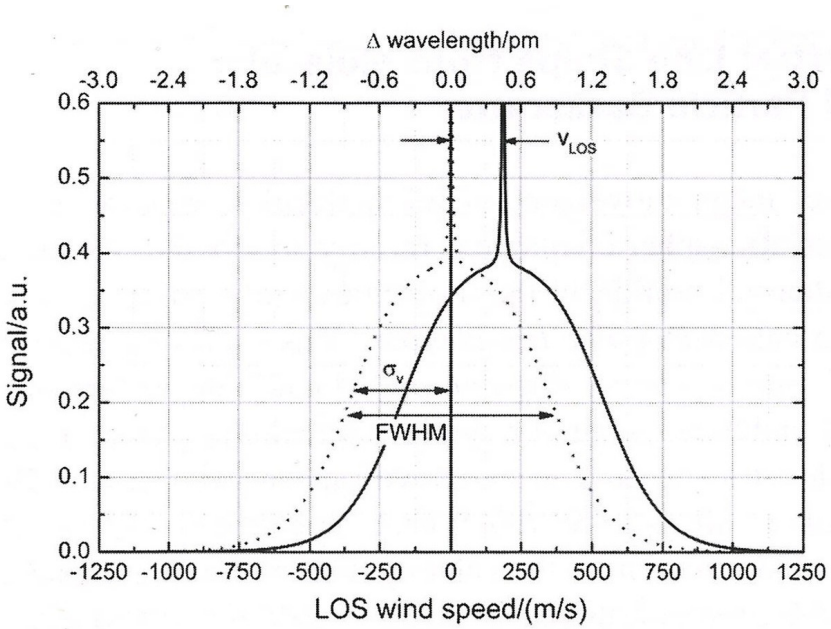

Figure 2.2: *Spectrum of Mie and Rayleigh backscattered signal from a DWL with a laser operating at 355 nm for LOS wind speed of 0 m s^{-1} (dotted line) and a LOS wind speed of 180 m s^{-1} (solid line). The abscissa displays the corresponding shift in wavelength on the top. σ_ν is the standard deviation, and FWHM indicates the Full-Width at Half Maximum of the Rayleigh spectrum. From Reitebuch (2012b).*

DWL systems are usually either based on coherent or direct detection to retrieve the LOS speed. Coherent detection lidars operate in the near-infrared (1.5-1.6, 2 and 10 μm) and are commercially available nowadays. The return signal is mixed with the radiation from a local oscillator, and the resulting beat signal is measured. The signal amplitude and frequency information is determined with high accuracy and precision, requiring no additional parameters or calibration. However, due to its small-bandwidth detection principle, coherent DWLs rely on aerosol and cloud particle backscatter and are, therefore, primarily used for wind measurements in the atmospheric boundary layer. Compared to coherent detection lidars, direct detection DWLs are also suitable for measurements in upper atmospheric levels. They are based on an optical spectral analyzer, typically a bandpass filter or interferometer, to gain information about the Doppler shift, allowing for both the Rayleigh and Mie spectrum analysis. A possibility to realize the filter technique is the double-edge filter method that uses two bandpass filters symmetrically placed around the Rayleigh spectrum with maximum transmission around the inflection points. The ratio of transmitted signal through each filter is used to determine the Doppler shift. Calibration is needed because of the sensitivity to atmospheric temperature and pressure of the Rayleigh backscatter signal (Rayleigh-Brillouin scattering) and its dependence on the actual filter transmissions. The two filters can be realized with a Fabry-Perot interferometer and are used with laser wavelengths in the ultraviolet (UV) (355 nm), visible (532 nm), and near-infrared (1064 nm). Besides the double-edge method, the single-edge filter technique can be applied for direct-detection lidars to specify narrow bandwidth absorption lines. However, this method is limited since only absorption lines that occur in the transmission wavelength of the laser can be measured. In addition to the filter techniques, fringe imaging is a common implementation on direct-detection wind lidars to determine the Doppler

shift. E.g., Fabry-Perot or Fizeau interferometers are used to measure the displacement of interference patterns which are imaged onto a detector with pixel-wise spectral channels such as a charge-coupled device (CCD).
The first airborne direct-detection DWL was developed between 2003 and 2005 at DLR and the European Aeronautic Defence and Space Company (EADS-Astrium) as an airborne prototype for the Aeolus instrument ALADIN. The so-called ALADIN Airborne Demonstrator (A2D) is, like ALADIN, composed of complementary receiver channels using the double-edge and fringe-imaging technique. It delivered valuable information for instrument validation and optimization of the wind retrieval and related quality-control algorithms (Lux et al., 2020, Reitebuch et al., 2009).

Aeolus DWL ALADIN specific design

The spaceborne direct-detection DWL ALADIN onboard the Aeolus satellite operates at a wavelength of 354.9 nm. Laser light in the UV spectral region allows for wind observations at higher altitudes, dominated by Rayleigh scattering, which is inversely proportional to the fourth power of wavelength. A detailed schematic of the instrument from Lux et al. (2021) is displayed in Fig. 2.3. ALADIN consists of two fully redundant switchable laser transmitters (FM-A and FM-B). The laser light is emitted at a frequency of 50.5 Hz via the same primary and secondary mirror of the 1.5 m diameter Cassegrain-type telescope that collects the backscatter signal. A beam splitter (BS) separates a small fraction of the laser beam that is directed to the receiver to determine the frequency of the outgoing signal and further calibrate the receiver spectrometer. This is called the internal reference path signal (INT). The other fraction of the laser signal interacts with the atmospheric constituents. The backscatter return enters the transmit-receive optics (TRO) and is then superimposed on the INT. A dual channel receiver analyzes the Doppler shift to measure the frequency from the narrowband Mie and the broadband Rayleigh backscatter separately. Both channels use a direct-detection method. The spectrometer of the Rayleigh channel is based on the double-edge technique realized by two Fabry-Perot interferometers. The Mie spectrometer relies on the fringe-imaging technique using a Fizeau interferometer. Two identical Accumulation Charge-Coupled Devices (ACCDs) with a 16 x 16-pixel imaging zone detect the Rayleigh and Mie signals. The binned charges of the 16 rows are stored, representing one vertical range gate for the backscatter signal. The memory zone allows for a number of 24 range bins in total. The range bins can be varied along orbit from a minimum vertical resolution of 250 m to 2000 m and thus adjusted to the needs of science applications and NWP. Typically, the uppermost measurement altitude is about 17-25 km. Horizontally, a minimum along-track resolution of 2.9 km (temporal resolution of 0.4 s) is achieved by accumulating 20 laser pulses and referred to as one “measurement”. Further processing of the different Aeolus products is applied on-ground.

2.1.2 Level-2B wind processing

The Aeolus level-2B (L2B) wind product contains the HLOS wind observations suitable for use in NWP. The operational L2B processing is performed in near-real-time at ECMWF. To control the horizontal resolution and achieve a sufficient signal-to-noise ratio, the measurements are grouped according to a scene-classification procedure into a type “clear” or “cloudy” (Rennie et al., 2020, Tan et al., 2008). Therefore, measurement-scale optical

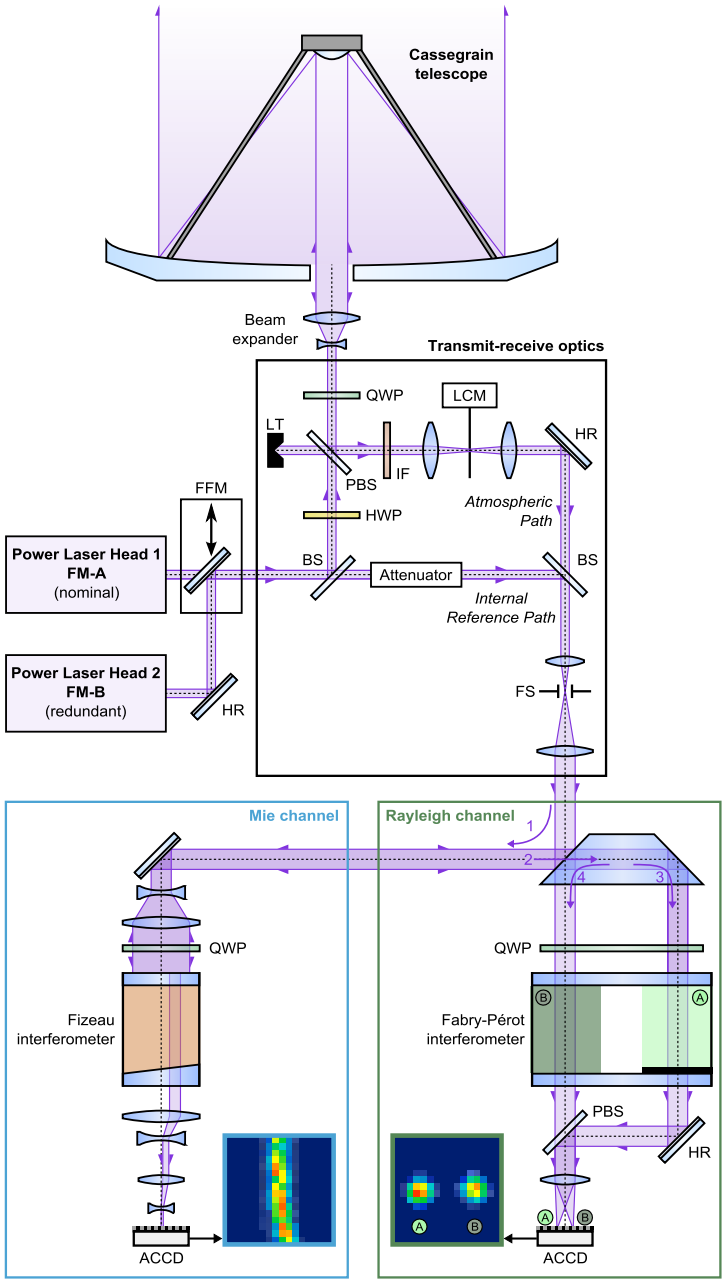

Figure 2.3: *Schematic of the direct-detection Doppler wind lidar ALADIN. From (Lux et al., 2021).*

properties, e.g., scattering ratio or particle extinction coefficient, are used to determine how much particulate and molecular backscatter contributes to the signal of an accumulated measurement bin. Due to the dual-channel receiver, four wind observation types are available: Rayleigh-clear and -cloudy with a horizontal average length of about 90 km, and Mie-clear and -cloudy, which represent a horizontal mean of 10 km (since 5 March 2019). A key step within the L2B processing chain is the correction for temperature and pressure-dependent Doppler broadening in the molecular backscatter signal (Rayleigh–Brillouin correction). This uses a series of auxiliary files containing information about, e.g., geolocation, calibration, and error estimates for several variables, as well as a prior (AUX_MET) data of atmospheric temperature and pressure from a short-range forecast (Šavli et al., 2021). In addition, the L2B processor provides several output data, such as uncertainty estimates or quality flags for the wind observations that are useful for data assimilation systems.

2.1.3 Overview: Satellite orbit and measurement geometry

The Aeolus satellite flies approximately 320 km above the terminator in a sun-synchronous, nearly polar orbit. It, therefore, always crosses a given point on the Earth's surface at the same local mean solar time. The local equatorial crossing time is 06 and 18 UTC, representing sunrise and sunset. The DWL onboard the Aeolus satellite is pointing 35° off-nadir towards the night side of the Earth. Measurements along the terminator pointing in anti-sun direction benefit from the minimized impact of solar background radiation. Aeolus flies at 7.7 km s^{-1} providing a quasi-global coverage within seven days (111 orbits) (Fig. 2.4).

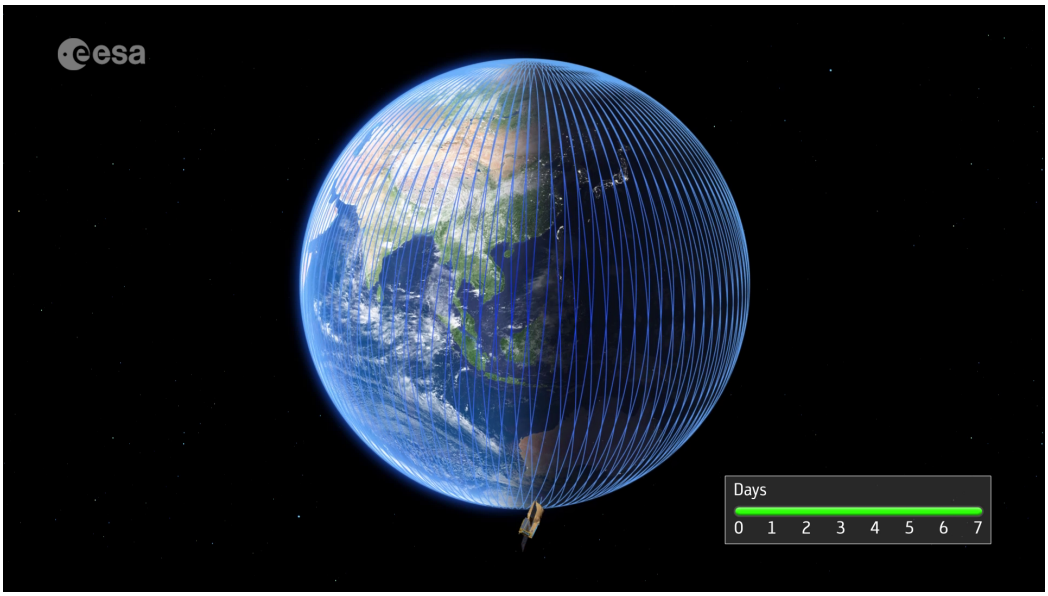

Figure 2.4: *Aeolus satellite orbits after seven days. From* `https://www.esa.int/Applications/Observing_the_Earth/FutureEO/Aeolus/Aeolus_satellite`

The orbits are spatially separated by about 18-19°, which corresponds to ∼2000 km in the tropics and ∼1000 km in the midlatitudes. The LOS of the instrument is 90° relative to the satellite's flight direction to ensure that the satellite velocity does not contribute to the measured Doppler frequency shift.

Fig. 2.5 displays a sketch of the measurement geometry of Aeolus. The LOS wind consists of a horizontal and vertical wind component (Fig. 2.5a):

$$v_{LOS} = v_{HLOS} \ cos\alpha - v_w \ sin\alpha, \tag{2.8}$$

with α being the elevation of the satellite-to-target pointing vector, v_{HLOS} being the horizontal projection of the LOS wind (HLOS), and v_w being the vertical wind (Krisch et al., 2022). Because of the curvature of the Earth, α is $\sim$ 52-54°, which is a bit smaller than expected from the sketch (Fig. 2.5).

(a) *vertical*

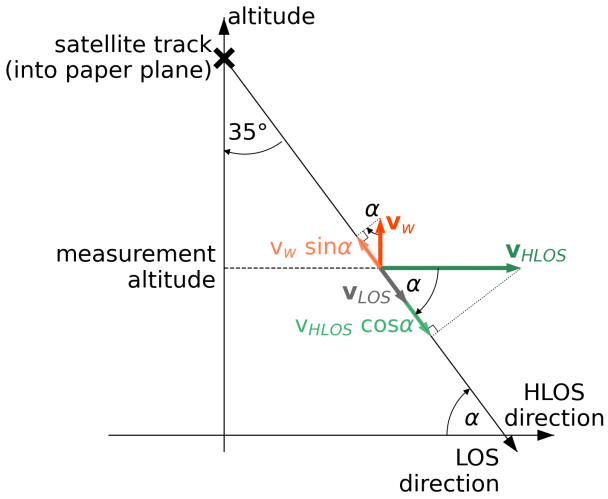

(b) *ascending*

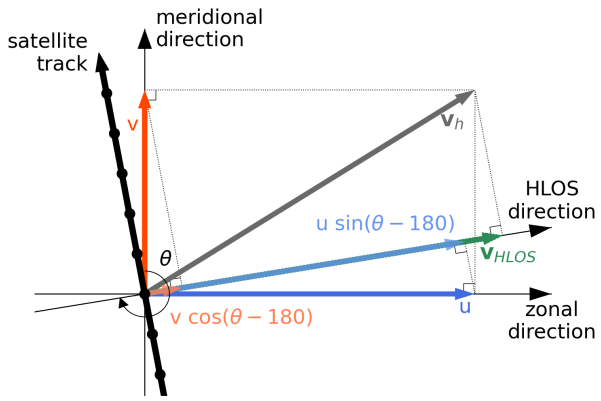

(c) *descending*

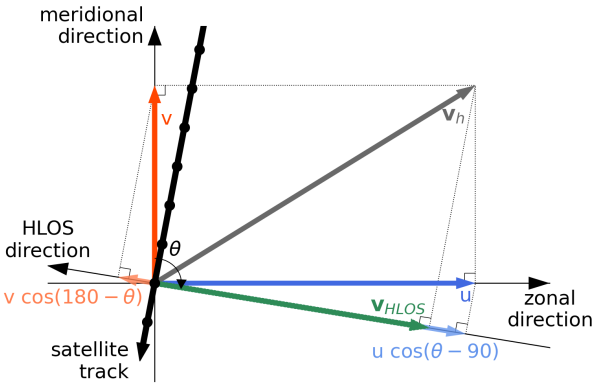

Figure 2.5: *Measurement geometry of Aeolus (according to Krisch et al. (2022)): (a) vertical along LOS plane for satellite track direction into the paper plane and horizontal plane for (b) ascending and (c) descending orbits, respectively, for track angles of 10° from the north.*

For better illustration the vertical wind in Fig. 2.5a is extraordinary strong. However, typically v_w is much smaller than v_{HLOS} and thus assumed to be negligible in the formulation for the HLOS wind within the L2B processing chain. This assumption might cause errors

in certain conditions, such as strong convection or gravity waves, and at small horizontal scales where horizontal and vertical velocity can be of the same order of magnitude.
The HLOS wind can be written as a linear function of the zonal u and meridional v wind component using the azimuth angle θ, which is defined as the angle of the LOS pointing vector of the laser projected onto the horizontal plane measured clockwise from north.

$$v_{HLOS} = -u \ sin(\theta) - v \ cos(\theta). \tag{2.9}$$

θ is provided as part of the observation geolocation information by the L2B product, being typical ∼260° for ascending and ∼100° for descending orbits. As the DWL LOS direction is perpendicular to the satellite–Earth relative velocity, the HLOS winds outside the polar regions mainly correspond to the zonal wind direction. The westerly winds in the midlatitudes and tropics are measured as positive HLOS for ascending and as negative HLOS winds for descending orbits. At higher latitudes, the meridional wind dominates the HLOS winds.

2.1.4 Main changes in the Aeolus L2B data set during the mission

Because Aeolus is a novel Earth Explorer mission, the processing algorithms have been evolving a lot since launch. The multiple updates of the Payload Data Ground Segment (PDGS) baseline cause different data quality for different time periods. Furthermore, the instrument performance, particularly the laser FM-A performance, is not constant, affecting the atmospheric path signal, the receive path efficiency, and the detector. A complete, consistently processed data set with uniform processor settings was not yet available for the evaluations of this thesis. The main changes in the L2B data from the satellite launch to the end of September 2020 are highlighted in the timeline in Fig. 2.6.

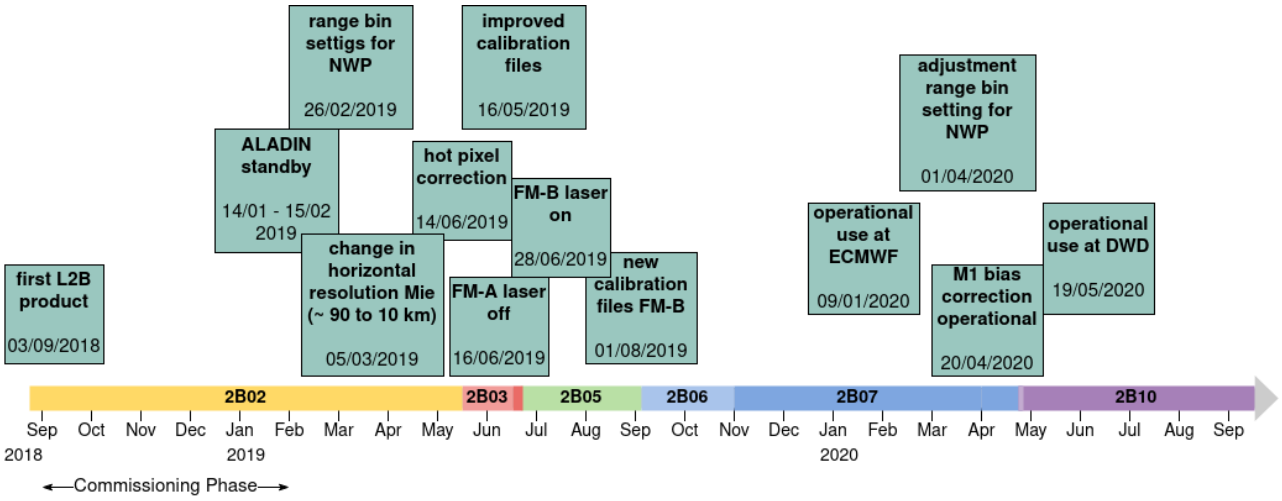

Figure 2.6: *Timeline from the Aeolus launch in August 2018 to September 2020 to mark the main changes in the L2B data set, including periods of different processor baselines 2B02-2B10 (color-coded).*

During the Commissioning Phase (CP, from launch until the end of January 2019), the range bin settings for Rayleigh and Mie were kept fix with a thickness of 250 m near the surface, 1 km in the mid-troposphere and 2 km in the lower stratosphere up to a

maximum measurement height of around 20 km. After the CP, the range bin setting was changed to be more appropriate for NWP. In particular, the vertical sampling around the jet stream has been increased. Further optimizations in the range bin setting in the tropics and extratropics were applied in April 2020.

In March 2019, the maximum horizontal averaging length scale of the Mie winds has been changed. During the CP, the horizontal resolution was the same for both Rayleigh and Mie (∼90 km). Therefore, the number of observations was about four times more for Rayleigh-clear than Mie-cloudy wind observations in the upper troposphere (Šavli et al., 2019). In order to increase the signal-to-noise ratio of cloud returns, the horizontal resolution of the Mie winds has been increased to ∼10-20 km.

Already at the beginning of the mission, it turned out that several range bins are affected by increased dark current rates (hot pixels) for specific ACCD detector pixels causing large biases in the HLOS winds. A correction using so-called Down Under Dark Experiment (DUDE) calibration data was implemented into the Aeolus operational processor chain (Weiler et al., 2020) on 14 June 2019.

An important intervention was the switch from laser FM-A to FM-B end of June 2019. The FM-A laser UV output energy decreased significantly at a rate of about 0.5-1 mJ per week between December 2018 and May 2019. This led to the decision to use the second laser, FM-B, which showed a better overall performance. Reasonable FM-B calibration files have been used operationally since 2 August 2019.

The updated baseline 2B10 introduced a major improvement in the HLOS winds systematic errors. On 20 April 2020, a near-real-time (NRT) bias correction was applied in the L2B processor. The bias correction uses linear correlations between O-B (observation-background) statistics from ECMWF and temperatures from the telescope primary mirror M1 to reduce biases that showed significant differences between ascending and descending orbit phases (Weiler et al., 2021).

The Aeolus observations have been operationally assimilated at ECMWF since January 2020 and at DWD since May 2020. Later in 2020, Météo-France and the UK Meteorological Office (Met Office) also began the operational assimilation of the Aeolus HLOS winds.

2.2 Data assimilation

The general task of data assimilation is to determine an optimal estimate for the true state of the atmosphere $\boldsymbol{x}^t$. Data assimilation algorithms usually start from an a-priori estimate obtained from earlier measurements and forecasts, the so-called background or first guess forecast state $\boldsymbol{x}^b$. This background state is adjusted using observational data $\boldsymbol{y}^o$ to get a new, improved estimate, the analysis $\boldsymbol{x}^a$. To find the best compromise, the various errors of each information source and their error covariances have to be taken into account (e.g., observation instrument errors, representativeness errors, background forecast errors). Each NWP model is linked to its specific data assimilation system, which must be adapted to the specific spatial and temporal scales of atmospheric processes and the observations available at each scale. This section first gives an overview of the theoretical background of data assimilation methods relevant to the DWD data assimilation system. Attention is drawn to the different elements that go into the core assimilation algorithms and to the particular algorithms themselves, namely the Three-Dimensional Variational Assimilation

(3D-Var) and Ensemble Kalman Filtering (EnKF/LETKF). Subsequently, the global data assimilation system of the DWD is specifically discussed. The description is mainly based on Hólm (2008), Kalnay (2003), Rhodin et al. (2022) and van Leeuwen (2016). Table 2.1 provides an overview of the important variables and operators that are used in this section.

Variable	Description
$\boldsymbol{x}^t$	true atmospheric state
$\boldsymbol{x}^a$	analysis state
$\overline{\boldsymbol{x}^a}$	analysis ensemble mean
$\mathbf{X}^a$	analysis ensemble perturbation matrix
$\boldsymbol{x}^b$	background state
$\overline{\boldsymbol{x}^b}$	background ensemble mean
$\mathbf{X}^b$	background ensemble perturbations
$\boldsymbol{y}^o$	observation vector
$\overline{\boldsymbol{y}^b}$	mean background observation ensemble (ensemble space)
$\mathbf{Y}^b$	background observation ensemble perturbations (ensemble space)
$\mathbf{B}$	background error covariance matrix
H	nonlinear observation operator
$\mathbf{H}$	linear observation operator matrix
$\mathbf{R}$	observation error covariance matrix
$\mathbf{K}$	Kalman gain matrix
J	cost function
M	nonlinear model operator
$\mathbf{Q}$	forecast model error covariance
$\mathbf{L}$	tangent linear model matrix
$\mathbf{I}$	identity matrix
$\mathbf{A}$	analysis error covariance matrix
$\mathbf{P}^a$	sample estimate of analysis error covariance matrix
$\widetilde{\mathbf{P}^a}$	sample estimate of analysis error covariance matrix (ensemble space)
$\mathbf{P}^b$	sample estimate of background error covariance matrix
$\mathbf{W}$	weight matrix
$\mathbf{w}$	weight vector

Table 2.1: *Overview of variable and operator definitions for Sec. 2.2*

Forecast model state:
Given $\boldsymbol{X} = \mathbb{R}^n$ being the model space and $\boldsymbol{x} \in \boldsymbol{X}$ being the model's state vector, $\boldsymbol{x}^t \in \boldsymbol{X}$ denotes the true state of the atmosphere and $\boldsymbol{x}^a \in \boldsymbol{X}$ is the estimate of the true state (analysis). The background state for the estimation of a new analysis (t_i) defined as a previous forecast (t_{i-1}) is:

$$\boldsymbol{x}^b(t_i) = M_{i-1}[\boldsymbol{x}^a(t_{i-1})], \tag{2.10}$$

where $M : X \to X$ is the nonlinear model operator.

Observations:
Given $\boldsymbol{Y} = \mathbb{R}^m$ being the observation space, the observations $\boldsymbol{y}^o \in \boldsymbol{Y}$ are:

$$\boldsymbol{y}^o = H(\boldsymbol{x}^t) + \boldsymbol{\epsilon}_o, \tag{2.11}$$

where $H : X \to Y$ is the observation operator that calculates the model equivalents for the observed quantities and $\boldsymbol{\epsilon}_o$ describes the observation error. For in-situ point-observations, the observation operator is comparatively easy performing bi-linear horizontal and vertical interpolation. More complex observation operators are required for e.g. satellite radiance, which use a radiative transfer model that calculates the outgoing radiation at the top of the atmosphere in the observed spectral interval from the atmospheric temperature and humidity profile as well as surface temperature.

Errors in data assimilation:
The errors in data assimilation (background $\boldsymbol{\epsilon}_b$, observation $\boldsymbol{\epsilon}_o$ and analysis $\boldsymbol{\epsilon}_a$ error) are defined as follows:

$$\boldsymbol{\epsilon}_b = \boldsymbol{x}^b - \boldsymbol{x}^t, \quad \boldsymbol{\epsilon}_o = \boldsymbol{y}^o - H(\boldsymbol{x}^t), \quad \boldsymbol{\epsilon}_a = \boldsymbol{x}^a - \boldsymbol{x}^t. \tag{2.12}$$

Because the true atmospheric state and, thus, the errors are unknown, only assumptions about their statistical properties can be made. Usually, they are assumed to be Gaussian distributed and free of bias:

$$E(\boldsymbol{\epsilon}_b) = E(\boldsymbol{\epsilon}_o) = E(\boldsymbol{\epsilon}_a) = 0, \tag{2.13}$$

Furthermore, the observation and model errors are considered to be uncorrelated:

$$E(\boldsymbol{\epsilon}_o \boldsymbol{\epsilon}_b^T) = 0. \tag{2.14}$$

The respective covariance matrices are:

$$\mathbf{B} = E(\boldsymbol{\epsilon}_b \boldsymbol{\epsilon}_b^T) \quad [n \times n], \quad \mathbf{R} = E(\boldsymbol{\epsilon}_o \boldsymbol{\epsilon}_o^T) \quad [m \times m], \quad \mathbf{A} = E(\boldsymbol{\epsilon}_a \boldsymbol{\epsilon}_a^T) \quad [n \times n], \tag{2.15}$$

with the variances $\mathrm{E}(\boldsymbol{\epsilon}_i^2) = \sigma_i^2$ on the diagonal.

The covariances in the observation error covariance matrix $\mathbf{R}$ are usually neglected in operational data assimilation, which is a valid assumption as observation errors are typically considered to be uncorrelated. However, if measurements are not independent (e.g. if they are derived using the same remote sensing instrument), then $\mathbf{R}$ should not be diagonal. The observation error consists of the instrument error $\mathbf{R}_{instr.}$, the operator error $\mathbf{R}_{operator}$ and the representativeness error $\mathbf{R}_{repr.}$ (more details are provided in Sec. 2.2.4).

The covariances in the background error covariance matrix $\mathbf{B}$ are generally spatially correlated between variables. The role of $\mathbf{B}$ is to ensure a physically consistent analysis update. It depends on the atmospheric conditions, however, methods such as 3D-Var assume this matrix to be constant over time, which is a rough assumption. The background error covariance matrix can rarely be represented explicitly and is one of the greatest challenges in data assimilation systems.

2.2.1 Three-dimensional variational assimilation

Variational methods seek the best analysis estimate by iterative minimization techniques finding the minimum of a given cost function that measures the model-to-observation misfit. This can be performed either for basic time steps separately (3D-Var) or for the trajectories of the system state in time (4D-Var) when the assimilation of observations within a time window is combined into a large minimization problem. Here, we focus on the 3D-Var algorithm.

To find the optimal analysis $\boldsymbol{x}^a$, a set of observations $\boldsymbol{y}^o$ has to be compared to the background field $\boldsymbol{x}^b$:

$$\boldsymbol{d} = \boldsymbol{y}^o - H(\boldsymbol{x}^b). \tag{2.16}$$

$\boldsymbol{d}$ is the innovation or observational departure.
Lorenc (1986) introduced the three dimensional cost function J of the state $\boldsymbol{x}$, that has to be minimized to find the optimal analysis $\boldsymbol{x}^a$ as the distance between $\boldsymbol{x}$ and $\boldsymbol{x}^b$ weighted by the inverse of $\mathbf{B}$ plus the distance between $\boldsymbol{x}$ and $\boldsymbol{y}^o$ weighted by the inverse of $\mathbf{R}$:

$$J(\boldsymbol{x}) = \underbrace{\frac{1}{2}(\boldsymbol{x}-\boldsymbol{x}^b)^T\mathbf{B}^{-1}(\boldsymbol{x}-\boldsymbol{x}^b)}_{J_b} + \underbrace{\frac{1}{2}[\boldsymbol{y}^o - H(\boldsymbol{x})]^T\mathbf{R}^{-1}[\boldsymbol{y}^o - H(\boldsymbol{x})]}_{J_o}. \tag{2.17}$$

The minimum is attained for $\boldsymbol{x} = \boldsymbol{x}^a$:

$$\nabla_{\boldsymbol{x}} J(\boldsymbol{x}^a) = 0. \tag{2.18}$$

In general, the observation operator H will be a nonlinear operator. However, using Taylor series expansion, H can be linearized around the background state $\boldsymbol{x}^b$:

$$\boldsymbol{y}^o - H(\boldsymbol{x}) = \boldsymbol{y}^o - H[\boldsymbol{x}^b + (\boldsymbol{x}-\boldsymbol{x}^b)] = [\boldsymbol{y}^o - H(\boldsymbol{x}^b)] - \mathbf{H}(\boldsymbol{x}-\boldsymbol{x}^b), \tag{2.19}$$

with $\mathbf{H}$ being the Jacobian matrix containing the first-order partial derivatives $h_{ij} = \frac{\partial H_i}{\partial x_j}$. Substituting Eq. (2.19) into the cost function $J(\boldsymbol{x})$ yields a quadratic function of the analysis increment $(\boldsymbol{x}-\boldsymbol{x}^b)$ that can be minimized directly. The gradient $\frac{\partial J}{\partial \boldsymbol{x}}$ with respect to the control variables $\boldsymbol{x}$ reads:

$$\frac{\partial J}{\partial \boldsymbol{x}} = \mathbf{H}^T\mathbf{R}^{-1}[H(\boldsymbol{x}) - \boldsymbol{y}^o] + \mathbf{B}^{-1}(\boldsymbol{x}-\boldsymbol{x}^b), \tag{2.20}$$

Setting Eq. (2.20) to zero leads to a set of linear equations which can be solved for the 3D-Var analysis state $\boldsymbol{x}^a$:

$$\boldsymbol{x}^a = \boldsymbol{x}^b + (\mathbf{B}^{-1} + \mathbf{H}^T\mathbf{R}^{-1}\mathbf{H})^{-1}\mathbf{H}^T\mathbf{R}^{-1}(\boldsymbol{y}^o - H\boldsymbol{x}^b), \tag{2.21}$$

$$\boldsymbol{x}^a = \boldsymbol{x}^b + \mathbf{K}(\boldsymbol{y}^o - H\boldsymbol{x}^b), \tag{2.22}$$

$$\text{where} \quad \mathbf{K} = (\mathbf{B}^{-1} + \mathbf{H}^T\mathbf{R}^{-1}\mathbf{H})^{-1}\mathbf{H}^T\mathbf{R}^{-1}. \tag{2.23}$$

$\mathbf{K}$ is the optimal weight matrix or the so-called Kalman gain. Formally, this is the solution of the 3D var problem. However, the multiplication of such large matrices is of high computational cost. Therefore, in practice, an iterative minimization algorithm determines the minimum of the cost function. At DWD, an iterative Newton method is used that searches for the minimum of the cost function by accounting for the nonlinearities that

cause the actual cost function to be only approximately quadratic. The Newton method implies a linearization of the observation operator and a quadratic approximation of the observation cost function. For the linear solution step, a preconditioned conjugate gradient method is employed.

To complete the 3D-Var algorithm, the background error covariance matrix **B** must be determined in addition to the observation error covariance **R**. The specification of the background error covariance matrix **B** determines how information from observations is spread to nearby grid points and levels. Error cross-correlations between variables always need to be included in **B** to ensure that observations of one model variable produce dynamically consistent increments in the other model variables. On large scales in the extratropical regions, e.g., the geostrophic wind balance translates into a strong correlation between wind- and mass-field errors. In 3D-Var, **B** typically is estimated climatologically with additional physical principles. At DWD, the so-called NMC method (named for the National Meteorological Center, now called the National Centers for Environmental Prediction (NCEP)) is used. This method estimates the forecast or background error covariance as averaged differences between forecasts of different lengths but verified at the same time (Parrish and Derber, 1992). However, all background errors are assumed to be statistically stationary and not flow-dependent, which in fact, is not true in NWP. 4D-Var algorithms that assimilate the observations at the correct time additionally allow for the evolution of **B**. Therefore, they use implicitly flow-dependent structure functions within the assimilation window (Thépaut et al., 1993). Nonetheless, the algorithm itself does not provide an estimate of the background error covariance for the next assimilation cycle. Fully flow-dependent estimates of the uncertainty of the forecast can be derived using ensemble data assimilation methods. The principles of the EnKF algorithm that is used as one of the core modules in the global data assimilation system at DWD are described in the following.

2.2.2 Ensemble Kalman Filter

The EnKF uses an ensemble of assimilation cycles to sample-estimate and predict the forecast uncertainty to then find an estimate of the true atmospheric state (ensemble mean) and its errors (ensemble spread). In general, three steps are required: In the **analysis step**, the analysis is computed from the current observations and a background ensemble. Then, the analysis ensemble is produced by resampling (**resampling step**) followed by the **forecast step** in which the analysis ensemble members are propagated forward to obtain a new forecast/background ensemble.

Assuming an ensemble consisting of N_e members, the forecast ensemble $\boldsymbol{x}_e^b(t_i)$ at time t_i is:

$$\boldsymbol{x}_e^b(t_i) = M_{i-1}[\boldsymbol{x}_e^a(t_{i-1})], \quad e = 1, ..., N_e. \tag{2.24}$$

The ensemble mean simply gives the most likely background state:

$$\overline{\mathbf{x}^b} = \frac{1}{N_e} \sum_{e=1}^{N_e} \boldsymbol{x}_e^b. \tag{2.25}$$

With the background ensemble perturbation matrix $\mathbf{X}^b = [\boldsymbol{x}_1^f - \overline{\mathbf{X}^b}, ..., \boldsymbol{x}_{N_e}^f - \overline{\mathbf{X}^b}]$ of dimension $n \times N_e$, the background ensemble error covariance matrix can be written as:

$$\mathbf{P}^b = \frac{1}{N_e - 1}\mathbf{X}^b(\mathbf{X}^b)^T. \tag{2.26}$$

The analysis must determine a state estimate $\overline{\mathbf{x}^a}$ with covariance matrix:

$$\mathbf{P}^a = \frac{1}{N_e - 1}\mathbf{X}^a(\mathbf{X}^a)^T, \tag{2.27}$$

where $\mathbf{X}^a = [\boldsymbol{x}_1^a - \overline{\mathbf{x}^a}, ..., \boldsymbol{x}_{N_e}^a - \overline{\mathbf{x}^a}]$ is the analysis ensemble perturbation matrix. The analysis mean should meet the following equation:

$$\overline{\mathbf{x}^a} = \overline{\mathbf{X}^b} + \mathbf{K}[\boldsymbol{y}^o - H(\overline{\mathbf{X}^b})], \tag{2.28}$$

with $\mathbf{K}$ being the ensemble Kalman Gain that uses the background ensemble error covariance matrix as an approximation for the full background error covariances:

$$\mathbf{K} = \mathbf{P}^b\mathbf{H}^T[\mathbf{R} + \mathbf{H}(\mathbf{P}^b)^T\mathbf{H}^T]^{-1}. \tag{2.29}$$

Except for $\mathbf{P}^b$ instead of $\mathbf{B}$ Eq. (2.23) and Eq. (2.29) are identical.
The first type of EnKF for atmospheric applications proposed by Evensen (1994) and further elaborated by Burgers et al. (1998) and Houtekamer and Mitchell (1998) uses perturbed observation ensembles to obtain $\mathbf{x}_i^a$. Perturbed observations can be created by adding noise with zero mean onto actual or model-predicted observations for each member. Due to the additional Gaussian observation spread normalizing the ensemble update, a stochastic filter can deal with nonlinearity to some extent. However, it introduces additional sampling noise and is only affordable for small ensembles. The second type of EnKF algorithms are deterministic filters, also called Ensemble Square Root Kalman Filters (EnSRF), that use an ensemble approximating the analysis error covariance matrix $\mathbf{P}^a$ to generate an analysis ensemble. Deterministic EnKFs mainly vary in how the transform matrix $\mathbf{T}$ is calculated in the analysis step:

$$\mathbf{X}^a = \mathbf{X}^b\mathbf{T}. \tag{2.30}$$

Using Eq. (2.26), Eq. (2.27) and Eq. (2.29), the analysis error covariance matrix can be written as:

$$\mathbf{P}^a = [\mathbf{I} - \mathbf{K}\mathbf{H}]\mathbf{P}^b, \tag{2.31}$$

$$\mathbf{X}^a(\mathbf{X}^a)^T = \mathbf{X}^b\{\mathbf{I} - (\mathbf{X}^b)^T\mathbf{H}^T[(N_e - 1)\mathbf{R} + \mathbf{H}\mathbf{X}^b(\mathbf{X}^b)^T\mathbf{H}^T]^{-1}\mathbf{H}\mathbf{X}^b\}(\mathbf{X}^b)^T, \tag{2.32}$$

or by defining model observation perturbations as:

$$\mathbf{S} = \mathbf{H}\mathbf{X}^b, \tag{2.33}$$

in a simpler form:

$$\mathbf{X}^a(\mathbf{X}^a)^T = \mathbf{X}^b\{\mathbf{I} - (\mathbf{S}^T[(N_e - 1)\mathbf{R} + \mathbf{S}\mathbf{S}^T]^{-1}\mathbf{S}\}(\mathbf{X}^b)^T. \tag{2.34}$$

Let $\mathbf{F}$ be the innovation matrix:

$$\mathbf{F} = [(N_e - 1)\mathbf{R} + \mathbf{S}\mathbf{S}^T]^{-1}, \tag{2.35}$$

the square root of

$$\mathbf{T}\mathbf{T}^T = \mathbf{I} - \mathbf{S}^T\mathbf{F}\mathbf{S}, \tag{2.36}$$

determines the analysis ensemble perturbation matrix.

A common square root filter is the Ensemble Transform Kalman Filter (ETKF) (Bishop et al., 2001). The ETKF solves the problem computationally efficiently by transforming it from high-dimensional model space into the low-dimensional ensemble space.
In general, the analysis update for the ETKF is written as

→ ensemble analysis mean

$$\overline{\mathbf{x}^a} = \overline{\mathbf{X}^b} + \mathbf{X}^b\overline{\mathbf{w}}, \tag{2.37}$$

→ ensemble analysis perturbations

$$\mathbf{X}^a = \mathbf{X}^b\mathbf{W} \tag{2.38}$$

, where $\overline{\mathbf{w}}$ is the weight vector that minimizes the ETKF-cost function in the N_e-dimensional ensemble space. Assuming a linear observation operator $\mathbf{H}$, the ETKF 3D cost function reads:

$$J(\mathbf{w}) = \underbrace{(N_e - 1)(\mathbf{w}^T\mathbf{w})}_{J_b} + \underbrace{(\boldsymbol{y}^o - \overline{\boldsymbol{y}^b} - \boldsymbol{Y}^b\mathbf{w})^T\mathbf{R}^{-1}(\boldsymbol{y}^o - \overline{\boldsymbol{y}^b} - \boldsymbol{Y}^b\mathbf{w})}_{J_o}, \tag{2.39}$$

with the background observation ensemble mean $\overline{\boldsymbol{y}^b} = \mathbf{H}\overline{\boldsymbol{x}^b}$ and perturbations $\boldsymbol{Y}^b = \mathbf{H}\boldsymbol{X}^b$. Due to the transformation, the minimization can be computed explicitly:

$$\overline{\mathbf{w}} = \widetilde{\mathbf{P}^a}(\boldsymbol{Y}^b)^T\mathbf{R}^{-1}(\boldsymbol{y}^o - \overline{\boldsymbol{y}^b}), \tag{2.40}$$

with

$$\widetilde{\mathbf{P}^a} = [(N_e - 1)\mathbf{I} + (\boldsymbol{Y}^b)^T\mathbf{R}^{-1}\boldsymbol{Y}^b]^{-1}. \tag{2.41}$$

Re-transformation gives the analysis error covariance matrix in model space:

$$\mathbf{P}^a = \mathbf{X}^b\widetilde{\mathbf{P}^a}(\mathbf{X}^b)^T. \tag{2.42}$$

The analysis ensemble perturbation weight matrix $\mathbf{W}$ is then computed via:

$$\mathbf{W} = [(N_e - 1)\widetilde{\mathbf{P}^a}]^{\frac{1}{2}}. \tag{2.43}$$

A specification of the ETKF is the Local Ensemble Transform Kalman Filter (LETKF) (Hunt et al., 2007). *Local* means that the analysis is independently computed locally on a reduced analysis grid for each grid point. This makes the LETKF computationally very efficient since it is easy to parallelize.
For atmospheric applications, localization is necessary because the number of observations m as well as the model dimension n is much larger than the degrees of freedom of the analysis state vector in the LETKF provided by the ensemble size N_e. Therefore, all observations within a defined area of influence that can significantly impact the analysis

are included and weighted using a localization function such as the distance-based damping Gaspari-Cohn function (Gaspari and Cohn, 1999). Further, localization reduces spurious correlations due to limitations in the ensemble size.

2.2.3 Global data assimilation system at DWD

The NWP model ICON, developed by DWD and the Max Planck Institute for Meteorology (MPI-M), has been operationally run at DWD since 2015. It is based on the non-hydrostatic system of equations in the global domain (Zängl et al., 2015). In the current operational version, the atmosphere is resolved by a grid of 13 km horizontal mesh size and 90 layers in the vertical. The core module of the global data assimilation system is a Hybrid Variational Ensemble Kalman Filter(VarEnKF), which consists of a LETKF and a 3D-Var data assimilation system. The computationally efficient 3D-Var scheme has the advantage of a well-developed background error covariance model. However, it is static. The LETKF, on the other hand, provides flow-dependent background error covariances, but in general, they are tainted by sampling error. Challenges are mainly caused by localization and the assimilation of nonlinear measured signals such as satellite radiances. The VarEnKF combines the localized ensemble background error covariance matrix from the LETKF $\mathbf{P}^b_{EnKF}$ with the static 3D-Var covariance matrix $\mathbf{P}^b_{NMC}$ used formerly in the 3D-Var:

$$\mathbf{P}^b = \alpha \mathbf{P}^b_{EnKF} + \beta \mathbf{P}^b_{NMC}, \qquad \alpha + \beta = 1 \tag{2.44}$$

In the DWD hybrid data assimilation system, the weights are $\alpha = 0.7$ and $\beta = 0.3$. This combination consistently considers temporal background error covariances with the model dynamics, generating a stable analysis state that incorporates more information from the observations than the pure 3D-Var could (Rhodin et al., 2022). The LETKF is based on a 40-member ensemble with a lower resolution of 40 km and a horizontal localization radius of 300 km. The assimilation is carried out with a 3 h cycling (00, 03, ..., 18, 21 UTC). A 3 h short-term forecast serves as background field that is adjusted using all observations within ± 1.5 h around the corresponding time step to generate the analysis field from which the next forecast is initialized. In the global VarEnKF, the observation operator is directly applied to the model forecast within the core data assimilation module.

Because measurements of atmospheric fields inevitably contain errors, the data must pass quality checks before they are incorporated into the assimilation algorithms. A first guess check compares the departures of the model equivalents from the observations to respective prescribed standard deviation values. Furthermore, observation data with an observation error that is too large are excluded. Observation thinning can be performed to remove redundant information due to correlations of spatially and temporally dense observation sets. In general, these kind of tests can only identify gross errors. Therefore, VarEnKF additionally applies variational quality control (VarQC) that handles remaining outliers. In data assimilation algorithms, the observation errors are assumed to be Gaussian, which is not necessarily true. VarQC assumes more realistic probability density functions for observation errors. At DWD, the modified Huber norm is used. The resulting nonlinearities in the observation cost function can then be accounted for by solving with the Newton method as described in section 2.2.1. Finally, the weight given to the observation as part of VarQC, together with the quality control steps, defines the observation

status (e.g., accepted, active, rejected, passive).

Ideally, the combination of the background and the observations that passed the quality checks minimizes the variance of the analysis with respect to the unknown true atmospheric state (Rhodin et al., 2022). This requires optimal observation and background error covariance matrices, which, however, are not exactly known. Therefore, data assimilation schemes use approximations of the error covariances. The optimization method in the 3D-Var scheme is based on Desroziers and Ivanov (2001) and Chapnik et al. (2004) and relies on the assumption that the background and observation error covariance matrices $\tilde{\mathbf{B}}$ and $\tilde{\mathbf{R}}$, as specified in the assimilation system (Eq. (2.15)), can be brought closer to the optimal matrices $\mathbf{B}$ and $\mathbf{R}$ by a scaling relation:

$$\mathbf{B} = s^b \tilde{\mathbf{B}}, \qquad \mathbf{R} = s^o \tilde{\mathbf{R}}. \tag{2.45}$$

The scaling coefficients s^b and s^o are tuned based on an optimality criterion for the cost function at its minimum, assuming that the correlations are accurately represented in the initially considered error covariances. It is important to note that the tuning is not performed during the assimilation and only offline when necessary.

2.2.4 Observation error components in data assimilation

Adequate assimilation of an observation system requires a detailed quantification of its errors or uncertainties. As already mentioned, the observation error consists of three main components that need to be considered:

1. **Measurement or instrument error:** is the error associated with the measuring device, occurring during the measurement process.

2. **Operator error:** is the error introduced by the computation of the observation operator that usually involves assumptions and approximations to pass from model to observation space. E.g., for the assimilation of radiation observations, $H(x)$ contains a complete radiative transfer model whose uncertainties must be considered.

3. **Representativeness error:** is the error due to unresolved scales and processes. The observed value of a meteorological variable at a single point in space and time is represented in the model as a spatial and temporal average over a grid box. On the other hand, observations corresponding to volume or line measurements are often treated as single-point measurements in the model. Interpolation errors within the observational operator also contribute to the representativeness error. Furthermore, errors associated with imperfections in quality control or pre-processing procedures can introduce representativeness errors (Janjic et al., 2018).

The representativeness and operator errors are often larger than the measurement errors. However, measurement errors are relatively well understood and estimated since they can show proportionality to the measured values (Doviak and Zrnić, 1993).

Chapter 3

Data and methodology

3.1 Data sets and methods for the Aeolus HLOS wind validation study

The following provides a description of the data sets, their processing, and statistical methods relevant for the validation study in Chapter 4. The validation of the Aeolus HLOS winds is performed using three different reference data sets:

1. radiosonde wind observations,
2. ECMWF IFS model equivalents,
3. DWD ICON model equivalents.

To avoid gross outliers in the validation statistics, various thresholds for quality control of the Aeolus HLOS wind observations are applied. Since the Rayleigh and Mie channel of the DWL onboard the Aeolus satellite differ in their sensitivity to error sources, they are treated separately in the evaluation. The largest errors that can occur when comparing spatially and temporally offset observations or dealing with model equivalents are due to representativeness. Typically, the estimation of representativeness errors is based on high-resolution data that are ideally independent of specific weather conditions. In this thesis, a data set of the COSMO-DE analysis as well as ICON Large Eddy Model simulation are used.

3.1.1 Evaluation period and region

The validation study of this thesis concentrates on comparisons of Aeolus HLOS and radiosonde wind observations as well as model equivalents over the time period from 10 September 2018 to 9 January 2020. This covers the Aeolus mission's CP, various processing changes to improve the data quality, and the laser switch from FM-A to FM-B (see timeline Sec. 2.1.4). After 9 January 2020, the operational use of the HLOS winds at ECMWF started, implying that the background is no longer independent of past Aeolus winds.

Since the radiosonde observations from the GOS are rare in the Southern Hemisphere and polar regions (Fig. 1.3c), the validation results are compared for the midlatitudinal band $23.5-65°$ of the Northern Hemisphere. Additionally, model-only global statistics were

performed to place the regional validation results in a global context. The comparisons concentrate on pressure levels above 800 hPa to exclude stronger influences on the HLOS winds of vertical velocity from convection and turbulence in the boundary layer and to avoid any ground return contamination. Furthermore, levels above 80 hPa are excluded due to the small number of collocation pairs.

3.1.2 Collocated radiosonde observations

Radiosonde observations generally provide very accurate information on the true wind profiles. The observation errors between different radiosondes can be assumed to be uncorrelated. Given that radiosonde wind data are direct in situ measurements, the inherent errors (e.g., instrument errors) are small compared to errors of satellite-based instruments. That makes them well suited to serve as reference data set for the true atmospheric state for validating the Aeolus HLOS winds.

At ECMWF, radiosonde feedback files are created from the Observational Data Base (ODB) at the end of the IFS analysis and archived in the Meteorological Archival and Retrieval System (MARS). The radiosonde station reports are provided in two formats: Binary Universal Format for the Representation of meteorological data (BURR) and alphanumeric reports. For stations where ECMWF is assimilating BUFR data (87 % of the radiosonde data), the balloon drift is considered by splitting data into groups of 15 min. Radiosonde feedback files from alphanumeric reports (13 % of the radiosonde data) only contain the time and position of the radiosonde's launch, but not the time and position of the individual wind observations. Insufficient coverage of the radiosonde drift during the sounding and the ascent time can cause additional errors. Seidel et al. (2011) evaluated characteristic values of average drift distances to be 5 km in the mid-troposphere, 20 km in the upper troposphere, and 50 km in the lower stratosphere, tending to be larger in midlatitudes than in the tropics. A few individual radiosondes are found to drift up to 200 km. Estimates of the ascent time of the balloon range from 5 min, when it reaches 850 hPa, up to 1.7 h at 10 hPa. For the definition of collocation criteria for the comparisons with radiosondes, these characteristics should be taken into account.
In this thesis, all radiosonde observations that are within

- 120 km horizontal,
- 90 min temporal,
- 500 m vertical

distance from the Aeolus measurements are used for the validation statistics. For each location, the radiosonde HLOS wind component is computed as a linear function of the zonal wind component u and the meridional wind component v following Eq. (2.9). To achieve a sufficiently large data set, statistics for one day are based on a running mean over seven days.

3.1.3 DWD ICON and ECMWF IFS model equivalents

For a more comprehensive global assessment, the validation results of Aeolus winds with radiosondes are supplemented by a comparison to model equivalents from the global model

ICON of DWD and the ECMWF IFS model. Observation feedback files store the model equivalents $H(\boldsymbol{x}^b)$, together with the original observations $\boldsymbol{y}^o$ and the quality flag information in order to evaluate offline diagnostics in observation space. For the validation, the departures of the model equivalents from the observations (O-B departures) that were screened by the data assimilation system but did not influence the analysis are used.

The deterministic first guess forecast $\boldsymbol{x}^b$ from the operational version of the ICON model is determined from the 3D-Var system with approximately 13 km horizontal grid spacing. Therefore, all observations within the observation window ($\pm$ 1.5 h around the analysis time) are assumed to be valid at the analysis time. The ECMWF operational data assimilation system is based on the 4D-Var technique with a grid spacing of approximately 9 km. Therefore, in contrast to the ICON model, the observations are used at their actual time.

To ensure comparable data sets for the radiosonde and the ECMWF and DWD model validation of the Aeolus winds, only the nearest O-B value per radiosonde collocation is used for the statistics for the midlatitudes on the Northern Hemisphere. A similar approach of limited regions and limited time periods is chosen for the model-only global validation. O-B departures statistics are calculated for regions of 10° latitude x 10° and over periods of seven days before they are averaged for the whole globe. This way, the influence of horizontal and temporal fluctuations of systematic errors on the random errors is reduced.

Due to the homogeneous spatial and temporal distribution of the model data in contrast to the radiosonde observation, the O-B departures serve as a basis for further investigations of bias dependencies.

3.1.4 Quality control criteria for the Aeolus HLOS wind observations

The Aeolus data set is the L2B HLOS wind product from the NRT PDGS processing using baseline 2B02-2B07. The data are obtained from the observation feedback files. To ensure meaningful validation results, various quality control criteria are applied:

- ➢ only observations with valid overall confidence flags are used,
- ➢ only the observation types Rayleigh-clear and Mie-cloudy winds are used, as they are generally of better quality than the other two observation types (from now on referred to as Rayleigh and Mie),
- ➢ Rayleigh winds with range-bin thicknesses of 250 m are rejected because of excessive noise,
- ➢ Rayleigh winds with a horizontal accumulation length < 60 km and Mie winds with horizontal accumulation length < 5 km are rejected due to a large amount of outliers in observation departure statistics,
- ➢ HLOS winds geometric height has been increased by 250 m for the observations until 26 February 2019 due to an error in the star-tracker calibration affecting the LOS pointing knowledge,
- ➢ Rayleigh winds with an L2B processor estimated observation error > 8 m s^{-1} are excluded,

➢ Mie winds with an L2B processor estimated observation error > 6 m s^{-1} are excluded,

➢ specific range-bins that are affected by hot pixels are excluded from the validation statistic before the implementation of the correction scheme into the operational processor chain.

(a) *Rayleigh*

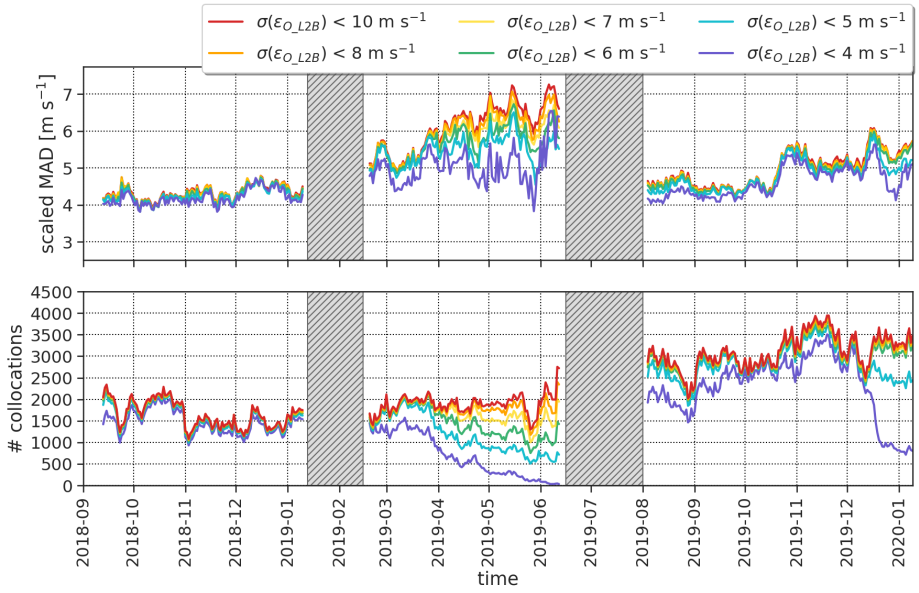

(b) *Mie*

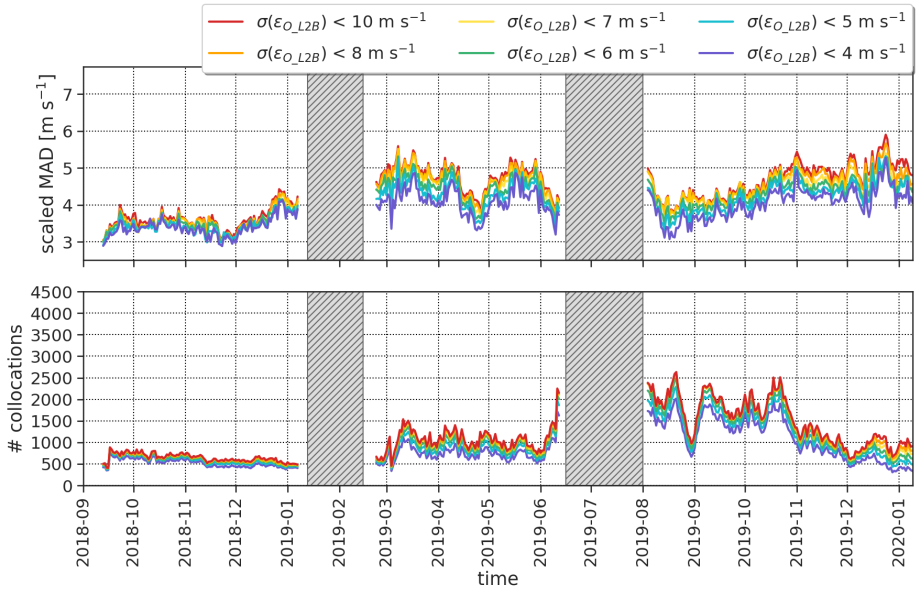

Figure 3.1: *Temporal evolution of collocated observation pairs available for the radiosonde comparison and the random differences in terms of the scaled MAD [m s^{-1}] for (a) Rayleigh and (b) Mie HLOS wind observations. Different colors display different thresholds for the L2Bp estimated observation error.*

L2Bp estimated observation error threshold

The L2B processor estimated observation error is an essential measure of the quality control criteria. Applying an L2Bp estimated error threshold for Rayleigh and Mie HLOS wind observations avoids gross outliers in the validation. For optimal use of the Aeolus observations, the threshold should ensure that a sufficient amount of collocated data can be used without introducing inconsistencies in data quality. A very strict L2Bp estimated error threshold decreases the random differences but would also reduce the number of Aeolus observations usable for the validation statistics. Fig. 3.1 illustrates this relation for Rayleigh and Mie, showing all collocated observation pairs available for the radiosonde comparison for the validation period (collocation criteria are defined in Sec. 3.1.2) together with the random differences (in terms of scaled median absolute deviation (MAD), see Sec. 3.1.6). During the CP, the influence of the L2Bp estimated error threshold is small. However, for the time before the switch from laser FM-A to FM-B (March - July 2019), different L2Bp estimated error thresholds lead to large differences in the number of available collocation pairs, especially for the Rayleigh observations. It turned out that the L2Bp estimated error had a bug in the baselines 2B02-2B04. Due to large UV solar background noise, it overestimated the error in daylight conditions. In particular, the Rayleigh wind random error depends on the solar background radiation. Thus, the effect is much stronger than for the Mie wind observations. During the summer months 2019 in the Northern Hemisphere, the L2Bp estimated errors are all too large, meaning a quality control with a threshold, e.g. 6 m s^{-1} for the Rayleigh wind observations becomes a stricter quality control for this period. After the switch to laser FM-B towards the winter season and with updated baselines, the differences between different L2Bp estimated error thresholds become smaller. However, a too low threshold still will lead to strong deviations in the number of comparable observations. Based on a trade-off, a threshold of 8 m s^{-1} for Rayleigh and 6 m s^{-1} for Mie is assumed to be a reasonable choice to ensure consistent validation statistics.

3.1.5 Representativeness errors

The knowledge of the representativeness errors is key to determining the Aeolus observational error of the Aeolus winds. The validation statistics include several representativeness error sources:

Firstly, representativeness errors arise due to different measurement geometries of the compared data sets. Whereby the Aeolus HLOS wind observations correspond to line measurements, the NWP models treat the Aeolus HLOS winds as point measurements. Radiosonde observations can also be interpreted as a point measurement.

The estimation of the representativeness error for the comparison of radiosonde and the Aeolus data includes three further error sources:

- the spatial and temporal difference resulting from the collocation criteria,
- the spatial and temporal difference resulting from the displacement during the radiosonde ascents when radiosonde data from alphanumeric reports are assimilated,
- the temporal offset value for the grouping time interval when accounting for balloon drift in BUFR data.

Data sets for the estimation of the representativeness errors

The different components of the representativeness errors are estimated using analysis data of the COSMO limited-area model for Germany (COSMO-DE) of five seven-day periods (February, April, June, October, and December 2016). The COSMO-DE model covers Germany, Switzerland, Austria, and parts of other neighboring states and has a horizontal grid spacing of 2.8 km and 50 levels in the vertical. The data are only used up to 12 km to avoid influences of large model errors and uncertainties of the simulation in the stratosphere. To determine the effect of unresolved scales in the COSMO-DE analyses, the results are compared to a three-day (3 to 6 June 2016) high-resolution ICON Large Eddy Model (ICON-LEM) simulation centered over Germany with 150 m horizontal resolution and 150 levels in the vertical. This way, an offset value is calculated, which is added to the representativeness errors. The entire procedure for estimating the representativeness errors is outlined in the results chapter (section 4.2.1).

3.1.6 Statistical metrics

For the Aeolus HLOS wind validation using the NWP models as reference, the systematic observation error can be estimated as:

$$E(\boldsymbol{\epsilon}_{HLOS}) = E(\boldsymbol{y}^{HLOS} - H(\boldsymbol{x}^b)) + E(\boldsymbol{\epsilon}_b) \approx E(\boldsymbol{y}^{HLOS} - H(\boldsymbol{x}^b)), \tag{3.1}$$

with the HLOS observation operator H following Eq. (2.9). For long validation periods and large spatial scales, the systematic model error is usually small compared to that of Aeolus observations. Thus, the mean systematic difference between the Aeolus observations and the background (O-B departure) can be referred to as bias:

$$\text{BIAS} \approx \frac{1}{\text{N}} \sum_{i=1}^{\text{N}} v_{\text{diff}}^{\text{HLOS}} = \frac{1}{\text{N}} \sum_{i=1}^{\text{N}} (y_i^{HLOS} - H(x_i^b)), \tag{3.2}$$

where i represents the time step and N is the number of compared data points. However, in certain conditions, such as in jet stream regions, the tropical upper troposphere, and the stratosphere, Aeolus HLOS bias estimates based on NWP monitoring statistics should be treated with caution.
For the Aeolus HLOS wind validation using radiosonde observations as reference, the bias can be estimated according to:

$$\text{BIAS} \approx \frac{1}{\text{N}} \sum_{i=1}^{\text{N}} v_{\text{diff}}^{\text{HLOS}} = \frac{1}{\text{N}} \sum_{i=1}^{\text{N}} (\text{HLOS}_i^{\text{L2B}} - \text{HLOS}_i^{\text{Radiosonde}}). \tag{3.3}$$

To quantify the random deviations, the standard deviation

$$\sigma = \sqrt{\frac{1}{\text{N-1}} \sum_{i=1}^{\text{N}} (v_{\text{diff}}^{\text{HLOS}} - \text{BIAS})^2}, \tag{3.4}$$

as well as the scaled MAD

$$\text{scaled MAD} = 1.4826 * \text{median}(|v_{\text{diff}}^{\text{HLOS}} - \text{median}(v_{\text{diff}}^{\text{HLOS}})|), \tag{3.5}$$

is determined for the three reference data sets. The MAD is a robust measure for the variability of the Aeolus HLOS winds, being more resilient to single outliers than the standard deviation. In the case of a normally distributed data set, the MAD value multiplied by 1.4826 (scaled MAD) is identical to the standard deviation (Ruppert and Matteson, 2015).

3.2 Data sets and methods to assess the impact of Aeolus HLOS wind assimilation

3.2.1 Experimental set up

Observing system experiment (OSE)

An effective way to assess the impact of an existing observation network in an NWP model is to conduct an OSE (Bouttier and Kelly, 2001, Kelly and Thépaut, 2007). In an OSE, two continuous assimilation cycles are performed: A control run which typically uses the operational model and observation set, and an experimental run in which the observation type of interest is either added or removed. Comparisons of the resulting analyses and corresponding forecasts then serve as the basis for a systematic impact study.

In this thesis, the impact of the Aeolus L2B HLOS wind observations is assessed using the operational version of the global model ICON at DWD (Sec. 2.2.3) at its full resolution (13 km). The control run (CTRL) is performed without the Aeolus but with all other operationally used observation types assimilated. In the experimental run (EXP_A), the Rayleigh and Mie HLOS wind observations are assimilated in addition to all other observation types. Both assimilation experiments were conducted with a corresponding cycled LETKF ensemble run to provide individual background error covariance estimates for the experiments. For EXP_A, the model background winds u and v are interpolated to the Aeolus observation geolocation point (latitude, longitude, and height) and transformed to the Aeolus HLOS wind equivalents using the observation operator following Eq. (2.9). Thus, the HLOS winds are assumed as point observations with neglected vertical velocity. This is a reasonable approach since the effective model resolution of ICON is between 80 and 100 km in the horizontal and between a few hundred meters (lower troposphere) up to 2 km (stratosphere) in the vertical, which is approximately the same size as the averaging length scale of the Rayleigh HLOS winds. The Mie winds' averaging box is about a factor of 10 smaller, but no thinning is applied.

Random observation error estimates

Figs. 3.2a and 3.2b display the random error estimates of the Aeolus HLOS wind observations in the OSE as function of altitude, including the observation error provided by the L2B processor $\sigma(\epsilon_{O\_L2B})$, the observation error assigned in the assimilation $\sigma(\epsilon_{O\_ass})$ and the standard deviation of the O-B departures $\sigma(O-B)$. The latter consists of the random

error estimate of the Aeolus winds $\sigma(\epsilon_O)$ and the background model error $\sigma(\epsilon_b)$:

$$\sigma(O-B) \approx \sqrt{\sigma(\epsilon_O)^2 + \sigma(\epsilon_b)^2} \tag{3.6}$$

Together with the assigned observation error, the background model error determines how closely the analysis field is drawn to the Aeolus observations compared to the background. Low assigned observation errors and large model errors allow Aeolus wind observations to have a more significant impact. The background model error shows the largest values at around 150 hPa for the Mie wind model equivalents and around 300 hPa for the Rayleigh wind model equivalents. The assigned observation error in the OSE is smallest in the middle troposphere and increases towards lower and stratospheric levels. It is derived based on the Desroziers method (Desroziers et al., 2005) and used in a table-driven format for specific pressure levels (Fig. 3.2c). Between these levels, it is interpolated.

(a) *Rayleigh* ***(b)*** *Mie* ***(c)*** *assigned observation error*

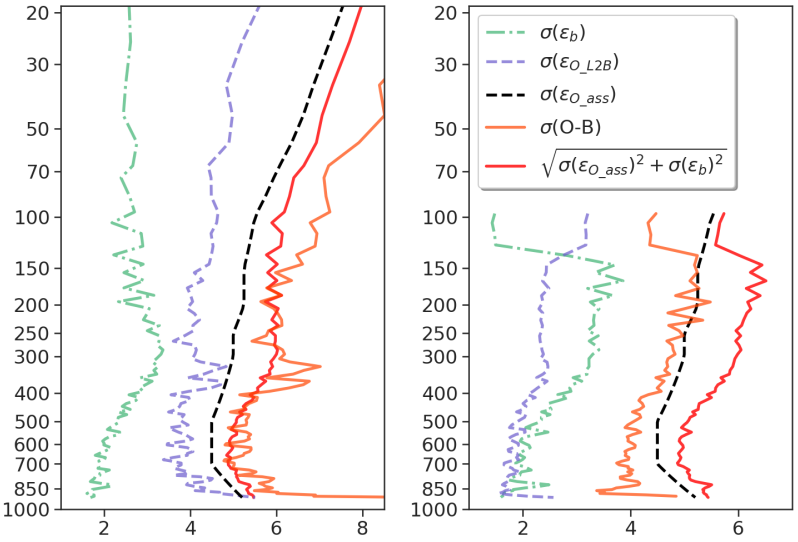

level [hPa]	$\sigma(\epsilon_{O\_ass})$ [m s^{-1}]
10	8.00
20	7.50
30	7.00
50	6.50
70	6.00
100	5.50
150	5.25
200	5.25
250	5.00
300	5.00
400	4.75
500	4.50
700	4.50
850	5.00
1000	5.50

Figure 3.2: *Random error estimates of the Aeolus Rayleigh (a) and Mie (b) HLOS wind observations as function of pressure [hPa] for 01 July 2020 to 30 September 2020, including: the background model error $\sigma(\epsilon_b)$ (green), the L2B estimated observation error $\sigma(\epsilon_{O\_L2B})$ (purple), the assigned observation error $\sigma(\epsilon_{O\_ass})$ (black), the standard deviation of the O-B departures $\sigma(O-B)$ (orange) and the random error estimate when combining $\sigma(\epsilon_{O\_ass})$ and $\sigma(\epsilon_b)$ (red). Table (c) displays the values of the assigned observation error $\sigma(\epsilon_{O\_ass})$ for specific pressure levels.*

The assigned observation error is generally larger than the observation error estimated by the L2B processor, which does not include the uncertainties due to representativeness. These differences are more pronounced for Mie winds than for Rayleigh winds. However, the increase of $\sigma(\epsilon_{O\_ass})$, $\sigma(\epsilon_{O\_L2B})$ and $\sigma(O-B)$ with height agrees relatively well, indicating a higher precision of Aeolus observations in the mid-troposphere compared to upper levels. Both the Rayleigh estimated L2B error and the standard deviation of O-B departures appear to be increased at pressure levels between 300 and 400 hPa. The Rayleigh wind random errors, among other things, depend on the atmospheric path signal and are therefore influenced by the signal accumulation (vertical and horizontal). In summer 2020,

the range bin setting in the tropics ±30° latitude (VENUS) and the range bin setting in the extratropics > 30°N and between -30° and -60°S (BRC_518_1) was adjusted by increasing the vertical sampling around the jet stream between 5 – 10 km. Improvements from the optimized range bin setting are mainly expected from the higher number of Mie observations since clouds usually generate high levels of noise at these levels. The larger random errors in the Rayleigh winds are probably related to these smaller range bins.

For a consistency check on how well the assigned observation error represents $\sigma(\epsilon_O)$ in the assimilation system, it is combined with the background model error as follows:

$$\sigma_{consistency\_check} = \sqrt{\sigma(\epsilon_{O\_ass})^2 + \sigma(\epsilon_b)^2} \tag{3.7}$$

Ideally, this corresponds to the standard deviation of the O-B departures. The profiles of $\sigma(O-B)$ and $\sigma_{consistency\_check}$ match quite well for Rayleigh winds, except for small discrepancies in the discussed levels with increased vertical resolution and above the tropopause, where either the assigned observation error or the ensemble spread is too small. The Mie winds show deviations of about 1 m s^{-1} indicating that slightly too low weight is assigned to them. Usually, the Mie observations tend to be more precise compared to Rayleigh because the backscatter signal from clouds is about an order of magnitude larger than during clear-sky conditions, and Mie observations are not affected by Doppler broadening due to Brownian motion. The VarQC included in the DWD assimilation system can partly compensate for inconsistencies in the assigned observation error. It operates during the iterative minimization as part of the solution of the variational problem and reduces the weight of observations with large deviations compared to its statistical expectation. It is more active for observations with low assigned errors and less active in the case of large assigned errors. Therefore, the resulting VarQC weight of Rayleigh winds is smaller than that of Mie winds (not shown). Overall, the data quality and monitoring statistics are fairly constant throughout the OSE period.

Quality control settings and bias correction for the OSE

Since the quality control criteria for the validation study (Sec. 3.1.4) are found to be reasonable, they also serve as the quality control basis for the OSE. The impact of the Rayleigh and Mie HLOS wind observations in the ICON model is assessed for a three-month period during the Northern Hemisphere summer, July 2020 - October 2020. The Aeolus data of this period are processed using the baseline 2B10, including an NRT bias correction method. During the first part of the mission, validation studies showed large systematic differences, which vary seasonally, spatially, and with orbital phase - particularly pronounced for the Rayleigh wind observations (Sec. 4.3). The operationally implemented bias correction is based on a multiple linear regression method of ECMWF O-B statistics and the thermistors of the telescope M1-mirror, eliminating most part of the bias. However, the DWD system still shows a small residual bias that depends on altitude for the Rayleigh wind observations.

Fig. 3.3 shows the mean departures between the HLOS wind observations (O) and the short-range forecast model equivalent HLOS winds (B). For both orbit phases, a bias with negative values in the troposphere and positive values around the tropopause and in the lower stratosphere is apparent for the Rayleigh wind observations (Figs. 3.3a and 3.3b). The

height-dependency is assumed to be related to the atmospheric background temperature used for the Rayleigh–Brillouin correction (Šavli et al., 2021). However, the investigations of this effect are still in progress. In total, the magnitude of the mean O-B departure is small ($< \pm 1$ m s^{-1}), but to further optimize the assimilation of the Aeolus HLOS winds in the ICON model, an additional model-based bias correction is implemented for the OSE. The bias correction uses the approach outlined in Sec. 4.3.1 and is a function of latitude conducted for specific height levels: surface-850 hPa, 850-500 hPa, 500-200 hPa, 200-70 hPa, 70-5 hPa. It is based on the previous seven days and applied to the HLOS winds separately for ascending and descending orbits.

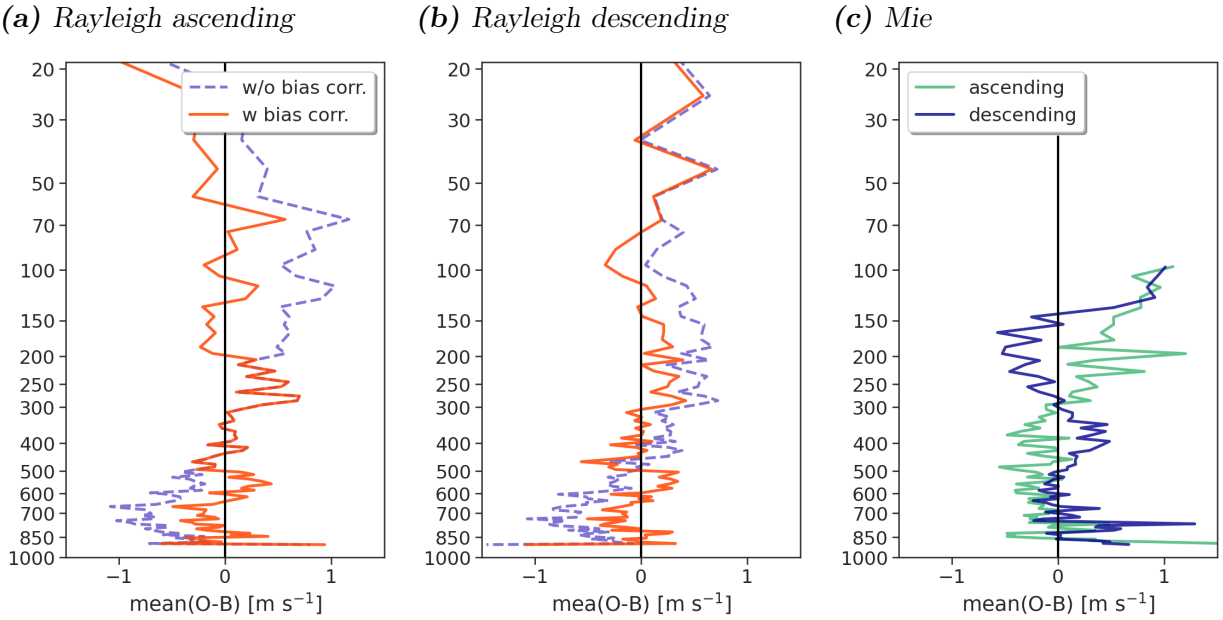

Figure 3.3: *Mean O-B departures (bias) as function of pressure [hPa] of the Aeolus HLOS Rayleigh ascending (a) and descending (b) winds for 01 July 2020 to 30 September 2020 - without bias correction (orange dashed line) and with bias correction (green solid line) - and for the Aeolus HLOS Mie winds (c) separately for ascending (cyan) and descending (blue).*

For levels below 500 and above 200 hPa, this bias correction reduces the differences between Aeolus winds and NWP model background winds to almost zero, thus eliminating the height dependency of the bias. On average, the residual absolute systematic deviations are about 0.2 m s^{-1}, i.e., half as large as without the model-based bias correction. The Mie bias is not as much related to the atmospheric background temperature and thus does not show a height dependency. After the M1-mirror-temperature-dependent bias correction, the additional model-based bias correction does not improve the Mie HLOS winds further. Whereas the Aeolus Rayleigh wind bias does not differ significantly between ascending and descending orbits, the Aeolus Mie bias (Fig. 3.3c) exhibits a dependence on the orbit phase. A similar pattern can be seen in the weekly monitoring routine at ECMWF, suggesting that these systematic errors are Aeolus and not model biases. According to Marseille et al. (2022), the systematic Mie errors are due to imperfections of the data in the absolute instrument calibration tables, which serve as input for the on-ground wind processing algorithms. An updated calibration table for the Mie channel based on NWP model winds

that reduces the bias and is part of the operational processing chain since 01 July 2021. However, the processor baseline of the OSE period is an older version. The magnitude of the absolute bias of the assimilated Mie winds is about 0.2 m s^{-1} for ascending and 0.3 m s^{-1} for descending orbits, thus, comparable to the Rayleigh wind bias.

3.2.2 Verification data and methods

For assessing the systematic impact of the Aeolus HLOS wind observations, analysis fields and the forecast errors of the CTRL and EXP_A experiment are compared. In general, forecast errors are defined as the differences between the forecast provided by an NWP model and the true atmospheric state. Typically, either NWP analyses at the time the forecast is valid or a statistically significant sample of observational data of other observation types is used to represent a reliable proxy for the "truth". However, it should be noted that these proxies contain their own errors depending on the choice of the verification data. For example, the error of short-range forecasts is likely correlated with that of the analysis leading to potential systematic errors in such a verification, especially if the same modeling system is used (Geer et al., 2010).

In this thesis, short-term forecasts up to 36 h are verified against measurements from a selection of other observation types (radiosondes, aircraft, GPSROs, and AMVs). These observations are, to a large extent, independent of the evaluated forecasts.

For the verification of longer forecast lead times, ERA5 reanalysis data are used as analyses. The ERA5 output is produced using the 4D-Var data assimilation of the ECMWF IFS at a horizontal resolution of 31 km and with 137 vertical model levels up to the height of 80 km (from 1000 hPa to 1 hPa, with 40 levels below 5 km) (Hersbach et al., 2020). As ERA5 reanalyses are based on a different model with different resolution compared to the OSE, they provide a relatively independent data source. The higher vertical resolution of ERA5 allows finer details of atmospheric phenomena to be resolved, such as a more realistic representation of atmospheric waves and their interaction with the mean flow, which is especially crucial for the study of QBO in Sec. 5.2.1. Furthermore, ERA5 assimilates a partly different set of observations than the global data assimilation system in the ICON model (e.g., more satellite radiances) and does not use the Aeolus observations. It is well known that NWP models in the stratosphere are typically subject to large uncertainties. ERA5 was found to have a cold bias in the lower stratosphere and a warm bias near the stratopause (Hersbach et al., 2020). However, the increased number of assimilated GPSRO bending angles in ERA5 since 2006 has significantly reduced this model bias, increasing confidence in using the stratospheric reanalyses for verification (Laloyaux et al., 2020a).

The forecast error of an experiment X is calculated as:

$$e_i^X = forecast_i^X - analysis_i^Y . \tag{3.8}$$

For this study, X is either the CTRL or the EXP_A run, Y is the verification data (observation or ERA5 reanalysis data), and i represents the time step when the forecast and analysis are valid, respectively. The root-mean-squared error (RMSE) of the experiment X determines how strongly the forecast deviates from the verification data:

$$RMSE(e^X) = \sqrt{\overline{(e_i^X)^2}} . \tag{3.9}$$

Depending on the requested dependency, the mean (denoted by the overbar in Eq. (3.9)) is either calculated over time, pressure level, latitude or longitude, or over several dimensions. Improvement or degradation of the forecast quality through the assimilation of Aeolus observations can then be assessed by the differences between $RMSE(e^{EXP\_A})$ and $RMSE(e^{CTRL})$. Because the RMSE depends on the magnitude of forecasts and observations, all results are additionally verified by calculating the normalized RMSE differences:

$$e_{diff} = \frac{RMSE(e^{EXP\_A}) - RMSE(e^{CTRL})}{RMSE(e^{CTRL})}. \tag{3.10}$$

Chapter 4

Results: Validation of Aeolus HLOS wind observations

A crucial prerequisite for using meteorological observations in NWP data assimilation systems is a comprehensive knowledge of their errors. Typically, the performance of a meteorological data set is characterized by comparisons with high-quality and well-established measurements from other observation systems. Radiosonde observations generally provide very accurate information on the true wind profiles with small errors (e.g., instrument errors) compared to satellite-based instruments. However, radiosondes are predominantly concentrated over Northern Hemisphere continents. Therefore, the validation study of the Aeolus HLOS wind observations presented in this chapter additionally includes comparisons with model equivalents from the DWD global model ICON and the ECMWF IFS system. Using a similar approach to calculate the systematic and random differences of the observation and model-based comparisons (Sec. 3.1.3), it is possible to produce comparable regional and global validation statistics. Since the DWL onboard the Aeolus satellite measures both molecular (Rayleigh) and particulate (Mie) backscatter, and these differ in their sensitivity to systematic and random sources of error, the validation is performed separately for Rayleigh and Mie. Furthermore, differences were found depending on whether the satellite is in the ascending (instrument pointing eastward) or descending (instrument pointing westward) phase of its polar orbit; therefore, the statistics are split accordingly. In particular, four main topics are covered in this chapter:

- the temporal evolution of the systematic and random differences,
- the determination of the Aeolus observational error, including the estimation of the representativeness errors of the validation
- the investigation of bias dependencies,
- an approach to correct for the bias.

4.1 Temporal evolution of systematic and random differences

Fig. 4.1 and Fig. 4.2 display the temporal evolution of the Aeolus HLOS wind systematic and random differences when using radiosonde observations and model equivalents from

the ECMWF IFS and the DWD ICON model around the collocated radiosonde locations as reference data sets. An overview of the mean absolute systematic differences and the mean scaled MAD values over the whole validation period is provided by Table 4.1. In addition to the validation around the radiosonde collocation pairs on the Northern Hemisphere midlatitudes, the results of the model-only validation on a global scale are listed.

Assessing the temporal evolution of the systematic differences, it is apparent that the quality of the Aeolus observations varies a lot over time. To some extent, this is caused by six different processor baselines and several updates of the calibration files during the selected time period, which makes the data partly inconsistent and incompatible. Right after the Aeolus launch, the Rayleigh wind observations of the ascending phase exhibit negative systematic differences, whereas the systematic differences of the descending phase are positive. With time, the systematic differences increase for both orbit phases. Comparing Rayleigh and Mie, the temporal evolution is relatively similar until the laser switch in June 2019. In January 2019, the satellite's GPS unit experienced a restart anomaly that caused the ALADIN instrument to be in stand-by mode for about one month (grey shaded area). After the stand-by period, the systematic differences reach their maxima. For the Rayleigh wind observations of the ascending orbit phase, the maximum is at the end of February 2019, with values up to 4 m s^{-1}. The Rayleigh descending and the Mie wind observations reach the maximum systematic differences later, around April 2019. Related to an update of the processor setting file end of May, the systematic differences show a sharp decline for both channels and orbit phases. For the Rayleigh wind observations, the decrease is about 4 to 5 m s^{-1}, resulting in negative values, while the Mie wind systematic differences fluctuate around zero. Overall, the Mie wind observations show stronger fluctuations in the systematic differences than Rayleigh for the first part of the validation period. This is probably linked to the sparser coverage of the Mie winds and the higher variability and larger model error when clouds are present. After the switch to the second laser FM-B, which caused a second longer period without data, the validation study continues when the new calibration files were implemented. After the laser switch, the strong fluctuations in the systematic differences of the Mie wind observations are reduced. They show quite constant and very small values for late summer and autumn. In contrast, the systematic differences of the Rayleigh wind observations are still relatively large in these months. Furthermore, they differ between the two orbit phases. The Rayleigh wind observation of the descending orbital phase exhibit positive systematic differences between 2 and 3 m s^{-1} in August 2019, tending to negative during the respective processor baseline period. The systematic differences of the ascending orbit vary between -3 and 0 m s^{-1}. Towards the end of 2019, when the systematic differences of the Rayleigh wind observations are negative for both orbit phases, a sharp increase occurs in mid-December. This is caused by a manual L2B processor bias correction of +4 m s^{-1} in the Rayleigh wind product to compensate for a global average bias drift.

The three different reference data sets agree very well in estimating the bias, raising confidence that the results are not determined by model biases. The small discrepancies in the validation of the Mie wind observations are likely due to uncertainties and differences in NWP models in cloudy regions. In total, the mean absolute systematic differences of the validation against radiosonde observations and DWD model equivalents are quite close, whereas the systematic differences when comparing the HLOS wind observations to IFS model equivalents are slightly smaller. This is probably due to different assimilated observa-

(a) Rayleigh ascending

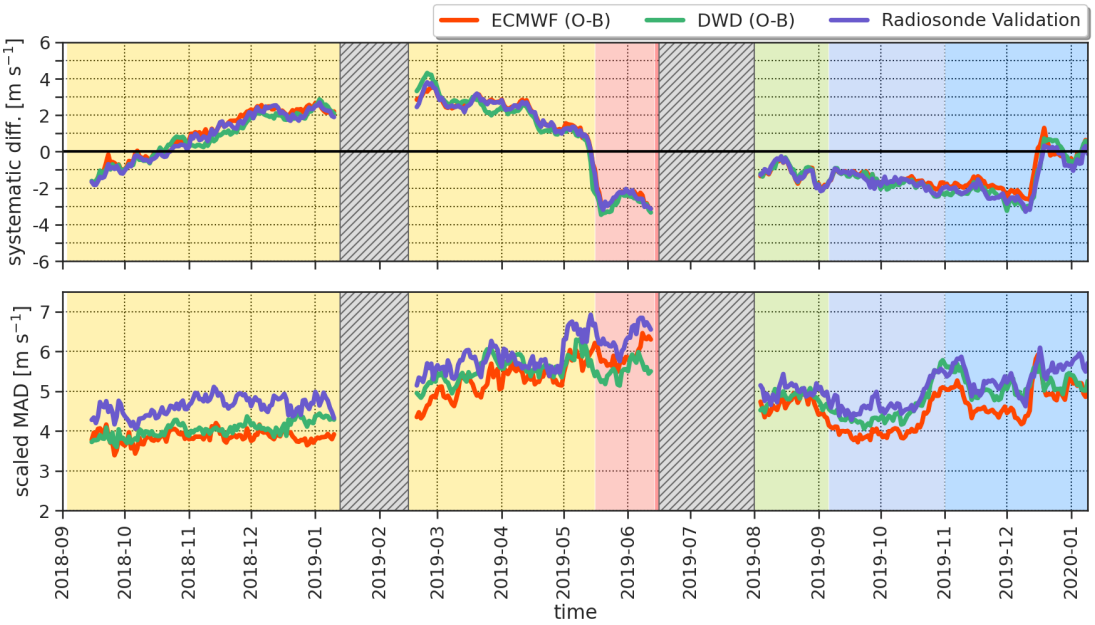

(b) Rayleigh descending

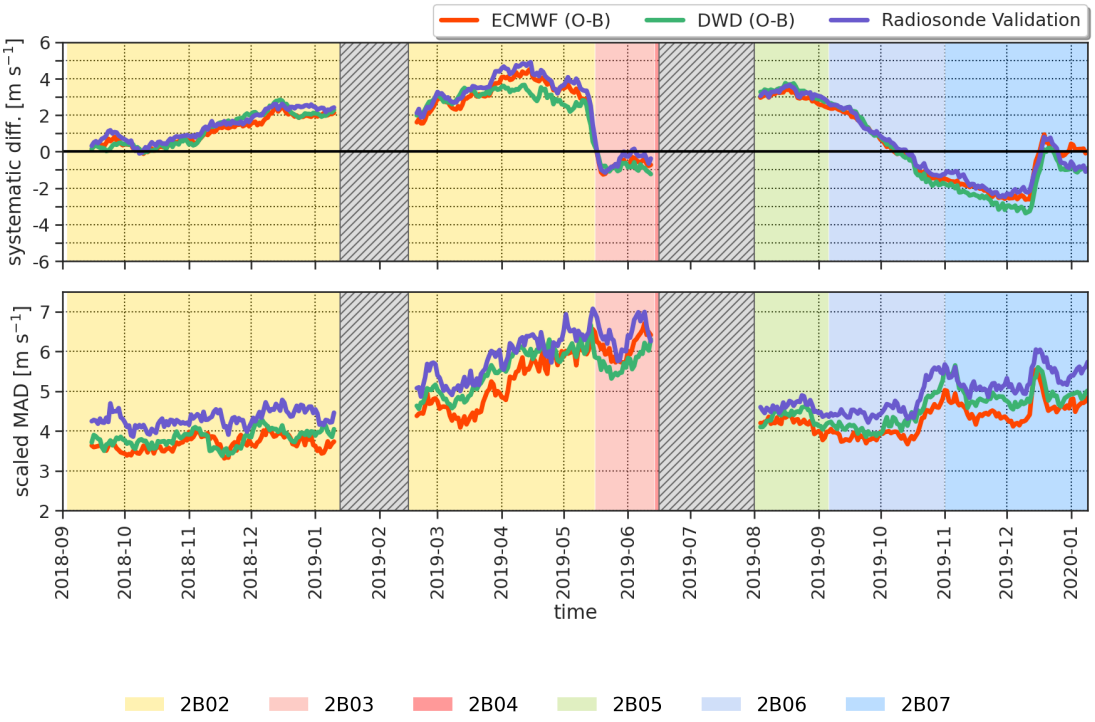

Figure 4.1: *Temporal evolution of the bias estimate, and scaled MAD of Rayleigh (a) ascending and (b) descending HLOS winds for the Northern Hemisphere ($23.5 - 65°N$), using collocated radiosonde observations (purple) and model equivalent statistics (O-B) around the collocation points of the ECMWF IFS model (orange) and the ICON model of DWD (green). The background colors indicate the different processor baselines.*

(a) Mie ascending

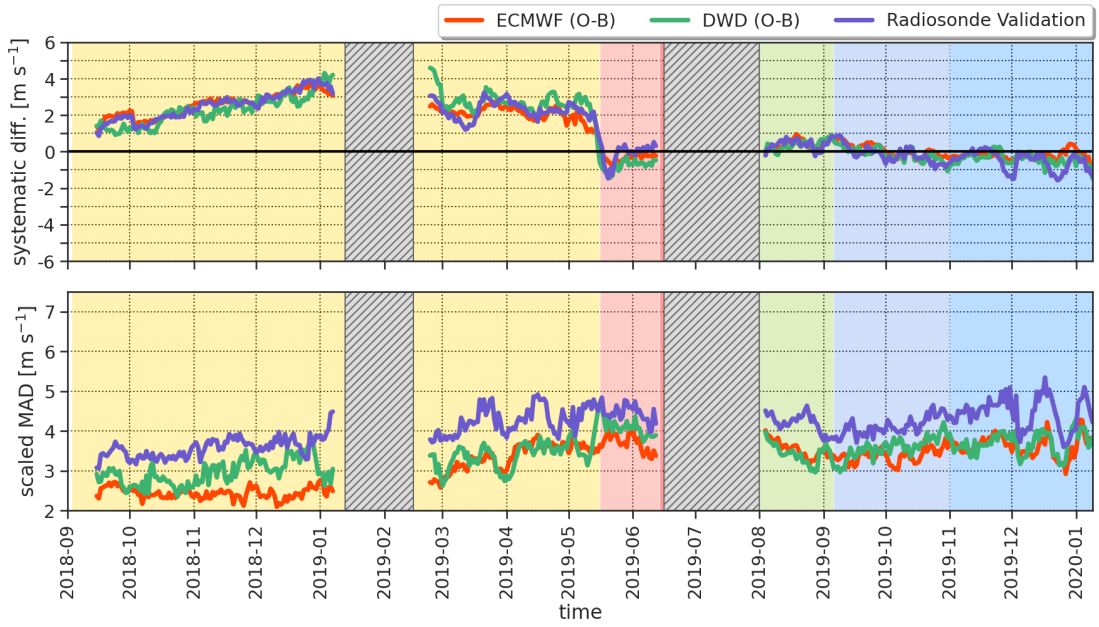

(b) Mie descending

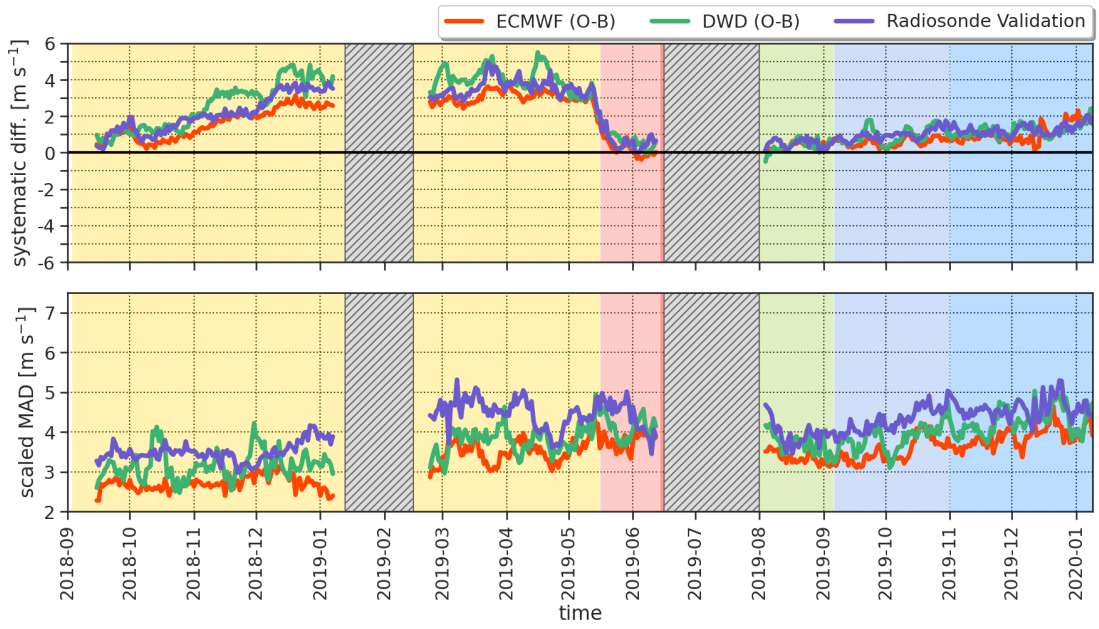

Figure 4.2: *Same as Fig. 4.1, but for Mie wind observations.*

tion data sets at ECMWF and DWD. At the ECMWF, the number of assimilated satellite observations, which typically strongly influence the background state, is higher than at the DWD. Consequently, radiosonde observations potentially have a higher weighting in the DWD's assimilation system than at the ECMWF. The globally derived mean absolute systematic differences of the Rayleigh wind observations, which are based on O-B statistic of limited areas (10° latitude x 10° longitude) and periods (seven days), are slightly smaller compared to the model validation results of the restricted areas on the Northern Hemisphere. However, for the Mie wind observations, the global statistic shows mainly larger values.
Besides the observed temporal changes in the quality of the Aeolus Rayleigh and Mie wind observations, the discrepancies between the ascending and descending orbit phase, mainly for the Rayleigh channel, are a challenging issue for using these data in NWP models. Thus, to reduce the Aeolus HLOS wind bias of -3 up to 5 m s^{-1}, a bias correction scheme is required that considers both seasonal and orbit phase variations.

	Rayleigh ascending		Rayleigh descending	
	systematic diff.	1.4826*MAD	systematic diff.	1.4826*MAD
Radiosondes NH	1.70	5.20	1.95	5.05
ECMWF NH	1.65	4.59	1.77	4.43
DWD NH	1.69	4.82	1.89	4.64
ECMWF global	1.47	4.51	1.73	4.41
DWD global	1.48	4.77	1.76	4.69
	Mie ascending		Mie descending	
	systematic diff.	1.4826*MAD	systematic diff.	1.4826*MAD
Radiosondes NH	1.45	4.08	1.85	4.13
ECMWF NH	1.36	3.17	1.46	3.34
DWD NH	1.48	3.40	2.06	3.72
ECMWF global	1.66	2.89	1.78	2.90
DWD global	1.67	3.00	2.21	3.07

Table 4.1: *Overview of the Aeolus HLOS wind mean absolute systematic differences [m s^{-1}] and the mean scaled MAD values [m s^{-1}] as estimates for the mean absolute bias and random error. The values are averaged from 10 September 2018 to 09 January 2020 over the Northern Hemisphere ($23.5 - 65°N$), restricted to the radiosonde collocation areas (3 top-most rows). In addition, the bottom rows show the values for a global model-only statistic.*

The random differences of the Rayleigh wind observations calculated based on model O-B statistics vary between 3 and 6 m s^{-1} within the considered validation period. For the comparison with radiosonde observations, the random differences are larger, ranging from 4 up to 7 m s^{-1}. This can be explained by the larger representativeness errors associated with radiosondes. Besides the higher spatial resolution of a radiosonde observation compared to the resolution of a global NWP model, representativeness errors arise from the chosen collocation criteria and the spatial and temporal displacement during the radiosonde ascents (Sec. 3.1.5). These error sources are considered in the estimation of the Aeolus wind

observational error in the following Sec. 4.2. Comparing the two NWP models, the mean scaled MAD calculated with the ECMWF model is, on average, about 0.25 m s^{-1} smaller than when using O-B statistics of the DWD global model. Likely, this is the result of neglecting the temporal evolution within the assimilation window in the DWD system. On a global scale, the mean scaled MAD values are slightly smaller than the model validation results of the restricted areas in the Northern Hemisphere.
For the wind observations of both channels, an increase in the scaled MAD occurs from the Aeolus launch until the laser switch in summer 2019. Overall, the random differences for the Rayleigh are larger than for the Mie wind observations because the return signal from clouds is typically stronger and further not affected by Doppler broadening. Also, the increase during the laser FM-A period is much stronger for the Rayleigh wind observations. Mainly, the larger random differences are associated with the energy decrease of the FM-A laser over time. However, the Rayleigh HLOS wind random error also depends on other factors influencing the atmospheric path signal. Besides the output laser pulse energy, the solar background noise can impact the data quality. Probably, this is another contribution to the strong increase in random differences during the early Northern Hemisphere summer. The laser switch and new improved calibration files led to a successful reduction of 1-1.8 m s^{-1} in the random differences of the Rayleigh wind observations. The Mie return signal primarily depends on the presence of aerosols or hydrometeors and not on the laser energy. Therefore, the random differences are almost unchanged after the laser switch. Since mid-October 2019, the random differences again show a slight increase for both channels. Nevertheless, the increase is much smaller compared to the period before the laser FM-B phase.

4.2 Aeolus HLOS wind validation error estimates

The total variance of the difference between radiosonde observations and Aeolus HLOS winds $\sigma(\epsilon_{val\_RS})$, represented by the squared scaled MAD, is generally the sum of the variance resulting from the Aeolus wind observational error $\sigma(\epsilon_{o\_A})$, the variance resulting from the radiosondes wind observational error $\sigma(\epsilon_{o\_RS})$, and the variance caused by the representativeness error $\sigma(\epsilon_{r\_RS})$. Therefore, the Aeolus wind observational error from the radiosonde validation can be estimated using the following formula:

$$\sigma(\epsilon_{o\_A}) = \sqrt{\sigma(\epsilon_{val\_RS})^2 - \sigma(\epsilon_{o\_RS})^2 - \sigma(\epsilon_{r\_RS})^2} \tag{4.1}$$

For the comparison with model equivalents, the model representativeness error $\sigma(\epsilon_{r\_ECMWF})$ and $\sigma(\epsilon_{r\_DWD})$ are used and $\sigma(\epsilon_{o\_RS})^2$ is replaced by the model errors $\sigma(\epsilon_{b\_ECMWF})$ and $\sigma(\epsilon_{b\_DWD})$:

$$\sigma(\epsilon_{o\_A}) = \sqrt{\sigma(\epsilon_{val\_ECMWF})^2 - \sigma(\epsilon_{b\_ECMWF})^2 - \sigma(\epsilon_{r\_ECMWF})^2} \tag{4.2a}$$

$$\sigma(\epsilon_{o\_A}) = \sqrt{\sigma(\epsilon_{val\_DWD})^2 - \sigma(\epsilon_{b\_DWD})^2 - \sigma(\epsilon_{r\_DWD})^2} \tag{4.2b}$$

4.2.1 Representativeness error

To achieve an estimate of the representativeness error, COSMO-DE analyses of different seasons of the year 2016 are used. The model representativeness error is calculated by comparing the point-like measurement geometry of the HLOS wind model equivalents with the measurement geometry of the Aeolus observations. An Aeolus observation can be regarded as the average value of a 90 km line for the Rayleigh winds and Mie winds till 5 March 2019, and as the average value of a 10 km line for the Mie winds after 5 March 2019. As the Aeolus HLOS winds mainly correspond to the zonal wind component, only the differences in u between a single point and a horizontal line average are determined. The calculation is performed for the whole COSMO-DE model domain, and the values are averaged over the height levels corresponding to the Aeolus range bin setting weighted by the mean number of Aeolus wind measurements of the Rayleigh and the Mie channel (Fig. 4.3a). The resulting representativeness error for the IFS and ICON model is 0.50 m s^{-1} for the Rayleigh wind observations, 0.52 m s^{-1} for the Mie wind observations with 90 km horizontal resolution, and 0.12 m s^{-1} for the Mie wind observations with 10 km horizontal resolution.

As radiosonde observations can also be regarded as point measurements, the same approach is used to assess the contribution of different measurement geometries to the radiosonde representativeness error. However, an additional error source is caused by the spatial and temporal displacement of radiosondes. Therefore, it is necessary to distinguish between radiosondes for which the actual position at every height level is available (87 %) and those reports that only provide the launch position and time (13 %).
For both cases, the temporal and the spatial part of the representativeness error, resulting from the collocation criteria, has to be considered. The error due to the spatial displacement is assessed by determining the differences between a point and a line measurement as the weighted mean over distances up to 120 km in east-west and north-south direction. Then, the weighted average over altitude is calculated accordingly to the model representativeness error. To account for the temporal displacement, a time offset value is estimated by assessing the representativeness error of the appropriate spatial displacement. The mean wind velocity over the validation period (16.19 m s^{-1}) and the temporal collocation criteria of 90 min results in a spatial displacement of 82 km, which corresponds to a representativeness error of 1.32 m s^{-1} for both channels with 90 km horizontal resolution and 1.46 m s^{-1} for the Mie winds with 10 km horizontal resolution. For the 13 % of the radiosonde data without the drift information, additionally, an error component due to the spatial displacement up to 50 km and an error component due to the temporal displacement during the radiosonde ascents of up to 90 min has to be considered. For the 87 % of the radiosondes with the drift information, a temporal offset value for the 15 min time interval into which the data are grouped must be taken into account. Those parts of the representativeness error are calculated accordingly to the parts resulting from the collocation criteria using the COSMO-DE analyses. To determine the overall contribution, the variances of the three different error components are summed up:

$$\sigma(\epsilon_{r\_RS}) = \sqrt{\sigma(\epsilon_r^{colloc.})^2 + 0.13 \cdot \sigma(\epsilon_r^{drift})^2 + 0.87 \cdot \sigma(\epsilon_r^{BUFR})^2}, \tag{4.3}$$

with:

$$\sigma(\epsilon_r^{colloc.}) = \sigma(\Delta x = 120\text{km}) + \sigma(\Delta t = 90\text{min} \approx 82\text{km}),$$
$$\sigma(\epsilon_r^{drift}) = \sigma(\Delta x = 50\text{km}) + \sigma(\Delta t = 90\text{min} \approx 82\text{km}),$$
$$\sigma(\epsilon_r^{BUFr}) = \sigma(\Delta t = 15\text{min} \approx 14\text{km})$$

As a last step, the effect of unresolved scales in the COSMO-DE analyses is assessed using the high-resolution ICON-LEM simulation. Fig. 4.3a displays the differences between a point and a line measurement averaged and weighted over distances up to 200 km as a function of altitude for the ICON-LEM and COSMO-DE data of the same date. The COSMO-DE model underestimates the representativeness error compared to the ICON-LEM simulation. On average, the offset value between the two models is 0.20 m s^{-1}. This offset value is added to the sum of the variances of the different error components, resulting in a representativeness error of 2.48 m s^{-1} for the Rayleigh winds, 2.49 m s^{-1} for the Mie winds with 90 km horizontal resolution and 2.66 m s^{-1} for the Mie winds with 10 km horizontal resolution. Fig. 4.3b additionally shows the representativeness error caused by the different measurement geometries as function of distance for specific altitude ranges. As expected, the representativeness error and the differences between COSMO-DE and ICON-LEM increase significantly with distance. It is largest around the tropopause, where wind gradients are typically strongest and smallest in the mid-troposphere. Fig. 4.3b underlines the importance of considering the representativeness errors in the Aeolus Cal/Val activities when comparing the HLOS winds with other spatially and temporally offset observations.

4.2.2 Model error and radiosonde wind observational error

The IFS and ICON model errors are derived from the ensemble data assimilation first guess error stored in the feedback files. It provides an appropriate measure for spatial and temporal variation of the background error. It should be noted that values taken for the IFS model errors are only valid at the start of the 4D-Var window as they increase during the 12-hr window. The model error estimates are determined for the latitudinal band between 23.5 and 65°N (Table 4.2) and globally (Table 4.3). NWP models, in general, tend to exhibit higher uncertainty in cloudy than in clear sky areas; thus, the model error is larger for Mie than for Rayleigh wind observations. For both observation channels, the ICON model error is on average more than 1 m s^{-1} larger than the IFS model error. Possible reasons for this could be differences in model properties, such as model resolution and typical uncertainties in NWP models, e.g., errors in the stratospheric circulations or in the distribution of clouds in the upper troposphere (Giorgetta et al., 2018, Laloyaux et al., 2020b). However, this issue is not within the scope of the thesis.

The radiosonde observational error σ_{RS} is assumed to be 0.7 m s^{-1}. The value is chosen based on the estimated measurement uncertainty of the GCOS Reference Upper-Air Network (GRUAN) for the wind speed, which was determined to be 0.4-1 m s^{-1} (Dirksen et al., 2014).

(a) ICON-LEM vs. COSMO altitude

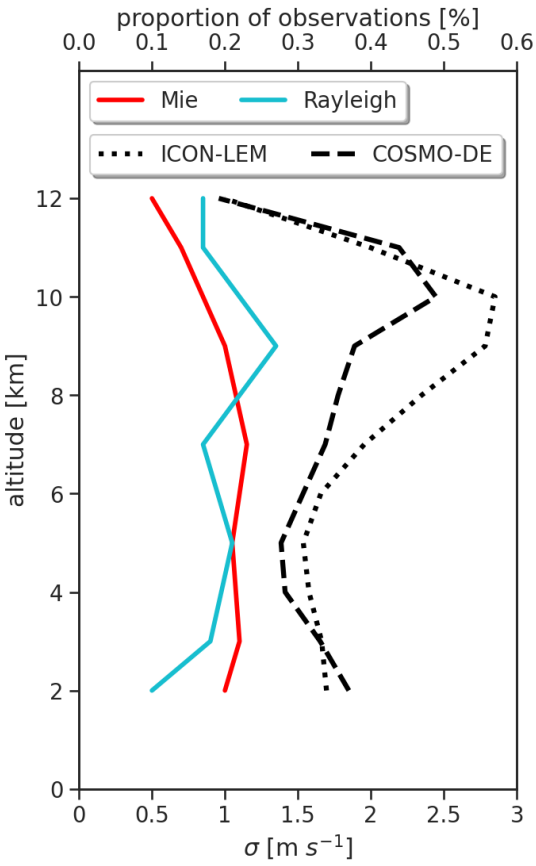

(b) ICON-LEM vs. COSMO distance

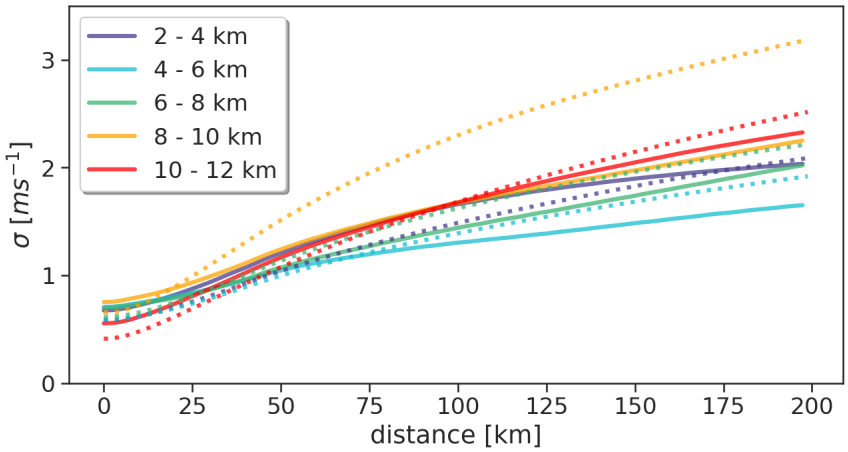

Figure 4.3: *(a) Representativeness error estimated with differences between a point and a 90 km line measurement (weighted mean over distances up to 200 km) as function of altitude for an ICON-LEM simulation (black dotted line) and COSMO-DE analyses (black dashed line), shown together with the proportion of observations of the Rayleigh (turquoise) and Mie (red) wind observations; (b) Representativeness error estimated with differences between a point and a 90 km line measurement as function of distances for an ICON-LEM simulation (dotted lines) and COSMO-DE analyses (dashed lines) for different height levels (different colors).*

4.2.3 Aeolus wind observational error

Finally, using the validation results from Sec 4.1 together with the estimated representativeness and model or observation error components, the Aeolus instrument error $\sigma(\epsilon_{o\_A})$ is determined. Table 4.2 shows the values of $\sigma(\epsilon_{o\_A})$ for the validation with radiosonde observations and model equivalents for the latitudinal band between 23.5 and 65°N for the Rayleigh and Mie channel, separated for the ascending and descending orbit phase. Table 4.3 additionally displays the results of the global model-only statistic.

	Rayleigh		Mie (90 km)		Mie (10 km)	
	ascending	descending	ascending	descending	ascending	descending
$\sigma(\epsilon_{r\_RS})$	2.48	2.48	2.49	2.49	2.66	2.66
$\sigma(\epsilon_{o\_RS})$	0.70	0.70	0.70	0.70	0.70	0.70
$\sigma(\epsilon_{val\_RS})$	5.20	5.05	3.61	3.62	4.33	4.38
$\boldsymbol{\sigma(\epsilon_{o\_A})}$	**4.52**	**4.34**	**2.52**	**2.55**	**3.34**	**3.41**
$\sigma(\epsilon_{r\_ECMWF})$	0.50	0.50	0.52	0.52	0.12	0.12
$\sigma(\epsilon_{b\_ECMWF})$	0.80	0.81	1.02	1.05	1.15	1.11
$\sigma(\epsilon_{val\_ECMWF})$	4.59	4.43	2.49	2.79	3.52	3.63
$\boldsymbol{\sigma(\epsilon_{o\_A})}$	**4.49**	**4.33**	**2.21**	**2.53**	**3.32**	**3.45**
$\sigma(\epsilon_{r\_DWD})$	0.50	0.50	0.52	0.52	0.12	0.12
$\sigma(\epsilon_{b\_DWD})$	2.40	2.96	2.37	2.41	2.65	2.56
$\sigma(\epsilon_{val\_DWD})$	4.82	4.64	2.98	3.21	3.72	3.98
$\boldsymbol{\sigma(\epsilon_{o\_A})}$	**4.15**	**3.54**	**1.73**	**2.06**	**2.46**	**3.05**

Table 4.2: *Overview of the estimated Aeolus wind observational errors $\sigma(\epsilon_{o\_A})$ and the single components of the calculation: representativeness errors ($\sigma(\epsilon_{r\_RS})$, $\sigma(\epsilon_{r\_ECMWF})$, $\sigma(\epsilon_{r\_DWD})$), radiosonde observational error ($\sigma(\epsilon_{o\_RS})$), ECMWF and DWD model errors ($\sigma(\epsilon_{b\_ECMWF})$, $\sigma(\epsilon_{b\_DWD})$) and random differences from the validation ($\sigma(\epsilon_{val\_RS})$, $\sigma(\epsilon_{val\_ECMWF})$, $\sigma(\epsilon_{val\_DWD})$) [m s^{-1}] for the Rayleigh and Mie winds for the ascending and descending orbital pass for the northern hemisphere ($23.5 - 65°N$), restricted to the radiosonde collocations.*

	Rayleigh		Mie (90 km)		Mie (10 km)	
	ascending	descending	ascending	descending	ascending	descending
$\sigma(\epsilon_{r\_ECMWF})$	0.50	0.50	0.52	0.52	0.12	0.12
$\sigma(\epsilon_{b\_ECMWF})$	0.91	0.91	1.20	1.18	1.30	1.28
$\sigma(\epsilon_{val\_ECMWF})$	4.51	4.41	2.20	2.24	3.23	3.24
$\boldsymbol{\sigma(\epsilon_{o\_A})}$	**4.39**	**4.29**	**1.77**	**1.83**	**2.95**	**2.97**
$\sigma(\epsilon_{r\_DWD})$	0.50	0.50	0.52	0.52	0.12	0.12
$\sigma(\epsilon_{b\_DWD})$	2.34	2.37	2.44	2.39	2.65	2.56
$\sigma(\epsilon_{val\_DWD})$	4.77	4.69	2.65	2.73	3.18	3.24
$\boldsymbol{\sigma(\epsilon_{o\_A})}$	**4.13**	**4.02**	**0.89**	**1.21**	**1.75**	**1.98**

Table 4.3: *Same as Table 4.2, but for the global model-only statistics*

Overall, the Aeolus wind observational error estimates are fairly close when comparing

the IFS and radiosonde validation results. However, due to the differences in the model error in the DWD and ECMWF assimilation system, the Aeolus wind observational error estimates based on the DWD model equivalents are about 0.5 m s^{-1} smaller. Furthermore, discrepancies between the three validation results might be caused by uncertainties in the estimation of the representativeness errors, which are based on averaged values of analyses only covering the area around Germany at certain time periods. When only considering the comparisons with IFS model equivalents and radiosonde observations, the Rayleigh wind observation error estimate is between 4.3 m and 4.5 m s^{-1}. The Mie wind observation error estimates are about 2.5 m s^{-1} for the observations with 90 km and about 3.4 m s^{-1} for the observations with 10 km horizontal resolution. For both channels, $\sigma(\epsilon_{o\_A})$ shows good agreement between the ascending and descending orbit phases. Overall, the Aeolus wind observational error of the Mie observations ascending orbit is slightly larger than that of the descending orbit phase, and vice versa for the Rayleigh observations. Comparing the globally derived Aeolus wind observational errors with the results of the validation statistics of the Northern Hemisphere, smaller values occur for both the Rayleigh and the Mie wind observational errors. It must be taken into account that the representativeness errors considered for the global statistics are the same as for the validation of the Northern Hemisphere, thus based on an area covering only Germany and its neighborhood.

Fig. 4.4 displays the height dependency of $\sigma(\epsilon_{o\_A})$ for Rayleigh and Mie wind observations. The large differences between the validation results using the ICON model and the validation results using radiosonde observations or the IFS model are mainly concentrated on pressure levels above 500 hPa. There, the Aeolus wind observational error estimates based on the ICON model decrease towards the tropopause, whereas the other two estimates increase. Around and above the tropopause, the three independent $\sigma(\epsilon_{o\_A})$ estimates of the Rayleigh wind observations show a similar behavior again. The discrepancies in the Mie wind observational error estimate are overall larger, which underlines the assumption that uncertainties in the representation of clouds in the NWP models cause them.
Altogether, Fig. 4.4 shows that for using the Aeolus observations in data assimilation, the observational error assigned in the assimilation system should increase towards the upper troposphere and lower stratosphere for both Rayleigh and Mie. Aeolus observations there should be weighted less because of the overall larger Aeolus observational error but also because of the discrepancies due to model and representativeness errors.

4.2.4 Comparison and classification of the validation error estimates

The results for the radiosonde and the model-based validation around the small selected regions around radiosonde collocation points are found to be slightly larger compared to the Aeolus observational error estimates of Witschas et al. (2020) and Iwai et al. (2021). Witschas et al. (2020) compared the Aeolus wind observations with a 2-μm DWL during the validation campaigns WindVal III and AVATAR-E (Aeolus Validation Through Airborne Lidars in Europe) over Europe in late autumn 2018 and early summer 2019. By excluding the 2-μm DWL observation error, an Aeolus observational error of 3.9-4.3 m s^{-1} (2.0 m s^{-1}) for the Rayleigh (Mie) wind observations was determined (Witschas et al., 2020). Iwai et al. (2021) compared the Aeolus wind observations with GPS radiosondes over Japan during baseline 2B02 and 2B10 periods. By taking the radiosonde representativeness error from

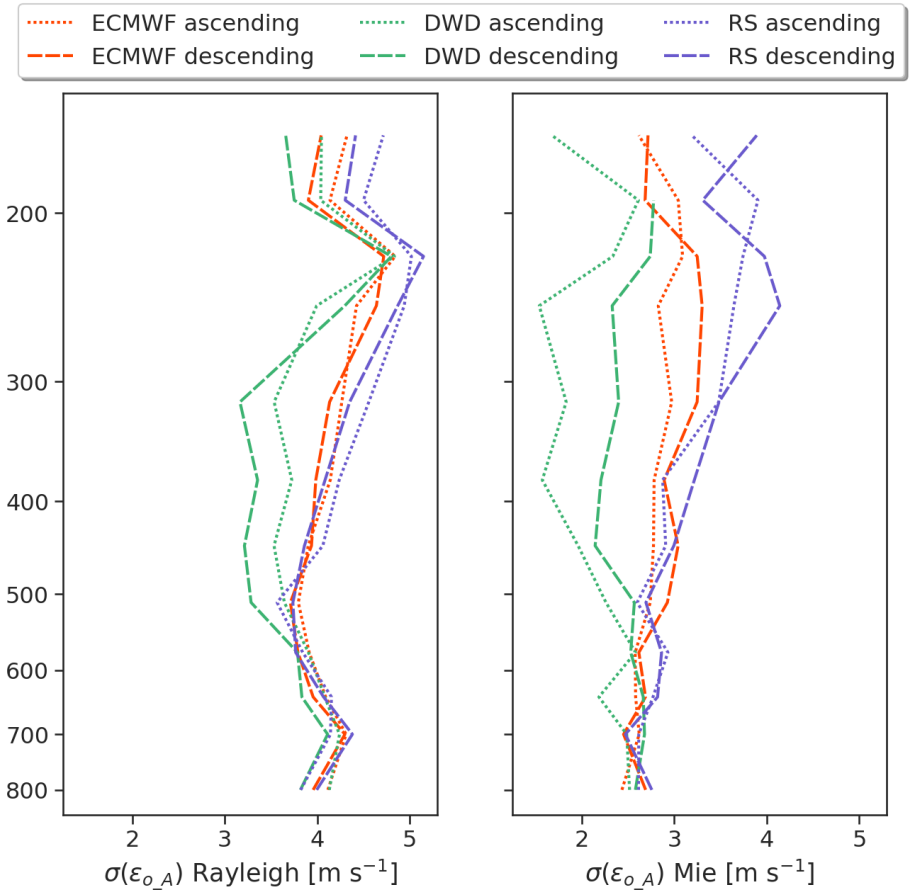

Figure 4.4: *The Aeolus wind observational error $\sigma(\epsilon_{o\_A})$ as function of altitude [hPa] for the Rayleigh and Mie observations, separately for ascending and descending orbit phase, estimated for the Northern Hemisphere ($23.5 - 65°N$), using collocated radiosonde observations (purple) and model equivalent statistics (O-B) around the collocation points of the ECMWF IFS model (orange) and the ICON model of DWD (green).*

this study into account, they estimated the Aeolus observational error to be 3 -4 m s^{-1} (2-3 m s^{-1}) for the Rayleigh (Mie) wind observations. The differences can be caused by a variety of factors, including different lengths of validation periods and, therefore, different sample sizes. Furthermore, Iwai et al. (2021) used the representativeness error estimate based on the COSMO-DE model area for their study over Japan which may bias the results. Other validation studies covering the period considered here have not considered representativeness or observational error components. Lux et al. (2020) found a random error estimate of 5.9 m s^{-1} for the Rayleigh wind observations during the WindVal III for comparisons with the A2D; Baars et al. (2020) used radiosonde during the Polarstern research vessel cruise from Bremerhaven to Cape town in November/December 2018 to determine the random error of the Rayleigh (Mie)wind observation being 4.8 m s^{-1} (1.6 m s^{-1}); and Bedka et al. (2021) analyzed research flights over the Eastern Pacific Ocean in April 2019 with a heterodyne detection DWL and a water vapor lidar onboard which revealed a random error estimate of 5.1 m s^{-1} (4.7 m s^{-1}) for the Rayleigh (Mie) wind observations. These results are in the range of the random differences displayed in Sec. 4.1, suggesting that uncertainties in the determination of the contributing error components primarily cause differences in estimations of the Aeolus observational error. Rennie and

Isaksen (2020) estimated the Aeolus observational error using the ECMWF model on a global base by subtracting a background u wind error of 1.6 m s^{-1}, resulting in a $\sigma(\epsilon_{o\_A})$ of 4-5 m s^{-1} (3 m s^{-1}) for the Rayleigh (Mie). The global statistics in this study are based on a region-constrained and short-period approach, particularly to avoid the random error estimates being affected by horizontal and temporal variations in bias. This probably results in the slightly smaller values of the globally derived Aeolus wind observational error. However, given that the representativeness and the model error estimates exhibit several uncertainties and the subtracted bias varies a lot, the discrepancies are within the range of the uncertainty of the estimates.

4.3 Rayleigh wind observation bias dependencies and correction approaches

According to ESA (2016), the accuracy of the Aeolus HLOS wind observations on a global scale is required to be 0.7 m s^{-1} to ensure a positive impact in NWP. However, the systematic differences found in Sec. 4.1 are much larger and fluctuate strongly with time. In particular, the estimates of Rayleigh wind observations show discrepancies between orbital phases in addition to temporal variations. To better understand Rayleigh bias and find a suitable bias correction scheme for data assimilation application, bias dependencies for different time periods are investigated on a global scale.

4.3.1 Rayleigh wind bias dependence on latitude and orbit phase

Fig. 4.5 displays the Rayleigh wind bias as a function of latitude, separately for the ascending and descending orbit phases. The values are binned into 10° latitude bins. Results are shown for March and August 2019. The bias estimates based on the two different NWP models correspond well along the climate zones. Larger discrepancies only appear in the tropics and subtropics. The comparison of Aeolus winds with inhomogeneously distributed radiosonde observations overall shows good agreement as well. Outliers, as around 20° S or 85° N, are mainly related to small sample sizes.
Representative for the winter and spring, Fig. 4.5a is chosen to show that the bias is fairly constant with latitude in these seasons. Small differences between the orbital phases occur in the Southern Hemisphere and the subtropical region of the Northern Hemisphere. From 40° N up to the north pole, almost no deviation between ascending and descending orbit is visible. End of summer, in August 2019 (Fig. 4.5b), the bias varies with latitude with an amplitude of 4-5 m s^{-1}. As seen in Sec. 4.1 for the summer and autumn seasons, large differences between the orbit phases exist, particularly outside of the tropics. Between the subtropical region and the poles, the bias for the descending orbit is positive, whereas the bias for the ascending orbit has a negative sign.
The results indicate that besides the satellite's orbit phase and the season, the latitudinal position of the satellite seems to influence the Aeolus Rayleigh wind bias. Before the launch of Aeolus, thermal fluctuations affecting the DWL instrument were considered as one of the possible sources of bias. Fluctuations in long-wave and solar radiation can cause small changes in the direction of the received laser light from the atmosphere, to which the spectrometers are sensitive, causing apparent frequency shifts and hence a wind bias.

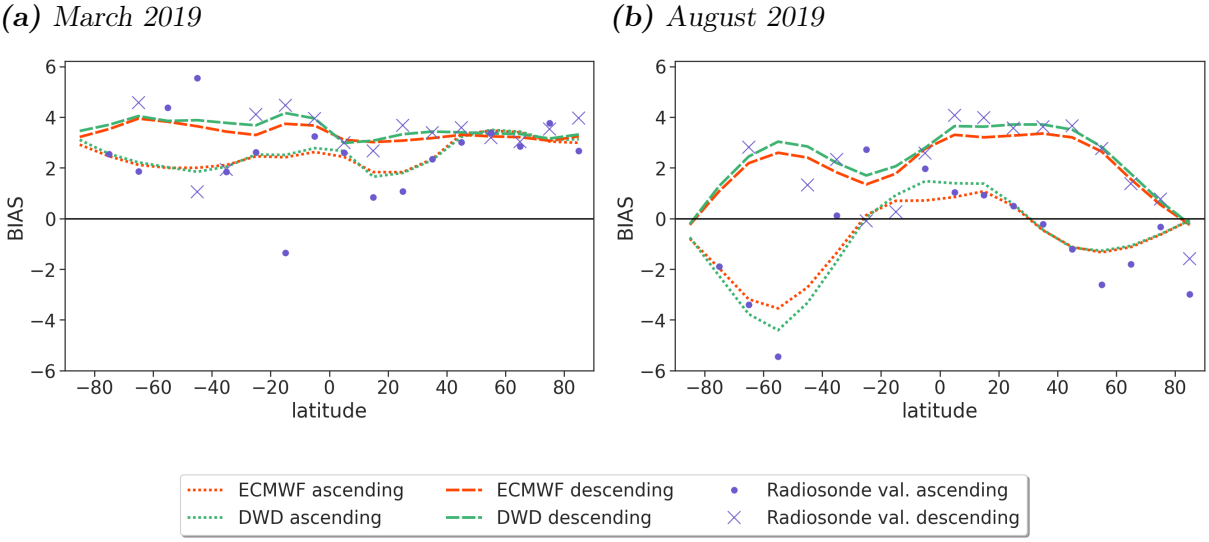

Figure 4.5: *Rayleigh HLOS wind bias as a function of latitude for ascending (dotted line) and descending (dashed line) orbit phase, calculated with model equivalents of the ECMWF IFS (orange) and the DWD ICON model (green). In purple (point markers: ascending, cross markers: descending), comparison results with collocated radiosonde observation are shown. Values are binned into latitude bins of* 10°*. (a): March 2019; (b): August 2019.*

The detected bias dependencies can potentially be related to changes in the top of the atmosphere temperature. The latitude variations and orbit differences are largest during the Northern Hemispheric summer, which is the season with the largest latitude gradient in the asymmetric radiative response. During the Southern Hemispheric summer, the gradient is less strong, and the bias dependencies and orbit phase differences are less pronounced.

A simple bias correction approach as a function of latitude, separately for ascending and descending orbit phases, is applied to eliminate systematic differences for the validation period. For latitude bins of 10°, the O-B departures from the previous seven days are averaged using the following weights (with i=0 being the current day):

$$w_{\mathrm{i}} = \frac{\frac{1}{1+\mathrm{i}}}{\sum_{j=1}^{7}(\frac{1}{1+\mathrm{j}})}, i = 1, ..., 7. \tag{4.4}$$

The resulting correction values are subtracted from the O-B departure of the day under consideration, and the residuals are averaged for each month of the validation period (Fig. 4.6). Considering the effect of the orbit phase differences, this is done separately for the ascending and descending satellite pass. To estimate if the model bias matters, three different configurations are tested, which differ regarding the correction values: the bias correction values are based on the same model; the bias correction value is calculated with the other NWP model; the bias correction value is an average value of the two NWP models. After applying the bias correction, a temporal variation, as seen in Sec. 4.1 for the systematic differences, is still apparent in the residuals. As the bias correction approach is essentially temporal and spatial smoothing, it is suggested that fast changes in the systematic errors are one source of the bias. At the beginning of the Aeolus mission, the correction is quite

efficient. In spring 2019, when the latitude dependence is comparably weak and the bias comparably high, a residual up to over 1 m s^{-1} remains. After the processor update in May 2019, when the Rayleigh ascending wind bias tends to be negative, also the residual bias exhibits a negative sign. Differences between the two models regarding the sign of the remaining bias are visible in September 2018 for the ascending orbit and in December 2019.

(a) *Rayleigh ascending*

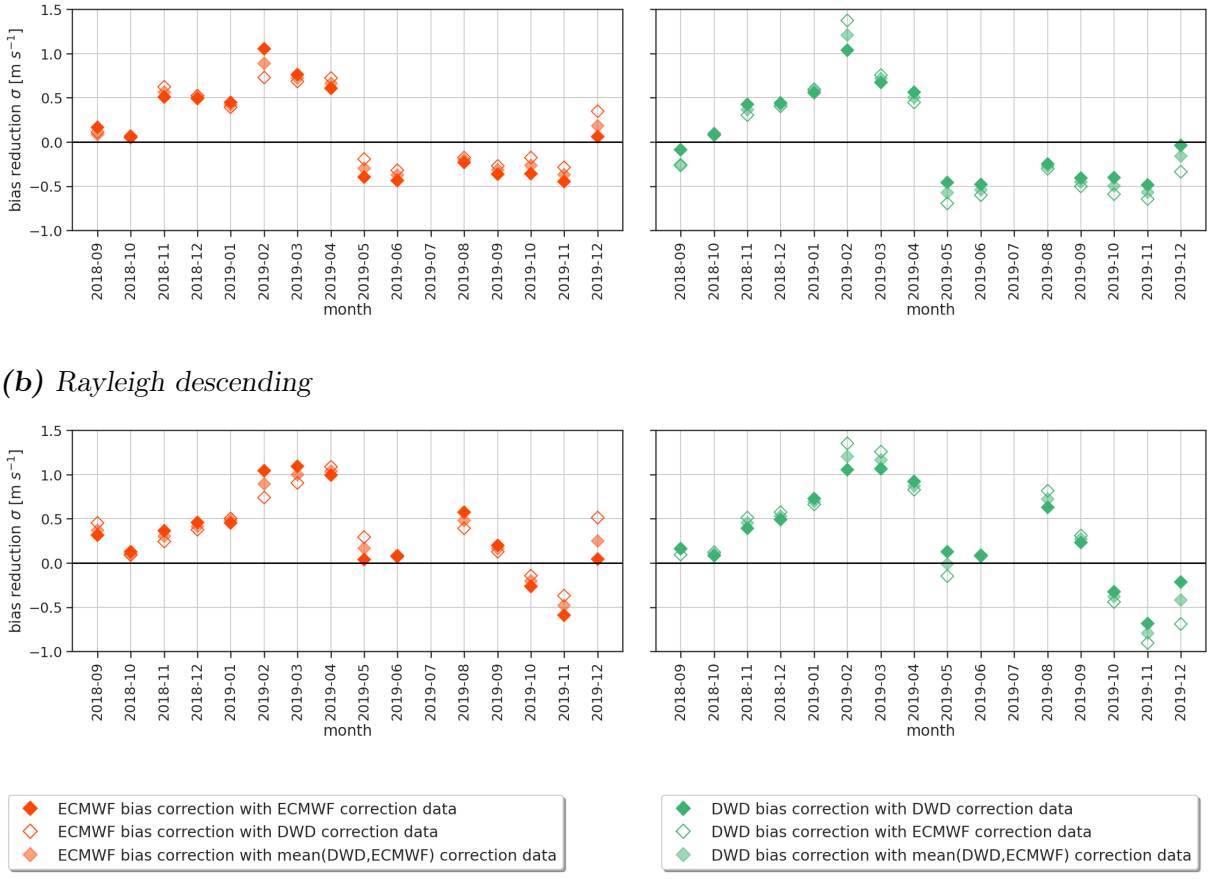

(b) *Rayleigh descending*

Figure 4.6: *Residual after a latitude-dependent bias correction, separately for Rayleigh ascending (a) and descending (b) orbit phase averaged over one month. On the left (orange), the ECMWF IFS model residuals, and on the right side, the DWD ICON model residuals (green) are displayed. The correction values are either based on the previous week of the model equivalents of the own model (dark-filled markers) or the other NWP model (unfilled marker) or an average value of both models (light-filled markers).*

Although remaining systematic differences - in particular in phases with large temporal bias changes - are still apparent, the correction can clearly decrease the bias. In total, the bias is reduced by almost 1 m s^{-1} for the ICON model and even more than 1 m s^{-1} for the IFS model (Table 4.4). A correction based on the previous seven days of the own model yields a comparable mean absolute residual bias for the IFS and the ICON model. Correcting the IFS model with the correction values calculated with the ICON model results in the lowest overall remaining bias and the largest reduction. In contrast, the ICON model O-B statistic shows worse results when applying the IFS model information to correct the latitude-dependent error. Altogether, no significant differences between the individual methods were found (following a Student's t-distribution), again indicating that model

biases do not have a dominant effect on the bias assessment. On average, the absolute remaining bias of the Rayleigh wind observations is about 0.37-0.59 m s^{-1}.

	ascending		descending	
	IFS	ICON	IFS	ICON
without bias correction	1.41	1.28	1.64	1.54
correction value based on IFS model	0.43	0.53	0.44	0.59
correction value based on ICON model	0.37	0.43	0.42	0.48
correction value based on $\overline{\text{(IFS,ICON)}}$	0.39	0.48	0.43	0.52

Table 4.4: *Mean absolute residual bias [m s^{-1}] of the ECMWF IFS and the DWD ICON model after a latitude-dependent bias correction for three different configurations for the period from September 2018 to January 2020.*

Assume that variations in long-wave and solar radiation and the associated response of the telescope's thermal control system are related to bias. In that case, it is supposed that, additionally, variations of the bias with longitude are present. Therefore, in the following Sec. 4.3.2, also the longitude-dependent Rayleigh bias component is examined, and it is tested whether a two-dimensional (latitude-longitude) bias correction approach can further reduce the remaining bias.

4.3.2 Rayleigh wind bias dependence on latitude, longitude and orbit phase

Fig. 4.7 shows latitude-longitude plots of the Aeolus Rayleigh HLOS wind bias for May and October 2019. Since the two NWP models agree very well in assessing the Rayleigh wind bias, only the results using the ECMWF IFS model are shown. In May, when the orbit phase and latitude dependencies are less pronounced, small fluctuations with longitude are visible in the tropical and subtropical regions of the Northern Hemisphere. For the ascending orbit phase, these patches of larger bias values appear to be related to land-sea distribution. This connection is also visible in October 2019 for the ascending orbit phase. Furthermore, it seems that the bands of pronounced bias values in the tropics match with the Intertropical Convergence Zone (ITCZ), which moves further north from the equator during the northern summer and further south towards the southern summer. The large bias of the descending orbit in May on the Southern Hemisphere in the midlatitudes might be related to the subtropical jet. The three gaps around 60°S are due to a technical issue at ECMWF. In October, the bias overall changed from positive to negative except for the descending orbit in the tropics and subtropics of the Southern Hemisphere.
Altogether, the results show that the bias dependencies are very scene dependent. There are indications that the source of bias is related to radiative variations, including land-sea distribution, seasonal variations and asymmetries in radiative response along latitude. However, no solid connection can be identified.

To examine the magnitude of the influence of the longitude component on the bias correction approach described above, it is repeated considering both geographic dimensions. Therefore, the Aeolus HLOS O-B statistics of the previous seven days as a function of latitude and longitude are averaged and weighted using bin sizes of 10°. Fig. 4.8 shows the

(a) Rayleigh ascending May 2019

(b) Rayleigh descending May 2019

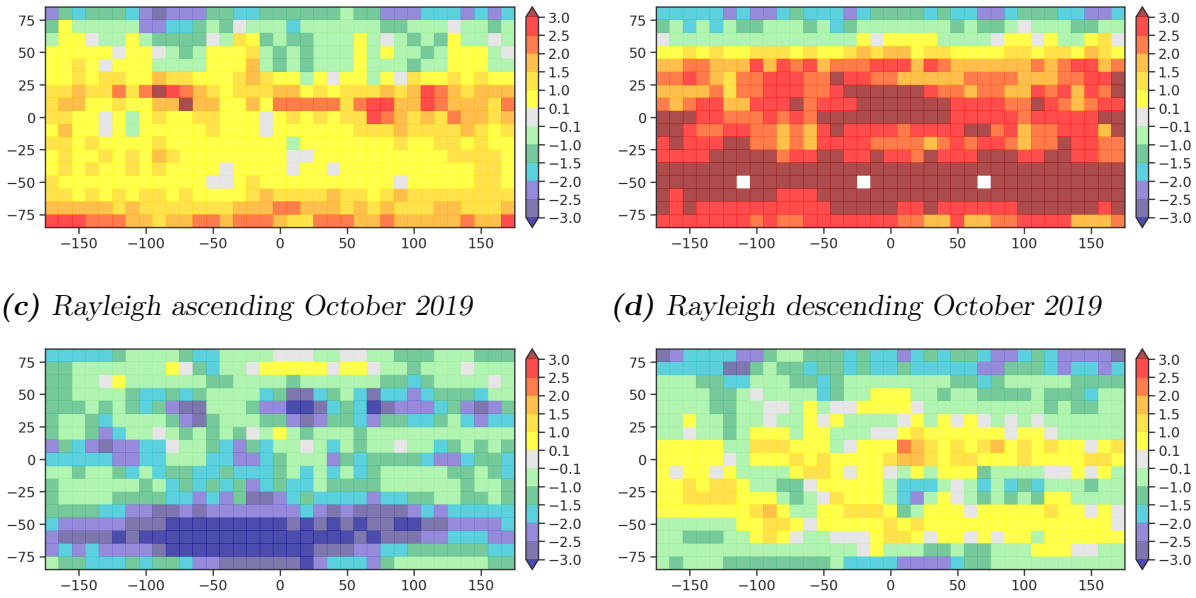

(c) Rayleigh ascending October 2019

(d) Rayleigh descending October 2019

Figure 4.7: *Rayleigh HLOS wind bias as a function of latitude and longitude for ascending and descending orbit phase, calculated with model equivalents of the ECMWF IFS for May 2019 (a,b) and October 2019 (c,d). Values are binned into latitude and longitude bins of* 10°.

(a) Rayleigh ascending

(b) Rayleigh descending

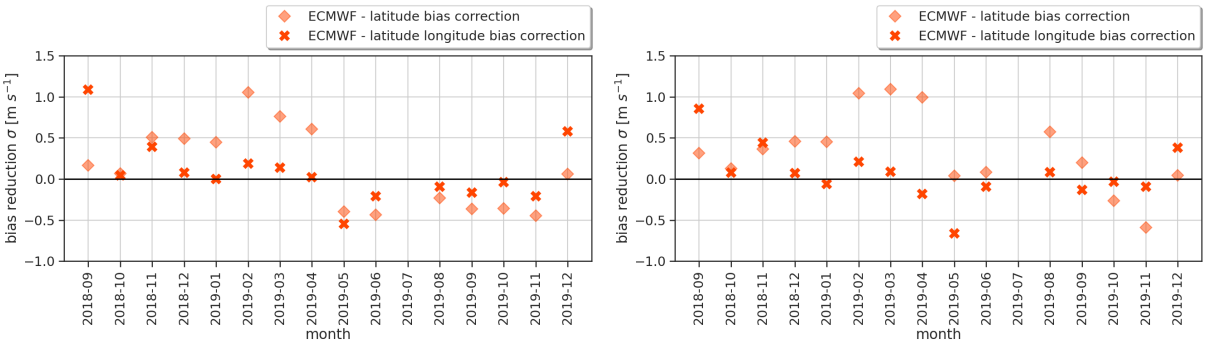

Figure 4.8: *Residual after a latitude-dependent bias correction (diamond marker) and a two-dimensional latitude-longitude-dependent bias correction (cross marker) averaged over one month, using the ECMWF IFS model equivalents. (a) for the Rayleigh ascending, and (b) for descending orbit phase.*

resulting residual bias based on the ECMWF IFS model averaged over each month. To get an impression of how strong the longitudinal bias variation is, the results are compared to the one-dimensional latitude-dependent correction approach from Sec. 4.3.1.
The mean absolute remaining bias for both correction formulations is provided in Table 4.5. Overall, the residual has been decreased by almost 50 % when considering the longitude dependence for ascending and descending satellite orbit phase. Main improvements occur for the bias correction in late winter and early spring, where a one-dimensional correction approach is not that effective. However, right after the mission's start, in May 2019 and at the end of the year, the remaining bias is increased when considering the longitudinal dimension. The one-dimensional latitude-dependent correction approach has almost removed the bias in these months.

type of bias correction	ascending	descending
latitude	0.43	0.44
latitude - longitude	0.25	0.23

Table 4.5: *Mean absolute residual bias [m s^{-1}] after a latitude and a latitude-longitude bias correction approach using the ECMWF IFS model for the time period from September 2018 to January 2020.*

4.4 Concluding remarks on the validation of Aeolus HLOS wind observations

Validation statistics of the Aeolus HLOS wind observations for the initial phase of the mission have been performed based on comparisons with radiosonde observations and model equivalents from DWD's ICON model and ECMWF's IFS system. This allowed systematic and random differences to be characterized on a regional (Northern Hemisphere mid-latitudes) and global basis.

The mean absolute systematic difference has been found to be about 1.8 m s^{-1} for the Rayleigh winds and 1.6 m s^{-1} for the Mie wind observations. The mean random difference is 3-5 m s^{-1} for the Rayleigh channel and 3-4 m s^{-1} for the Mie channel. The discrepancies found between the radiosonde and model-based random error validation results are mainly due to differences in spatial and temporal representativeness. Both the systematic and random errors are higher than expected before the launch. Mie wind errors are smaller overall compared to Rayleigh wind errors but show larger differences between the three validation statistics due to uncertainties when clouds are present. By estimating the representativeness errors, the observational error of Aeolus could be evaluated. The estimated representativeness error for comparison with radiosonde observations is about 2.5 m s^{-1}, which emphasizes the importance of considering the sources of representativeness error when comparing HLOS winds with other spatially and temporally offset observations. The resulting observational Aeolus wind error overall increases in the upper troposphere and lower stratosphere, with the largest discrepancies between the validation reference datasets occurring around the tropopause. Therefore, it is suggested that less weight be given to the Aeolus observations in the assimilation there.

Further investigation of the systematic differences of the Rayleigh channel revealed several dependencies. The Aeolus wind bias varies with season, orbital phase, latitude, and longitude. These detected bias dependencies are expected to be related to long-wave and solar radiation fluctuations and the radiative response. It has been shown that a simple bias correction approach as a function of latitude, separately for the ascending and descending satellite orbit phase based on the last seven days, can reduce the bias. Including both geographic dimensions in the bias correction further reduces the residual by nearly 50%.

In (Rennie et al., 2021), a bias correction similar to the here presented scheme has been used manually via look-up tables of the mean(O-B) from the previous week versus argument of latitude (orbit phase angle) and longitude. The bias correction has been applied for both Rayleigh and Mie wind observations. However, the Mie biases are smaller and more stable and thus not changed much by the correction scheme. In 2020, it became clear that there is a link between the Rayleigh bias and the ALADIN telescope primary (M1) mirror temperatures. The M1 mirror's onboard thermal control mechanism varies in response to the top of atmosphere radiation. Therefore, a bias correction has been developed at ECMWF, as part of the Aeolus Data Innovation and Science Cluster (DISC), using a multiple linear regression method of ECMWF O-B statistics and the thermistors of the telescope M1 mirror (Rennie et al., 2021, Weiler et al., 2021). This successfully eliminated most part of the bias. On 20 April 2020, the M1 temperature bias correction was operationally implemented in the L2B processor. However, some small residual biases still exist after the implementation, so several NWP centers have implemented additional model-based bias corrections. At DWD, a latitude-dependent correction scheme (according to Sec. 4.3.1) for specific height levels is used to further improve the impact of the Aeolus observation in the assimilation system of the ICON model (Sec. 3.2). Furthermore, the assigned observation error is chosen accordingly to the estimated Aeolus wind observational error in Sec. 4.2.3. A detailed examination of the Aeolus impact at DWD is provided in the following main results part of this thesis (Chapter 5).

Chapter 5

Results: Impact of Aeolus HLOS wind assimilation in the global model ICON

To assess the impact of Aeolus HLOS wind observations in the operational global assimilation and forecasting system of DWD, an OSE for three months has been performed using the global model ICON based on the general operational settings (Sec. 3.2). This chapter consists of two main parts: First, a global overview of the systematic changes in the analysis and impact on forecast errors is provided (Sec. 5.1). The second part focuses on regions and time periods with a particularly strong influence of the Aeolus wind observations and discusses indications of dynamical changes and processes related to the positive impact (Sec. 5.1).

5.1 A global statistical overview

5.1.1 Systematic changes in the analysis

Fig. 5.1 shows the systematic changes in the analysis of the zonal wind component due to the Aeolus observations (EXP_A - CTRL) for 100, 250, and 600 hPa. Positive values indicate that Aeolus observations tend to make the zonal wind component more westerly; negative values indicate a strengthening of the easterly flow. Additionally, the absolute mean analysis differences between the CTRL run of the OSE and ERA5 are shown, providing a qualitative estimate of the structure of systematic analysis errors.

Altogether, the most pronounced systematic influence of the Aeolus observations occurs around key atmospheric circulation systems, strong large-scale wind regimes, and convectively active areas in the tropics, where uncertainties in the analysis are systematically larger, and the background forecast does not represent the associated atmospheric phenomena well. Furthermore, it is apparent that increased influence is related to a low number of other collocated observing networks, e.g., oceanic regions.

In the mid-troposphere, the trend of making the zonal wind more westward is strongest around the Indian Ocean and slightly less above the West Pacific and the East Pacific Ocean south of the equator. West winds are accelerated in the equatorial East Pacific. The strengthening of easterlies around the west coast of Africa is probably related to the mid-level African Easterly Jet (AEJ), which was found to be strongly influenced by the Aeolus HLOS winds, especially the northern part (Borne et al., 2022). Uncertainties in

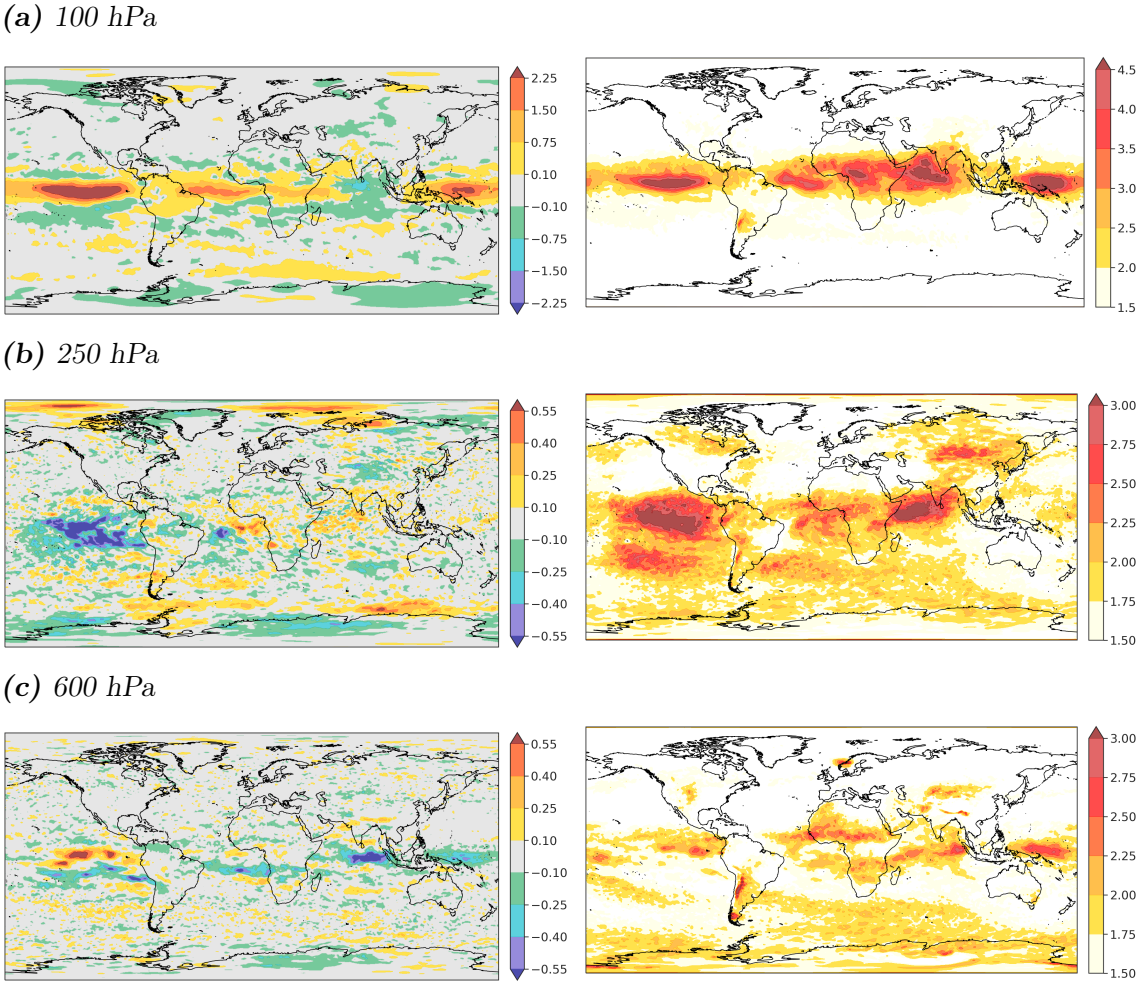

Figure 5.1: *Mean analysis difference (EXP_A - CTRL) of the zonal wind component U (left column) and absolute mean difference of the zonal wind component between the CTRL analysis and the ERA5 reanalysis (right column) at (a,b) 100 hPa, (c,d) 250 hPa and (e,f) 600 hPa for 01 July 2020 to 30 September 2020. Note different color scales for 100 hPa compared to 250 and 600 hPa.*

the Indian Ocean are likely to be associated with the synoptic-scale monsoon circulation system in the lower troposphere, which typically lasts from June to September.

At 250 hPa, the Aeolus observations largely influence the zonal wind field in the East Pacific, where also systematic analysis errors are increased. Changes in the analysis due to the assimilation of HLOS winds occur as strengthening of easterlies. These changes in the upper level are presumably related to modifications in the zonal Walker circulation, which in turn is connected to the state of ENSO. The state of ENSO switched during the OSE period, suggesting that associated changes in the convective pattern at the coast of South America and Indonesia are the dynamical source of the strong influence. Furthermore, enhanced influence of Aeolus observations in the upper troposphere is found in the Mid-Atlantic Ocean and the polar regions, but with fluctuations in the sign of the mean differences.

At the level of the tropical tropopause, the mean zonal wind analysis is particularly modified around the equator (note that the color scale is different from the lower levels). There, the strengthening of westerlies dominates. Only at the edge of the tropics and

above the Indian Ocean are easterly winds accelerated when including the Aeolus observations. The analysis changes in the surrounding of the Indian Ocean probably represent an amplification of the upper-level Tropical Easterly Jet (TEJ) that develops in the upper atmosphere during the Asian monsoon. Compared to the ERA5 reanalysis, the TEJ region is characterized by large systematic analysis errors. Besides the tropics, an influence of the Aeolus observations is again visible in the Southern Hemisphere's polar region.

Since the pattern of changes in the mean zonal wind analysis due to Aeolus is quite constant with time in the troposphere, it has been concentrated on the mean over the whole OSE period. The picture looks different at the stratospheric levels. Fig. 5.2 shows the same as the left column of Fig. 5.1, but separately for (a) July to mid of August and (c) mid of August to September at 50 hPa. Between 70 and 10 hPa, typically, the quasi-biennial oscillation (QBO) of the equatorial zonal wind between easterlies and westerlies takes place by downward propagation of the successive wind regime with a period of 22 to 34 months. In winter 2019/2020, the QBO phase change from westerly to easterly winds was disrupted, and an eastward zonal-mean jet subsequently emerged above the shallow westward layer (Anstey et al., 2021). In 2020 the normal QBO cycling manifested again as a westerly jet. The OSE period covers the alternation between 50 and 30 hPa, where the QBO westerly phase evolved mid of August. In the time before the emergence of the westerly jet at 50 hPa (Fig. 5.2a), the Aeolus observations tend to accelerate the easterlies around the equator. However, the magnitude of the influence is much weaker than in the second half of the OSE period, during the QBO westerly phase (Fig. 5.2b). Those equatorial west winds are strengthened to a large extent by the Aeolus observation. The ability of Aeolus to measure this reversal is investigated in more detail in Sec. 5.2.1.

(a) *50 hPa: 01 Jul 2020 - 15 Aug 2020* ***(b)*** *50 hPa: 15 Aug 2020 - 30 Sep 2020*

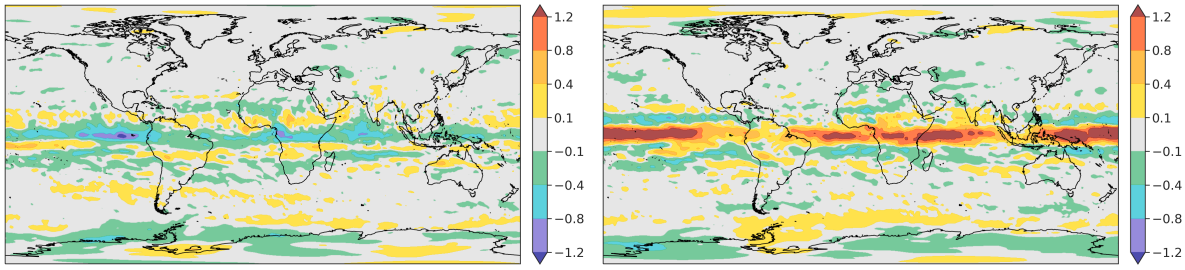

Figure 5.2: *Mean analysis difference (EXP_A - CTRL) of the zonal wind component U at 50 hPa for (a) 01 July 2020 to 15 August 2020 and (b) 15 August 2020 to 30 September 2020.*

5.1.2 Short-range forecast impact: Observation-based verification

The impact of the Aeolus HLOS winds on the quality of short-range forecasts up to 36 h is verified by the fit to observations from radiosondes (TEMP), aircraft (AIREP), GPSROs, and AMVs. The relative mean differences in RMSE between EXP_A and the CTRL run as functions of altitude are shown in Fig. 5.3, separately for the tropics, the Northern and the Southern Hemisphere. The size of each compared sample is presented by the grey line in the subplots alongside. Additionally, the average values of the changes in forecast error are

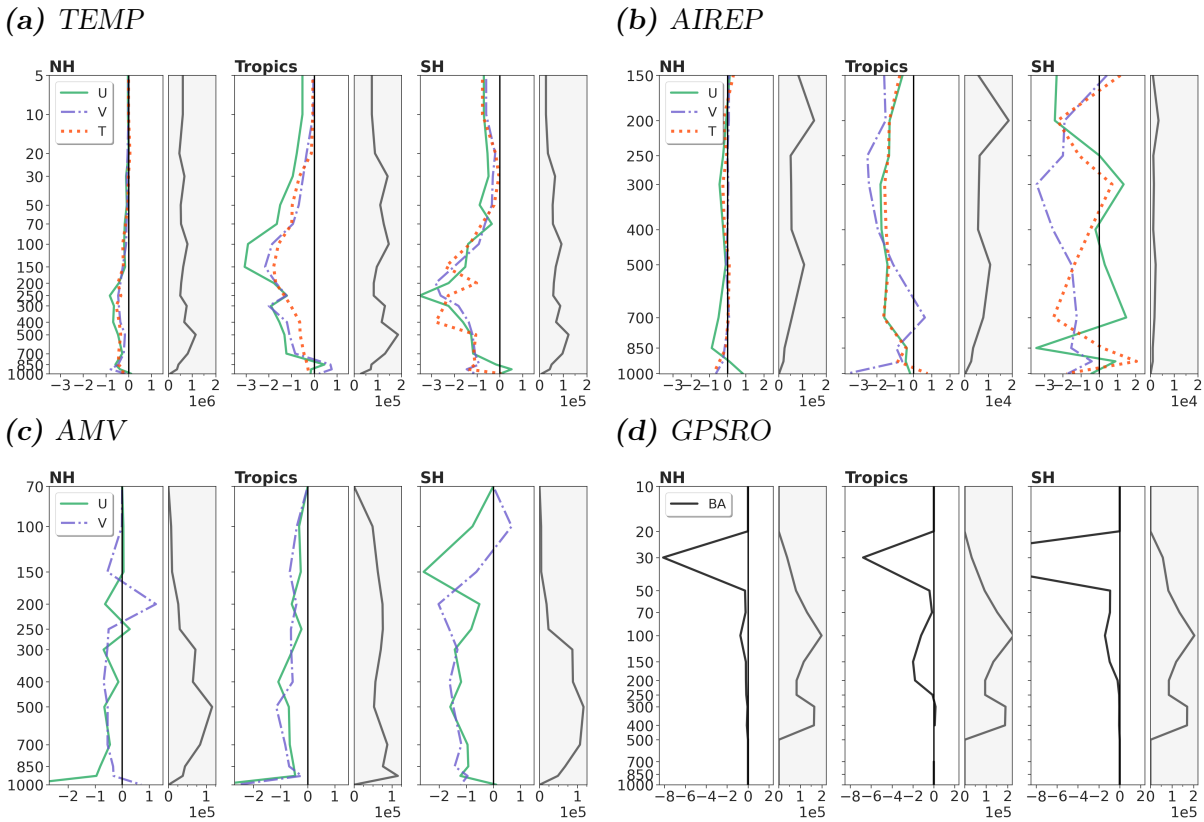

Figure 5.3: *The relative mean differences in 3-36 h forecast RMSE [%] between the EXP_A and the CTRL run as functions of altitude for 01 July 2020 to 30 September 2020, verified against (a) radiosonde (TEMP) and (b) aircraft (AIREP) for the zonal (U) and meridional (V) wind component and the temperature (T), against (c) AMV for U and V and against (d) GPRSO observations for the bending angle (BA), separately for the tropics, the northern (NH) and southern (SH) hemisphere. The gray lines in the subplots alongside present the number of observations.*

	Variable	**NH**	**Tropics**	**SH**
TEMP	U	−0.30	−1.20	−1.05
	V	−0.25	−0.70	−1.21
	T	−0.25	−0.69	−1.12
AIREP	U	−0.14	−1.07	−0.48
	V	−0.08	−1.57	−1.59
	T	−0.15	−0.99	−0.54
AMV	U	−0.46	−0.51	−0.70
	V	−0.12	−0.51	−0.75
GPSRO	BA	−0.59	−0.77	−1.36

Table 5.1: *Averaged values of differences in 3 - 36 h forecast RMSE [%] between the EXP_A and the CTRL run as functions of altitude for 01 July 2020 to 30 September 2020 from Fig. 5.3.*

listed in Table 5.1. Beneficial impact (represented by negative values) for radiosonde wind and temperature observations is largest in the tropics and the Southern Hemisphere, with a maximum around the tropopause (up to 3.5% improvement). The Northern Hemisphere, where the number of radiosonde observations is highest, shows a smaller impact, but on average, up to 0.3% improvement is found that also peaks at heights of the extratropical tropopause. The fit to wind and temperature observations from aircraft, which are most frequent at flight levels, are also mainly improved in the tropics (up to 1.6%) and to a lower extent in the Northern Hemisphere (up to 0.2%). The impact evaluation with respect to aircraft observations in the Southern Hemisphere suffers from a low number of measurements. Thus, these results should be treated with caution. AMVs and GPSRO observations, in contrast, are quite abundant in the Southern Hemisphere. On average, the impact is 0.7% relative to AMV winds and 1.4% relative to bending angles from GPSRO measurements. The largest improvements for AMVs are found in the lower and mid-troposphere, where the number of compared observations is highest. Around 400-500 hPa, the maximum impact in the tropics is 1.2%. In the Northern Hemisphere, improvements of ∼1% occur. GPSRO impact is strongest in the mid- and lower stratosphere. At 30 hPa, the maximum reaches eight or even more percent. At lower levels, where the sample of compared observations is larger, the impact reaches up to 3% in the tropics. In general, the changes in the short-range forecast errors resulting from assimilating Aeolus HLOS winds consistently show positive impact verified with radiosonde, aircraft, AMV, and GPSRO observations.The largest improvements are mainly found in upper atmospheric levels in the tropics and the Southern Hemisphere, also depending on the number of measurements. Despite the good coverage of observations on the Northern Hemisphere, Aeolus HLOS winds nevertheless still have a comparably large impact on the short-range forecast there.

5.1.3 Medium-range forecast impact: Analysis-based verification

To evaluate the impact of the Aeolus HLOS winds on forecasts with lead times of 24-120 h, these forecasts are verified against the ERA5 reanalysis. An overview of the forecast error reduction in terms of relative differences in RMSE between EXP_A and the CTRL run for the tropics, the midlatitudes, and the polar region of both hemispheres as a function of altitude is provided in Fig. 5.4. The relative reduction of forecast error is shown for the zonal wind component (U), geopotential (Z), temperature (T), and relative humidity (RH). The verification with analyses can involve larger uncertainties for short lead times as forecast errors strongly correlate with the analysis error, especially in data-sparse areas (Geer et al., 2010). Therefore, results for 24 h should be treated with caution.

As expected and similar to the observation-based verification (Fig. 5.3), Aeolus wind observations lead to the largest error reduction in the tropics, where winds are not constrained by geostrophic balance. This is evident for all four variables and for all forecast lead times. For the zonal wind component, the forecast quality in the tropics is improved by at least 2% and up to 8%, peaking at the tropopause height of around 100 hPa. For temperature, the largest improvements in the tropics are in the upper troposphere, for relative humidity between 500 and 850 hPa. Besides the tropics, the forecast is, on average, also improved in polar regions and the midlatitudes of both hemispheres. In the Southern Hemisphere, the beneficial impact of Aeolus is predominantly below the tropopause around the jet level and then decreases with altitude for forecast lead times of 24 to 72 h. Only

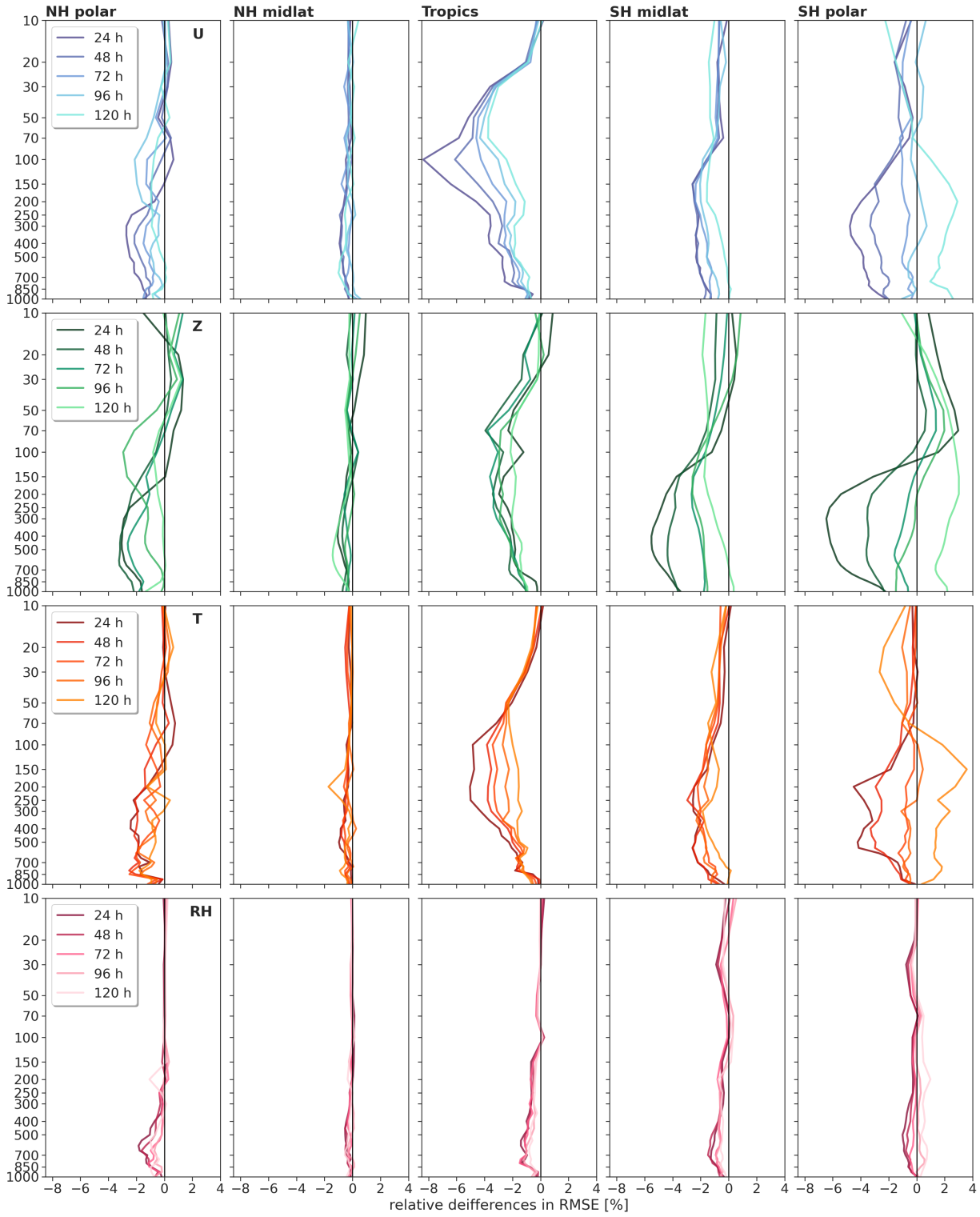

Figure 5.4: *The mean relative differences in RMSE [%] of zonal wind component (U), geopotential (Z), temperature (T), and relative humidity (RH) as function of pressure [hPa] for the tropics, the midlatitudes (NH midlat, SH midlat) and polar region (NH polar, SH polar) of both hemispheres for 01 July 2020 to 30 September 2020 as function of altitude for forecast lead times from 24 up to 120 h.*

relative humidity exhibits a second peak in the Southern Hemisphere in the stratosphere, which aligns with the impact results when verifying against GPSROs. Presumably, the impact on relative humidity is mainly caused by improved winds leading to improved advection of humidity and a resulting relative reduction in the humidity RMSE up to 2%. In the midlatitudinal troposphere of the Southern Hemisphere, the RMSE is reduced up to 3% for the zonal wind and temperature and even up to 6% for geopotential. In the midlatitudes of the Northern Hemisphere, Aeolus observations lead to an average improvement of up to 1%, which is again consistent with the changes in forecast errors verified against wind and temperature observations from radiosondes, aircraft, and AMVs (Sec. 5.1.2). Towards the polar regions, the differences in impact between forecast lead times shorter and longer than three days become larger. Especially in the Southern Hemisphere, differences in the sign of the impact occur with increased degradation in forecast quality for the 96 and 120 h forecast. However, this may be induced by the strong systematic differences between ERA5 based on the IFS model and the ICON experiments in these areas (Fig. 5.1).

Spatial distribution of the Aeolus impact

In the subsequent Sec. 5.2 regions of particularly pronounced impact of the Aeolus observations and the underlying dynamical scenarios are discussed. The selection of these regions is motivated by Fig. 5.5, which provides an overview of the spatial distribution of the relative forecast error reduction and Table 5.2 displaying the average values for the different climate zones.

The spatial distribution of the relative RMSE reduction reveals that above the tropical tropopause, the beneficial impact is primarily located around the equatorial band (Fig. 5.5a). The forecast errors of forecast lead times from 24 to 120 h are reduced by almost 5% on average. On large scales, this region is affected by the quasi-biennial oscillation of the zonal wind, the QBO. The OSE period covers the change in the circulation state associated with evolving westerly winds, which was strongly strengthened in the analysis by the assimilation of Aeolus observations (Sec. 5.1.1). Sec. 5.2.1 evaluates the hypothesis that there is a relation between the QBO phase change and the large impact of Aeolus.

Furthermore, large forecast error reduction can be found in the 300-hPa zonal wind in the midlatitudes in the Southern Hemisphere and the tropics with an average improvement of 1.7 -2.6%. The midlatitudes in the Southern Hemisphere overall show a fluctuating impact pattern. However, the most pronounced forecast error reduction appears around the storm track region downstream of South America. In the tropics, striking forecast error reduction is located around the Eastern Pacific Ocean and the subtropical jet over South America at 300 hPa. The large-scale dynamics there are mainly dominated by the coupled circulation system ENSO which is characterized by the interaction between surface temperatures and upper-level winds. Large systematic changes in the analysis over the Eastern Pacific due to the assimilation of Aeolus observations in the OSE were found in Sec. 5.1.1 in the form of a strengthening of easterly winds. The OSE covers the onset of a shift in ENSO conditions which is generally associated with modifications in the tropical circulation pattern of the zonal and vertical wind. The changes in the wind pattern are assumed to be the dynamical source of the large Aeolus impact and are discussed in more detail in Sec. 5.2.2).

(a) U 50 hPa U

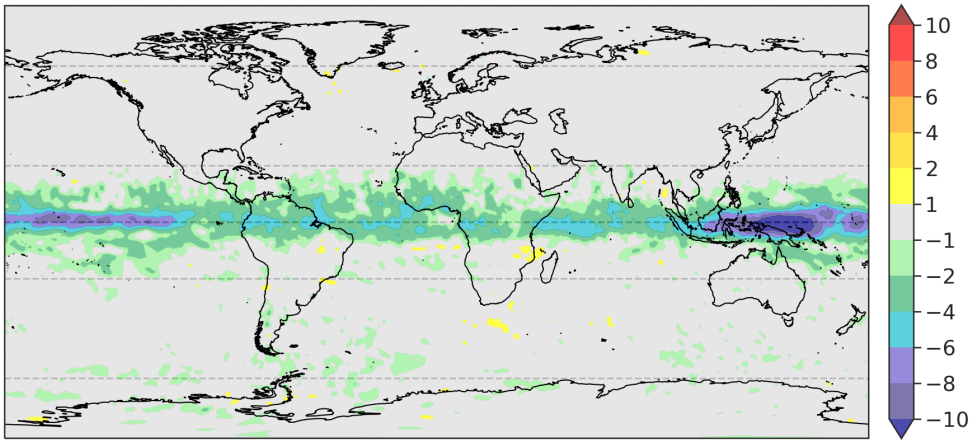

(b) U 300 hPa U

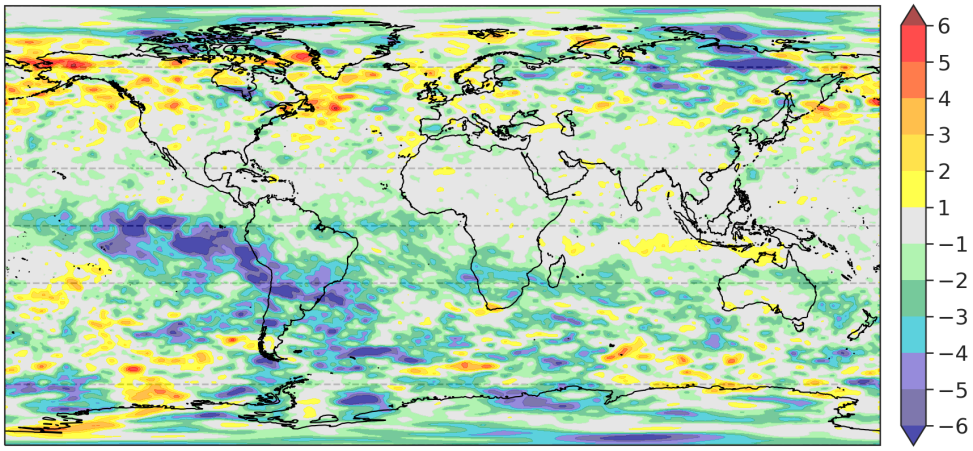

(c) Z 500 hPa

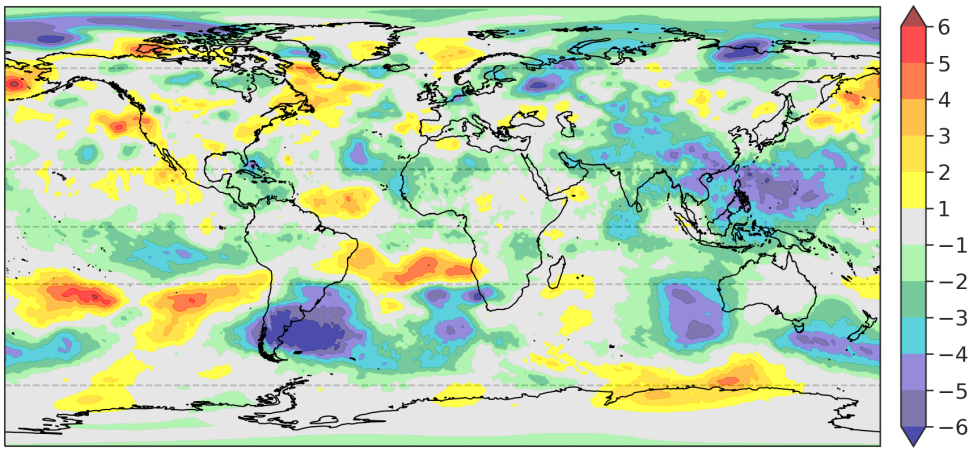

Figure 5.5: *The mean relative differences in 24 -96 h forecast RMSE between the EXP_A and the CTRL run [%] as function of pressure [hPa] for 01 July 2020 to 30 September 2020, (a) 50-hPa zonal wind component (U), (b) 300-hPa zonal wind component (U), and (c) 500-hPa geopotential (Z).*

	[-90°,-65°)	[-65°,-23.5°)	[-23.5°,23.5°]	(23.5°,65°]	(65°,90°]
U 50 hPa	-0.78	-1.05	-4.84	-0.26	-0.54
U 300 hPa	-1.16	-1.72	-2.64	-0.47	-1.43
Z 500 hPa	-0.10	-1.71	-1.87	-0.74	-1.56

Table 5.2: *Mean relative difference in 24 -120 h forecast RMSE between the EXP_A and the CTRL run [%] averaged over the polar, midlatitude, and tropical region in the Northern and Southern Hemisphere for 50-hPa zonal wind component (U), 300-hPa zonal wind component (U), and 500-hPa geopotential (Z).*

Further north, in the 500-hPa geopotential, large forecast error reduction occurs near the Northern Hemisphere turning circle in the western Pacific and Atlantic. These are regions of tropical cyclone activity in the experimental period. Furthermore, large improvements can be seen in the Southern Hemisphere storm track areas, such as the Indian Ocean, the eastern side of Australia, and the region near 30°S over South America. On average, forecast errors are reduced by 1.9% in the tropics and by 1.7% (0.7%) in the Southern Hemisphere (Northern Hemisphere) midlatitudes.
Overall, the mean impact pattern in the Northern Hemisphere is characterized by large variability likely related to fluctuations of the polar jet and the associated midlatitude circulation that partially obscures the mean error reduction. Large forecast error reduction over continents occurs over the Himalayan region, India and Eastern Asia. Moreover, both the zonal wind on 300 hPa and geopotential on 500 hPa show large improvements of 1.4-1.6% in the polar region in the Northern Hemisphere. Aeolus's impact in these regions may be investigated further in future investigations. This study further examines the spatiotemporal evolution of forecast error reduction in midlatitudes to better understand the impact of Aeolus in relation to the general midlatitude circulation and to identify associated specific extratropical weather systems with a particular focus on the ET of tropical cyclones (Sec. 5.2.3).

5.2 Investigation of links between dynamical scenarios and particularly high impact of Aeolus on NWP forecasts

5.2.1 Impact on tropical stratospheric wind variations (QBO)

Systematic changes in the analysis field (Sec. 5.1.1) and improvements in forecast quality of the stratospheric zonal wind field (Fig. 5.5a) indicate an impact of the Aeolus observations on the QBO phase change from easterly to westerly that took place in summer 2020. In order to better monitor the QBO in 2020, Aeolus's vertical range bin setting was adjusted to allow for measurements up to 25 km in the tropics. This advanced setting was active in the tropical belt ±10° once a week for 24h only, from Wednesday, 01:00 am UTC until Thursday, 01:15 am UTC. Fig. 5.6 focuses on the impact of Aeolus HLOS observation between 30 and 50 hPa around the equator, showing the time evolution. After an unusual disruption of QBO cycling in winter 2019/2020 (Anstey et al., 2021), the regular oscillation

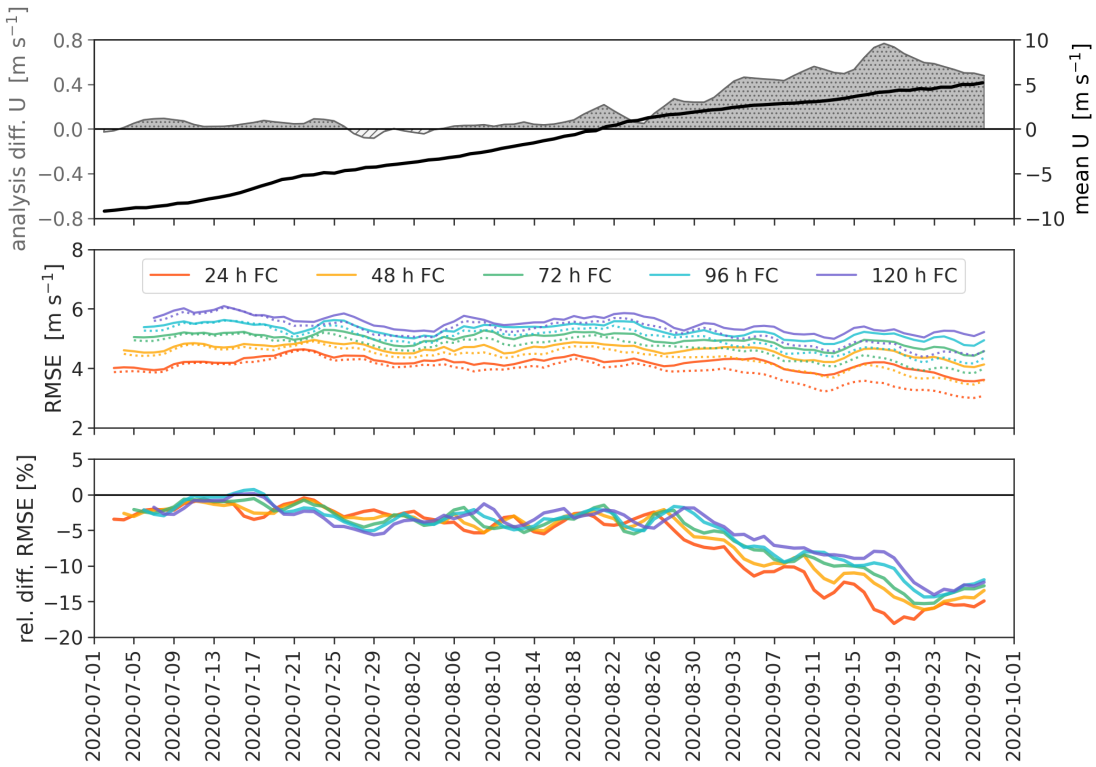

Figure 5.6: *Time series for the tropical belt ±10° latitude between 30 and 50 hPa. Top row: the mean zonal wind (black line) and the mean analysis differences in the zonal wind between EXP_A and CTRL (shaded grey). Middle row: the RMSE for forecast lead times from 24 to 120 h for the CTRL (solid line) and the EXP_A (dotted line) run. Bottom row: relative differences in RMSE between EXP_A and CTRL for forecast lead times from 24 to 120 h.*

in that stratospheric layer emerged again as an eastward jet around 20 August. The Aeolus observations affect the change in zonal mean wind from easterly to westerly in the way that the evolved westerly winds are strengthened in the ICON model. The forecast errors of the CTRL run are fairly constant with time, only slightly varying between 4 and 6 m s^{-1}. On the other hand, the forecast errors of the EXP_A noticeably decrease with time. The relative differences in RMSE between EXP_A and CTRL already show improvements in the quality of the zonal wind forecast by the Aeolus observations at the beginning of the OSE period. The reversal of the zonal wind direction is then accompanied by a marked reduction in the RMSE for all lead times. Towards the end of September, improvements of 10% to over 15% occur.

It should be taken into account that both the ERA5 reanalysis used for verification and the global model ICON exhibit large uncertainties in the tropical stratosphere, probably contributing to the pronounced impact of Aeolus observations. The QBO is mainly driven by a combination of upward-propagating low-frequency equatorial waves and inertia-gravity waves from the troposphere that dissipate and deposit momentum to the upper level zonal-mean zonal winds (Shepherd et al., 2018). However, a realistic representation of the wave, mean-flow interaction behind the QBO is typically limited by insufficient vertical model resolution, uncertainties in parameterized processes such as tropical convection, and the sparseness of direct wind measurements in the tropics. Given the lack of direct wind observations in the area, the models there could be prone to biases.

Due to QBO teleconnections with other parts of the atmospheric system such as the polar vortex (Anstey and Shepherd, 2014, Baldwin et al., 2001, Gray et al., 2018) or tropical oscillations as, e.g., Madden-Julian Oscillation (MJO) (Martin et al., 2021b) and ENSO (Anstey et al., 2021), accurate prediction of the QBO by an additional observing system might also provide a meaningful source of longer-term predictive skill outside the tropics. Furthermore, several statistical studies showed that besides or in interaction with the ENSO, the QBO could also modulate the tropical cyclone activities over various oceans (Baldwin et al., 2001, Gray, 1984, Gray et al., 1992, Jury et al., 1999) and that the QBO west phase is usually associated with enhanced deep convection, both sides of the equator.

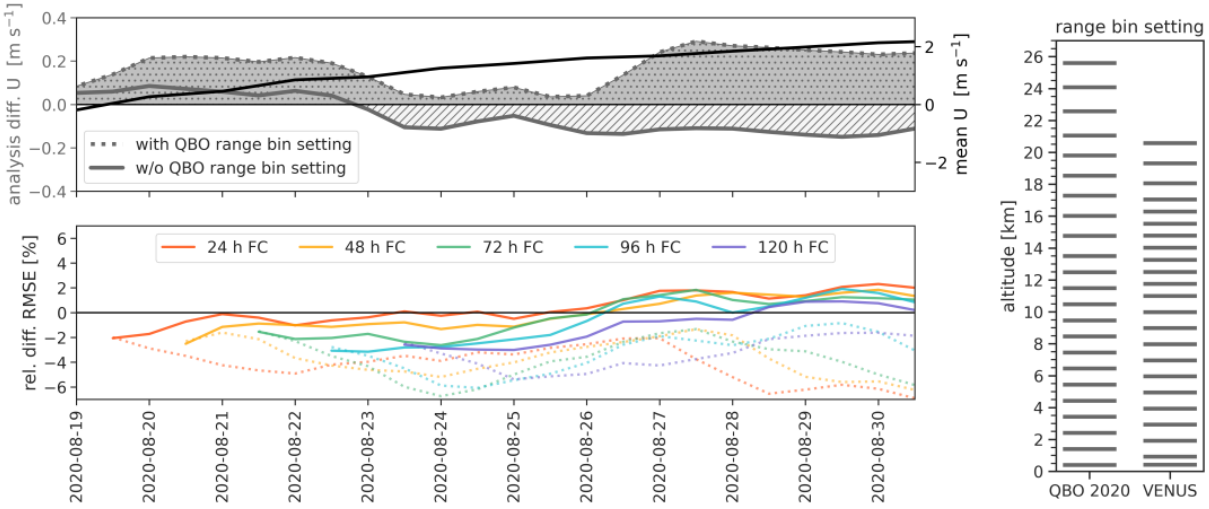

Figure 5.7: *Time series for the tropical belt ±10° latitude between 30 and 50 hPa. Top row: the mean zonal wind (black line) and the mean analysis differences in the zonal wind between EXP_A and CTRL (shaded grey), with (dotted line) and without (solid line) the QBO range bin setting. Bottom row: relative differences in RMSE between EXP_A and CTRL for forecast lead times from 24 to 120 h, with (dotted line) and without (solid line) the QBO range bin setting. The distribution of the general tropical range bins (VENUS) and the advanced QBO setting is illustrated on the right.*

Both accurate Aeolus wind measurements in the stratosphere and a good capture of upward propagating waves from the lower levels can cause the strong positive impact on the QBO phase change. To exclude the influence of the extended special QBO range bin setting, which amplifies the effect of the stratospheric Aeolus observations, another experimental run, with a shorter period of 14 days, was performed. For this, the Aeolus observations between Wednesday, 01:00 am UTC until Thursday, 01:15 am UTC were not used in the assimilation. Fig. 5.7 displays the relevant time series from 18 August 2020 to 31 August 2020 of the analysis differences and the relative differences in RMSE for the tropical belt ±10° latitude between 30 and 50 hPa. The experiment with and without the QBO range bin setting are compared. On the right, in Fig. 5.7 the distribution of the general tropical range bins (VENUS) and the advanced QBO setting is illustrated. The experiment's start covers the time when the QBO west phase manifested again. Whereas the Aeolus experiment with the QBO range bin setting shows a large influence in the analysis in the form of an intensification of the west winds, the exclusion of the high-resolution stratospheric Aeolus observations leads to a weakening of the west jet after a

few days. Striking differences also appear in terms of forecast error for lead times from 24 to 120 h. Initially, both experiments show beneficial effects in the equatorial stratosphere, but with time the forecast error reduction of the experiment without QBO range bin setting decreases up to degradation of 2%. As the stratosphere is characterized by large model uncertainties, a longer OSE would be useful to be able to draw firm conclusions. However, it is noteworthy that even within 14 days, the elimination of observations during two days of higher resolution Aeolus observations can have significant effects. This underscores the importance of the range bins settings for the Aeolus mission.

5.2.2 Impact on change in the ENSO state in the Eastern Pacific

In the equatorial region, the ENSO is another important tropical oscillation pattern whose interannual tropospheric variability influences both weather and climate on a global scale. It is characterized by periodic fluctuations through a neutral phase between warm (El Niño) and cold (La Niña) extremes in sea surface temperature (SST) across the equatorial Pacific Ocean. In summer 2020, the state of ENSO changed from neutral to the La Niña state. The ENSO phases relate to the zonal Walker circulation, that is strengthened during La Niña events as the eastern Pacific is colder and the western Pacific is warmer than on average, leading to an enhanced rise of warm moist air over Indonesia and South America and an enhanced downward branch over the mid-Pacific. Fig. 5.8 displays the time evolution of differences in 48 h forecast RMSE of the zonal wind component averaged over the equatorial Eastern Pacific [5°S-5°N, 90°W-160°W] as a function of altitude. The shift in the ENSO conditions is associated with a major change in the wind patterns of the tropical belt that appear to be strongly influenced by the assimilation of Aeolus wind observations. The three-month average equatorial Pacific SST anomaly (Oceanic Niño Index (ONI)) is a common measure and NOAA's primary indicator for monitoring the state of ENSO. Around 8 August 2020, the SST anomaly, determined as the difference from the average ERA5 reanalysis from 1985 to 2015, exceeds the -0.5 K threshold, indicating the presence of La Niña conditions. This point in time is the beginning of a large forecast error reduction for upper-level zonal wind. The reduction in forecast error increases over the 14 days after the La Niña onset and extends into the middle troposphere. Enhanced improvements continue to occur afterward and are also apparent in a shorter period before the onset. The largest error reduction in the 48 h forecast occurs about 48 h after the strongest negative increase in the SST anomaly, which corresponds to the initialization time.

Together with the results of Sec. 5.2.1, this suggests that Aeolus particularly reduces uncertainty in the model representation at the beginning of variations in the large-scale circulation systems. The better representation of the ENSO pattern, as provided by the HLOS winds in the ICON model, is expected to have a variety of further beneficial impacts. The fluctuations in the ENSO pattern can, for example, greatly affect the location of tropical rainfall and wind patterns. Moreover, influences on the extratropics are possible via the interaction with Rossby wave trains (Hoskins and Karoly, 1981), the North Atlantic Oscillation (NAO) phase (Rogers, 1984) or the Pacific-North American Pattern (PNA) (Horel and Wallace, 1981), but also through planetary wave activity into the stratosphere (Iza et al., 2016).

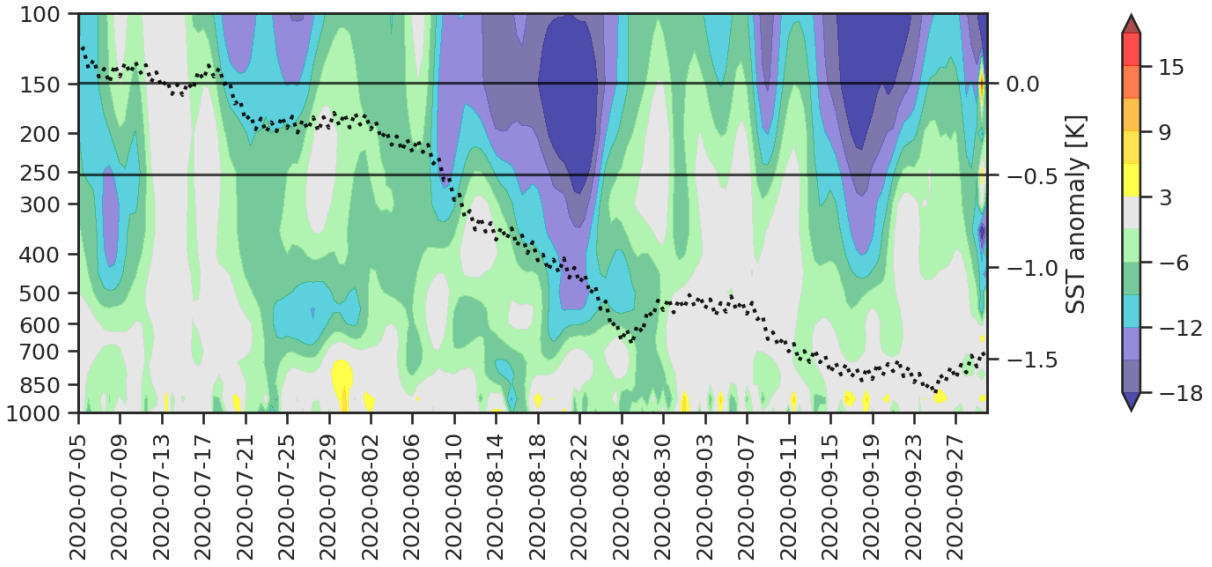

Figure 5.8: *Relative differences in 48 h forecast RMSE of the zonal wind component [%] between EXP_A and CTRL [5° S-5° N, 90° W-160° W] as function of forecast time and pressure [hPa]. The black dotted line is the sea surface temperature (SST) anomaly from ERA5 reanalysis 1985 to 2015.*

5.2.3 Dynamical impact in the midlatitudes

Hovmöller diagrams are a common way of data plotting in meteorology to display both the change over time and the spatial variability of a variable. In particular, they serve to highlight the behavior of atmospheric waves. To identify dynamical sources of the extratropical influence of Aeolus in the Northern Hemisphere, Fig. 5.9 represents the latitudinal average between 25° and 60°N of the 250-hPa meridional wind field and the convective precipitation as a function of longitude and time from 8 July 2020 to 19 July 2020. The dashed black contour lines display the largest error reductions in the 48 h forecast of 500-hPa geopotential. At the beginning of the time period shown here, tropical cyclone Fay, which originally formed from a surface low over the northern Gulf of Mexico, emerged into the western Atlantic Ocean. The storm intensified while moving northward, reaching its peak intensity on 10 July. Later that day, Fay made landfall over New Jersey and interacted with the midlatitude upper-level flow. The Hovmöller diagram shows pairs of green/blue and orange/red patches that form a clear banded pattern from 70°-80°W around 10 July all the way to Europe on 15 July, representing individual troughs and ridges of an RWP. The contour lines related to the reduction in the 48 h forecast error of the 500-hPa geopotential are associated with this wave structure.

ET typically involves a complex interaction with the midlatitude baroclinic environment, which causes considerable changes in the characteristics of the cyclone (Grams et al., 2013). Interactions with the midlatitude waveguide can lead to increased forecast uncertainty, mainly associated with upper-level divergence, vertical wind shear, and cirrus clouds (Jones et al., 2003). Therefore, it is expected that a good Mie wind coverage with a comparatively high resolution can have positive effects. In general, there is no commonly accepted definition of ET, but various classification factors have been proposed for a typical ET event. In Jones et al. (2003), a definition of a two-stage classification of ET based on Klein et al. (2000) can be found. Typically, when the cyclone is affected by vertical wind shear

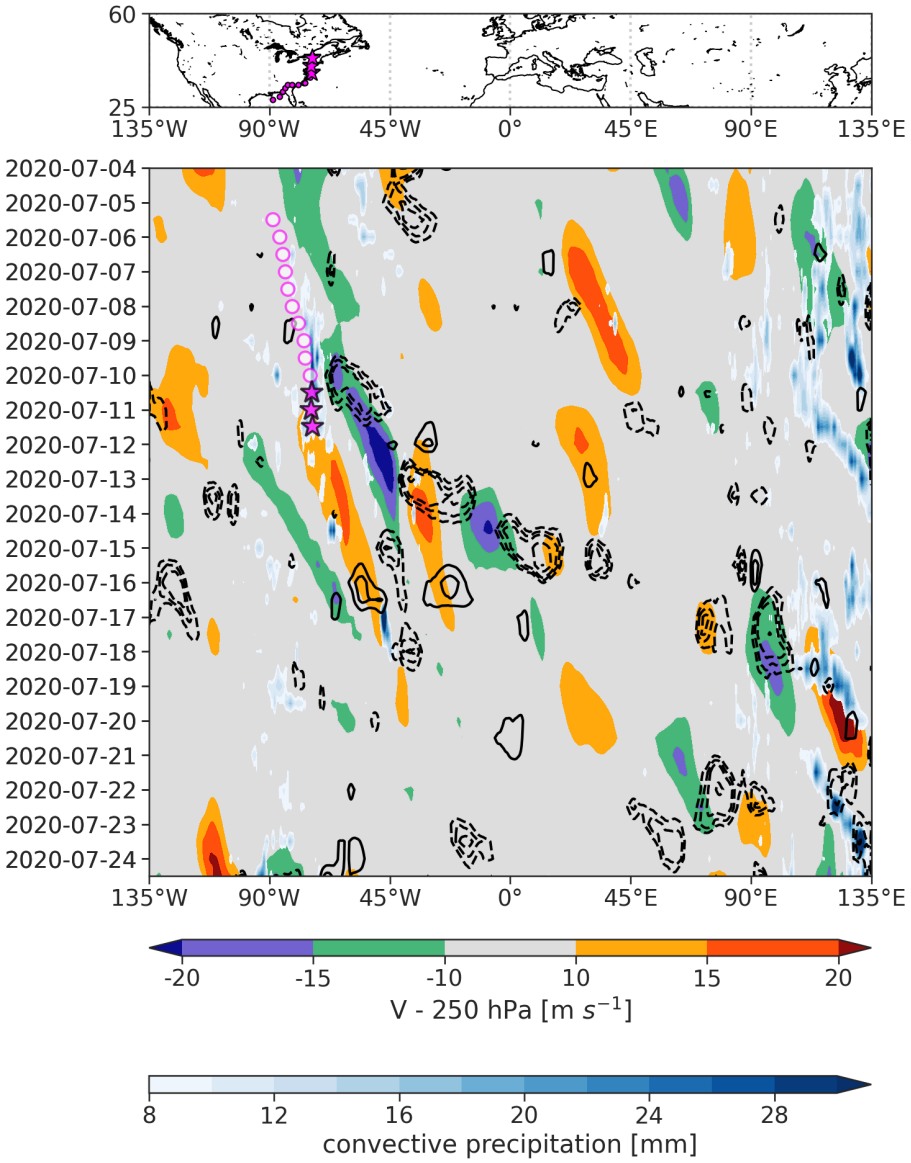

Figure 5.9: *Hovmöller diagram of the 250-hPa meridional wind (color shading, in m s*$^{-}$*1) for 4 July 2020 to 24 July 2020 and the convective precipitation averaged between 25° and 60°N. The black contours are the largest differences of the 48 h forecast error of 500-hPa geopotential between EXP_A and CTRL (dashed: negative, solid: positive). The magenta circles mark the position of cyclone Fay; the stars highlight the onset of the ET and interaction with the midlatitude flow.*

associated with the baroclinic zone, the axisymmetric structure of the tropical cyclone around the core is distorted, resulting in an asymmetry in the wind and thermal structures and consequently in the moisture, cloud, and precipitation fields. The upper-tropospheric divergent outflow, which appears as a cirrus cloud shield, may directly impact the large-scale midlatitude flow by interacting with the upstream trough of the midlatitude jet. Due to the tropical origin, low potential vorticity (PV) is advected by the divergent flow, which leads to a strengthening of the meridional PV gradient. This results in an amplification of the jet streak and the development of a ridge-trough couplet downstream of the transitioning cyclone, which marks the generation of a new RWP or the modification of an existing one (Wirth et al., 2018). The RWP then disperses further downstream and can

contribute to the development of strong cyclogenesis or atmospheric blocking anticyclones (Riboldi et al., 2019). Therefore, ET associated with the amplification of RWPs may also lead to high-impact weather in distant downstream regions (Keller et al., 2019). The many different atmospheric processes involved in ET events pose a major challenge for NWP models. They can considerably reduce the skill of the medium-range forecasts downstream of the tropical cyclone (Jones et al., 2003).

It is suggested that the evolution of the reduction in the 48 h forecast error displayed in the Hovmöller diagram is related to the interaction of Fay undergoing ET with the midlatitude waveguide. The downward propagation of the forecast error reduction seems to be similar to the group velocity of the RWP. This picture fits the theory described by Keller et al. (2019), that uncertainties in the ability to predict ET events typically first manifest as uncertainties in the prediction of the strengthening of the downstream ridge and then propagate with the evolving RWP.

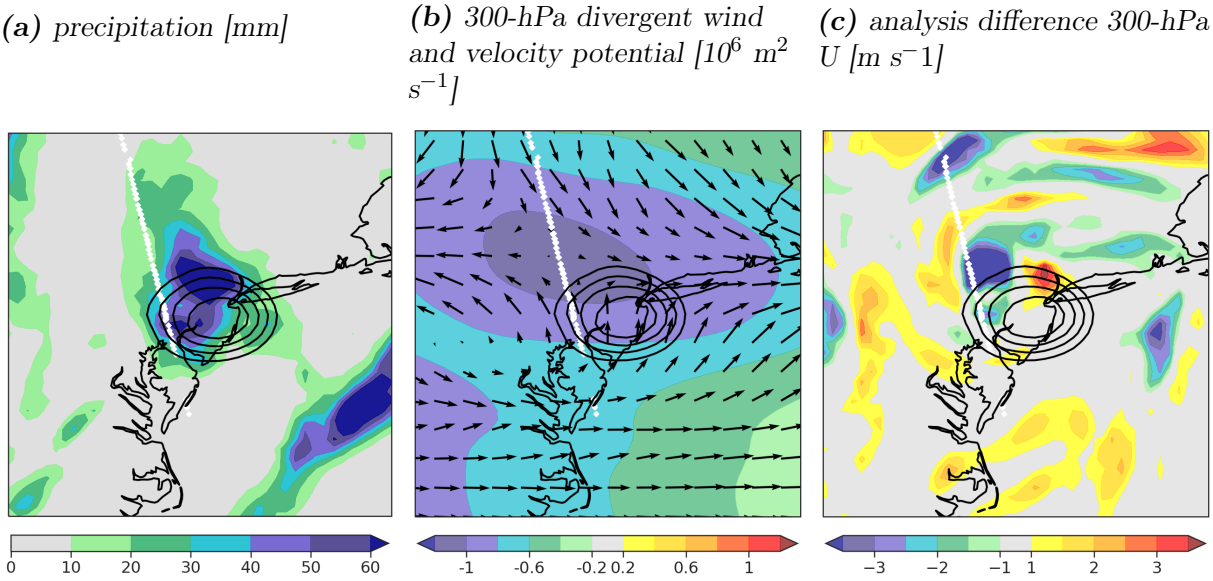

Figure 5.10: *Precipitation (a), 300-hPa divergent wind (vectors) and velocity potential (b), and the analysis differences in 300-hPa zonal wind between EXP_A and CTRL (c) for 10 July 2020 12 UTC for the region around cyclone Fay [35°-45° N, 80°-70° W]. The black contours represent the minimum surface pressure.*

Fig. 5.10 focuses on the time around the onset of the ET of Fay. The contour lines are the minimum surface pressure showing Fay making landfall. Pronounced values in the divergent wind field of the upper troposphere (Fig. 5.10b) occur northwest of the cyclone center, representing the poleward expanding and anticyclonically rotating outflow. Characteristic for ET events are the regions of significant precipitation embedded in the cloud shield apparent in Fig. 5.10a. The rain field tends to be located to the west of the cyclone center. The Mie wind observations from Aeolus assimilated at this time cover the area of the diverging flow very well, which could be the origin of the forecast improvements in the Hovmöller diagram right at the beginning of the RWP development. The differences in the zonal wind on 300 hPa (Fig. 5.10c) exhibit an increased influence of Aeolus observations in terms of both west and east wind acceleration around the region of the interaction of the cyclone with the large-scale flow.

(a) *2020-07-10 12UTC: analysis*

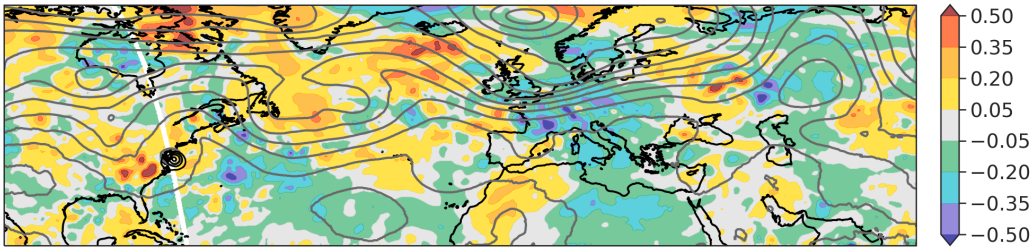

(b) *2020-07-11 12UTC: 24 h forecast*

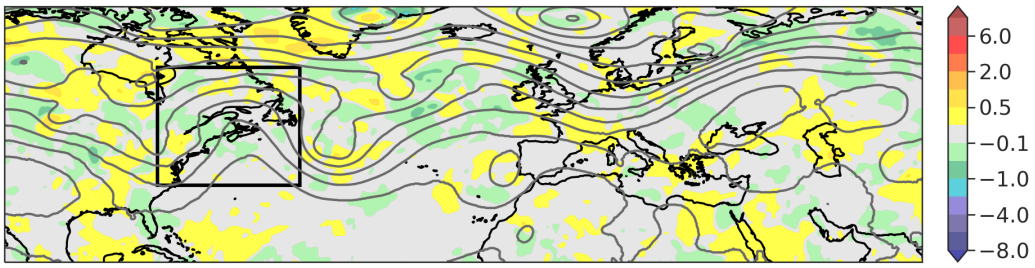

(c) *2020-07-12 12UTC: 48 h forecast*

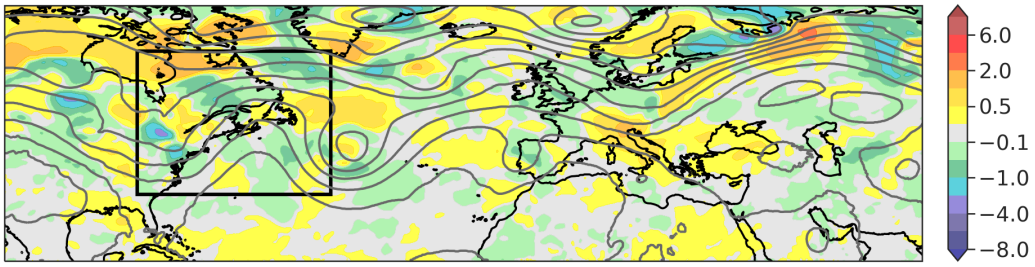

(d) *2020-07-13 12UTC: 72 h forecast*

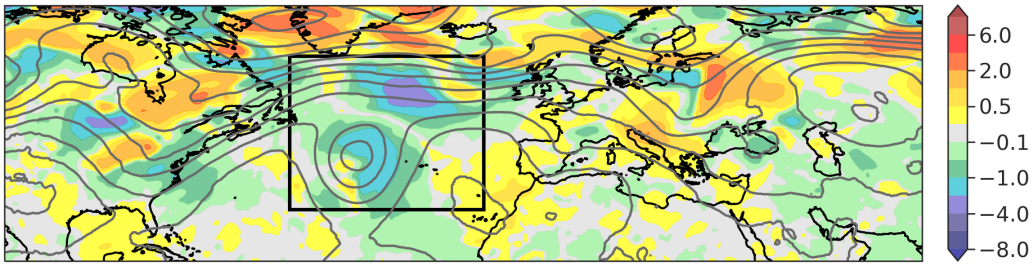

(e) *2020-07-14 12UTC: 96 h forecast*

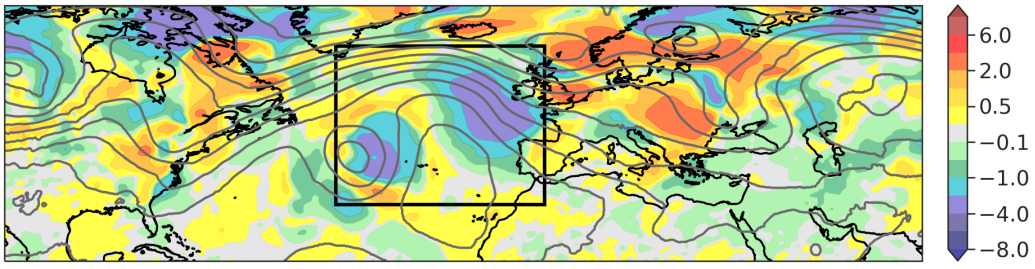

(f) 2020-07-15 12UTC: 120 h forecast

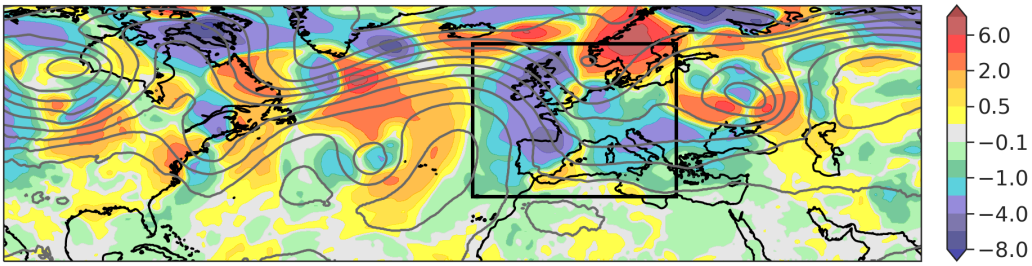

(g) 2020-07-16 12UTC: 144 h forecast

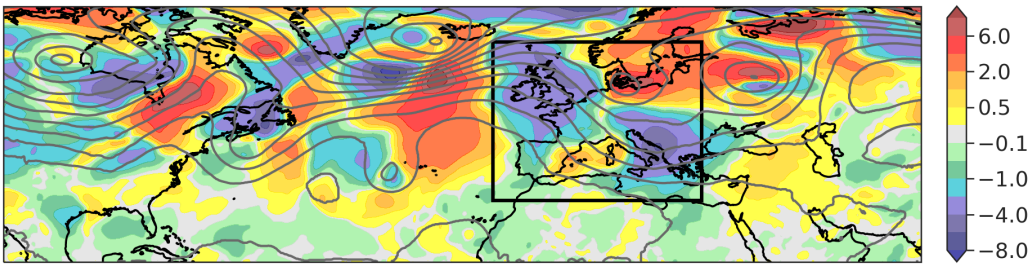

Figure 5.11: *Downstream impact of Aeolus on 500-hPa geopotential from forecast start 10 July 2020 12 UTC for the region [20°-70°N, 110°W-70°E]. (a) The differences in the analysis of between EXP_A and CTRL for 10 July 2020 12 UTC, the white line is the Aeolus track, the black contours are the minimum surface pressure, (b) differences in 24 h forecast error (EXP_A - CTRL) - 11 July 2020 12 UTC, (c) differences in 48 h forecast error - 12 July 2020 12 UTC, (c) differences in 72 h forecast error - 13 July 2020 12 UTC, (d) differences in 96 h forecast error - 14 July 2020 12 UTC, (e) differences in 120 h forecast error - 15 July 2020 12 UTC, (f) differences in 144 h forecast error - 16 July 2020 12 UTC. The box highlights the area of interest associated with the ET event; the grey contour lines represent the 500-hPa geopotential from ERA5 reanalysis in 5 gpdm steps.*

The forecast impact on the course of downstream development after the ET event is displayed in Fig. 5.11 by the differences in forecast errors of the 500-hPa geopotential between EXP_A and CTRL for lead times from 24 to 144 h. All forecasts are initialized on 10 July 2020 12 UTC. Fig. 5.11a shows the analysis differences at this time, when Hurricane Fay is located ahead of the upstream trough of the jet and the Aeolus track passes directly over the cyclone and trough front. A large analysis influence is visible in the areas around the cyclone, especially at the trough axis. The evolution of the Aeolus impact described in the following is believed to be related to either better coverage of upper troposphere outflow associated with the latent heat release of cyclone Fay or/and reduction of uncertainties in the dry baroclinic upper-level flow dynamics. In the 24 h forecast (Fig. 5.11b), only small effects of the Aeolus observations on the midlatitude flow are visible in the region around the amplifying ridge, presumably related to the outflow. However, due to the assimilation cycling, the effects cannot be clearly assigned, but it is assumed that previous measurements and the cycling lead to differences in the cyclone as well as in the jet environment. The improvements become more distinct in the 48 h forecast (Fig. 5.11c) where the area of forecast error reduction moved towards the deepening trough downstream. One day later (Fig. 5.11d), a distinct RWP with a ridge–trough

couplet and cyclogenesis over the northern Atlantic Ocean developed. This cyclogenesis and the region of the jet streak above are associated with a large reduction of 72 h forecast error. Subsequently, the impact propagated downstream over the East Atlantic (Fig. 5.11e). Fig. 5.11f shows a clear wave structure in the 500-hPa geopotential, from the east coast of America to Europa. The 120 and 144 h forecast error differences (Figs. 5.11f and 5.11g) highlight the area of increased error reduction spreading eastwards across the whole of Europe. This spatial perspective of the individual forecast times along the wave packet further supports the assumption that the downstream forecast improvement is related to the Aeolus observations in the preceding ET of Fay.

The data denial experiment period includes a large part of the tropical cyclone season, and additional ET cases associated with forecast error reduction associated with the assimilation of Aeolus observations are detected. Fig. 5.12 shows three further examples of Hovmöller diagrams for ET and the spatiotemporal evolution of RWPs as well as differences in 500-hPa geopotential forecast error covering the time period of Hurricane Laura (Fig. 5.12a), Hurricane Paulette (Fig. 5.12b) and the two Typhoons Bavi and Maysak in the western Pacific (Fig. 5.12c). As in Fig. 5.9, wave-like structures in the meridional wind component that form or intensify around the beginning of the ET are visible. However, the RWPs are not as pronounced as in Fay's ET event. Furthermore, the correspondence between the propagation velocity of the impact structures and the RWP does not seem to be as clear. But it was found that the area around the upper-level divergent flow of the ET examples in Figs. 5.12a to 5.12c were all well-captured by the Aeolus Mie observations during the onset of the transition (not shown here). Therefore, some impact on the downstream development of the RWPs to Europe or for the Typhoons to America can be assumed. The impact of Aeolus observations on tropical cyclone tracks has also been investigated. However, no significant improvements were found. This may be related to the lack of observations beneath clouds and consequently within and nearby the cyclone, but it could also be due to the need for a large sample size when evaluating tropical cyclone tracks. Apparent is the connection of all cyclones to heavy precipitation. The importance of upscale error growth from convective to larger atmospheric scales limiting the predictability in NWP is discussed in several recent studies (e.g. Hohenegger and Schär, 2007, Rodwell et al., 2013, Selz and Craig, 2015, Selz et al., 2022). Selz et al. (2022) found that latent heat release in convective systems and the divergent component of the atmospheric flow dominate the error growth with respect to physical processes. It is assumed that accurate observations of the divergent wind field as expected from the Aeolus winds can reduce the uncertainty of the initial conditions around mesoscale convective ET events, but also in cyclogenesis regions in other parts of the world.

Fig. 5.12d shows an example of an RWP developing in the region over southern South America, expected to be related to the clear structure of the largest forecast error reduction in 500-hPa geopotential. Typically, in the Southern Hemisphere winter season, cyclogenesis is associated with the subtropical jet in the lee of the Andes in South America (Hoskins and Hodges, 2005). Berbery and Barros (2002) discussed the strong moisture transport in winter and spring from the tropics into the La Plata River basin on the eastern side of the Andes and the importance of the associated latent heat release for subtropical cyclogenesis process. The increased beneficial impact of the Aeolus observations in this region along the subtropical waveguide on the Southern Hemisphere has already been shown in the mean forecast error reduction in 500-hPa geopotential in Sec. 5.1.3 (Fig. 5.5c). This might

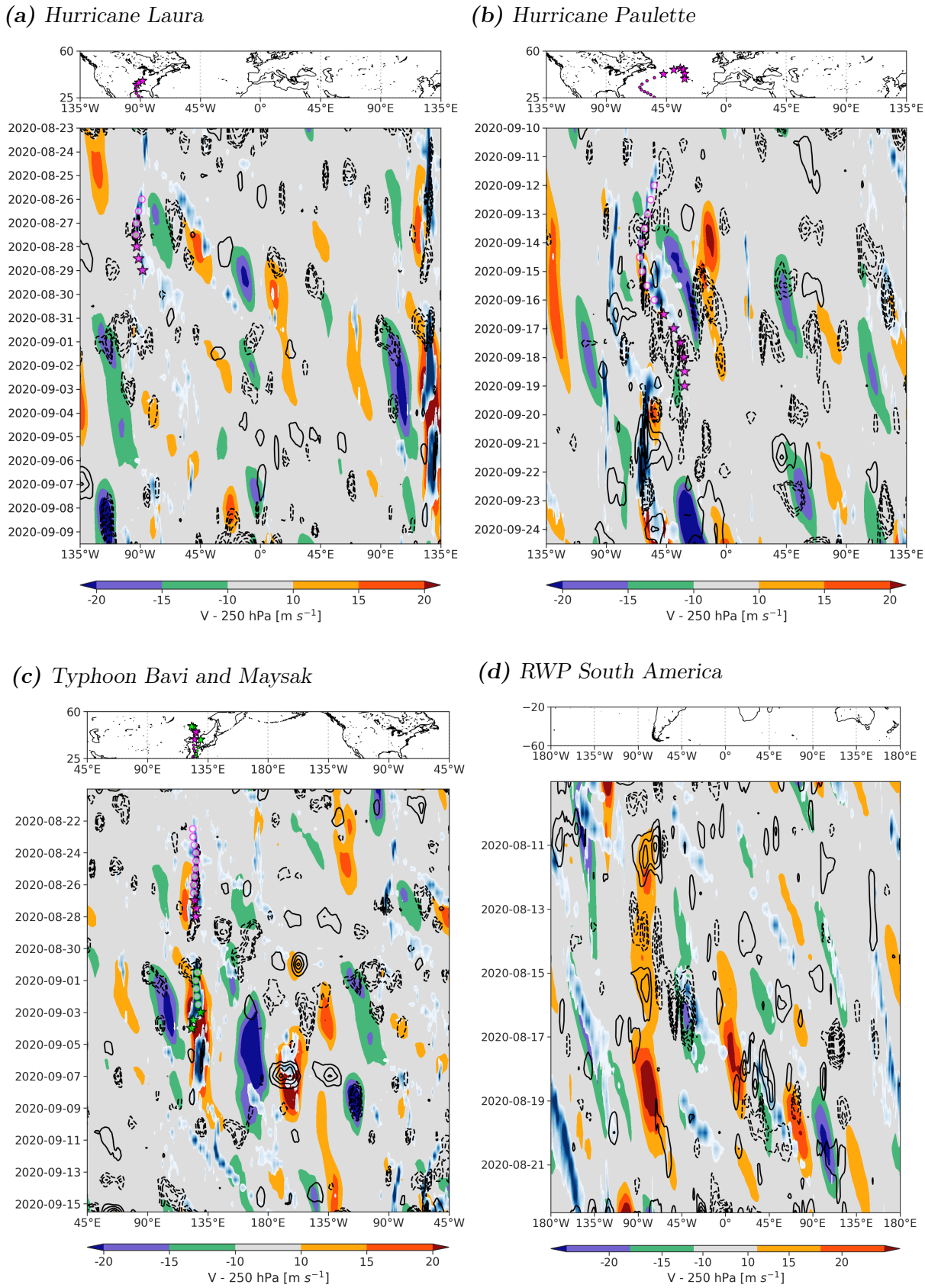

Figure 5.12: *Same as Fig. 5.9 for the ET event of (a) Hurricane Laura, (b) tropical cyclone Paulette, and (c) Typhoon Bavi and Maysak, and (d) an RWP development around the cyclogenesis region over South America.*

be related to good Mie wind observations in moist areas associated with cyclogenesis, capturing the onset or modification of orographically excited RWPs. Overall, there is significantly less knowledge available for the storm tracks in the Southern Hemisphere than in Northern Hemisphere, which has been observed and examined more comprehensively in the past.

5.3 Concluding remarks on the impact of Aeolus HLOS wind assimilation in the global model ICON

The Aeolus HLOS wind profile observations account for approximately 2% of the assimilated observations at the global model ICON at DWD. Based on an OSE consisting of two continuous assimilation runs with and without the assimilated Aeolus observations, their impact has been investigated globally and for regions and time periods of particularly large forecast error.

The reduction in forecast error was found to be largest in the tropical upper troposphere and stratosphere as well as in the mid- and upper troposphere of the Southern Hemisphere. The Northern Hemisphere shows a somewhat smaller but still beneficial impact of Aeolus observations. The mean relative reduction in short-range forecast error when verifying against other conventional observations was found to be between 0.1% and 0.6% in the Northern Hemisphere and up to 1.6% in the tropics and the Southern Hemisphere. On a global average, the forecast errors of zonal wind, temperature, and geopotential up to five days lead time are reduced by 2-4% when assimilating the Aeolus HLOS winds. In the upper troposphere and lower stratosphere of the tropics, where the largest impacts were expected, improvements of even 5-8% were observed. For these regions, ECMWF (Rennie et al., 2021) and Météo-France (Pourret et al., 2022) reported a reduction in the root mean square error (RMSE) of about 2%, which was verified using operational analyses. At the National Oceanic and Atmospheric Administration (NOAA) (Garrett et al., 2022), a reduction of up to 4% was observed. The slight discrepancies compared to the impact study with the ICON model are likely due to differences in the data assimilation systems and the set up of the OSEs. The potential of Aeolus HLOS wind observations in NWP models depends on the number and quality of observations but also on the description of background error covariances in the data assimilation system that defines the spread of observed information in model space. Furthermore, the analysis used for verification can affect the results of the OSEs.

To better understand the underlying dynamics leading to the overall promising statistical improvements, specific dynamical changes and processes related to the positive impact of Aeolus observations have been investigated. In the tropics, two weeks of large improvement in the East Pacific west of the Peruvian coast and about five weeks in the global equatorial band in the stratosphere particularly stand out. These regions and periods are associated with a change in the phase of the large-scale tropical circulation systems, the ENSO and the QBO. In addition, it has been focused on the midlatitudes, where spatiotemporal surveys show large forecast error reduction following the ET of tropical cyclones and their interaction with the midlatitude waveguide. Overall, the results of this study show potential for further investigations of the dynamical effects of the assimilation of the Aeolus wind observations for both the higher latitudes in the Northern and Southern Hemispheres.

Chapter 6

Conclusions and Outlook

6.1 Main conclusions

Global wind profiles from the Doppler Wind Lidar (DWL) satellite mission Aeolus are an important recent supplement to the Global Observing System (GOS). The assimilation of the Aeolus horizontal line-of-sigh (HLOS) wind product is expected to significantly improve the initial state in Numerical weather prediction (NWP) and thus have a beneficial impact on the analysis and forecast. The overreaching goal of this thesis is to contribute to the optimal use of the novel Aeolus wind observations in NWP models.

To use the Aeolus observations in NWP data assimilation, the knowledge and minimization of their systematic errors are required. Furthermore, an observational error must be assigned to the DWL wind measurements. This thesis evaluated the quality of the novel Aeolus data set for effective use in NWP data assimilation systems through a comprehensive validation analysis with independent model and observation-based reference data sets. The estimation of the representativeness errors, which are an important contribution to validation statistics, then allowed the determination of the Aeolus observational error.

The impact of the Aeolus observations was quantified using the ICOsahedral Nonhydrostatic (ICON) model's global data assimilation system at Deutscher Wetterdienst (DWD). Besides a global statistical overview showing the largest forecast error reductions in the tropical upper troposphere and lower stratosphere, indications of atmospheric features and dynamical scenarios constituting pathways for significant improvement have been discussed. Aeolus observations have been shown to have a particularly large impact on the phase change of the large-scale tropical circulation systems, the Quasi-Biennial Oscillation (QBO) and the El Niño-Southern Oscillation (ENSO), but also on the midlatitude dynamics. Spatio-temporal analyses provided evidence for reducing downstream forecast errors associated with the interaction of cyclonic systems with the midlatitude waveguide. These results strongly motivate an Aeolus follow-on mission and the future use of space-based DWL observations in operational NWP.

Main conclusions: Validation of Aeolus HLOS wind observations

The **first research question** is concerned with the characterization of the systematic and random errors of the Aeolus wind observations as well as the estimation of the Aeolus observational error. This was addressed by providing a comprehensive validation statistic

using collocated radiosonde observations and two different global NWP models, the European Centre for Medium-Range Weather Forecasts (ECMWF) Integrated Forecast System (IFS) and the ICON model of DWD, as reference data. All validation results around the collocation points were compared for the midlatitudinal band 23.5−65° of the Northern Hemisphere. Additionally, a model-only global statistic was used to place the regional validation results in a global context.

A time series from the early stages of the mission showed that the systematic differences in Aeolus winds vary significantly with time, especially for the Rayleigh channel. Furthermore, it was found that the discrepancies between the ascending and descending orbital phases pose a challenge to the use of these data in NWP models. The three different reference data sets showed good agreement in estimating the systematic error, suggesting that the results are not driven by model biases. Slightly larger fluctuations in the systematic and random differences of the Mie wind observations compared to Rayleigh winds are likely due to uncertainties and discrepancies in NWP models in cloudy regions. The mean absolute systematic difference was found to be approximately 1.8 m s^{-1} for the Rayleigh winds and 1.6 m s^{-1} for the Mie wind observations. These values are beyond Aeolus's mission requirements, which state that the bias should be smaller than 0.7 m s^{-1}.

The mean random difference assessed in the validation analysis is about 3-5 m s^{-1} for the Rayleigh channel and 3-4 m s^{-1} for the Mie channel. Deviations between the radiosonde and model-based validation results of the random error estimates are mainly due to differences in spatial and temporal representativeness. The temporal changes in the random difference of the Rayleigh wind observations are believed to be primarily related to changes in the laser output energy. However, the return signal of molecular backscattering can also be affected by factors such as Doppler broadening or solar background noise, whereby the latter is associated with seasonal variations. The return signal from clouds typically is stronger, primarily depending on the presence of aerosols or hydrometeors and not on the laser energy. Thus, the random difference of the Mie wind observations is more stable and smaller than the random difference of Rayleigh wind observations.

To meaningfully evaluate the Aeolus observational error for the validation, the representativeness, as well as model and radiosonde observational errors, were determined. In particular, the higher spatial resolution of a radiosonde observation compared to the resolution of a global NWP model, the chosen collocation criteria, and the spatial and temporal shift during radiosonde ascents are sources of error that led to discrepancies between model-based validation and comparisons with radiosonde observations. The Aeolus observations correspond to a line measurement, whereby the NWP models treat the Aeolus HLOS winds as point measurements. Radiosonde observations can also be interpreted as a point measurement. Using regional Consortium for Small-scale MOdeling (COSMO-DE) analyses and high-resolution ICON Large Eddy Model (LEM) simulations, differences between a point and a 90 km (Rayleigh) or 10 km (Mie) line measurement were calculated. A large increase in the representativeness error was found with increased distance between the two measurement geometries and for specific altitude levels where wind gradients are strong. The results of the error estimation stress the importance of considering representativeness error sources when comparing the HLOS winds with other spatially and temporally offset observations. Accounting for all sources of error, the estimated Aeolus observational error for the comparisons with the ECMWF IFS model equivalents and radiosonde observations in the midlatitudes of the Northern Hemisphere was found to be between 4.3 and 4.5 m

s^{-1} for Rayleigh and about 2.5 (3.4) m s^{-1} for the Mie wind observations with 90 (10) km horizontal resolution. The Aeolus wind observational error estimates for the comparisons with the DWD ICON model equivalents is about 0.5 m s^{-1} smaller, probably due to differences in the description of background error covariances in the data assimilation systems of ECMWF and DWD. Overall, the Aeolus wind observational error showed increased values towards the upper troposphere and lower stratosphere, with the largest discrepancies between the validation reference data sets around the tropopause. It was therefore recommended to assign the errors in the data assimilation systems in such a way that less weight is given to the observations there.

The **second research question** asked how systematic errors can be corrected to optimize the use of the Aeolus wind observations in the data assimilation. The Mie wind bias was found to be relatively stable within the validation study. However, detailed investigations of the Rayleigh wind bias showed that it depends not only on the satellite's flight direction and the season but also on latitude and longitude. These detected bias dependencies were expected to be related to long-wave and solar radiation fluctuations and the associated response from the telescope's thermal control system. The spectrometers are very sensitive to small changes in the direction of the received laser light from the atmosphere that can cause apparent frequency shifts and hence a wind bias. The latitude variations and orbit differences were found to be particularly large during the Northern Hemispheric summer, which is the season with the largest latitude gradient in the asymmetric radiative response. A simple latitude-dependent bias correction approach based on the previous seven days was shown to be able to reduce the bias. However, a temporal trend of the remaining bias values still occurred. Taking both the latitude and the longitude dimension into account when correcting for the Rayleigh bias, the residual could be further reduced by nearly 50 % for the ascending and descending phases of the satellite's orbit. Although a near-real-time bias correction operationally implemented in April 2020 based on the linear correlations between O-B statistics from ECMWF and temperatures from the telescope primary mirror M1 eliminates most part of the systematic error, several NWP centers show a small residual bias. This remaining bias could be further reduced at DWD using the latitude-dependent bias correction scheme for specific altitude levels, thus improving the integration of the Aeolus observation in the assimilation system.

Main conclusions: Impact of Aeolus HLOS wind assimilation in the global model ICON

The **third research question** that motivated this thesis is how NWP might benefit from assimilating the novel DWL observations from the Aeolus satellite in the framework of the global assimilation system at DWD. To address this, a three-month Observing System Experiment (OSE) was conducted using the operational settings of the global model ICON and quality control based on the validation study. First, the systematic differences between the control and the Aeolus assimilation run in the analysis and the forecast errors were assessed on a global scale. Despite large random and complex systematic errors, the results of the global impact statistics indicate that the Aeolus observations are an important recent addition to the operationally assimilated observing system.

The systematic analysis influence of the Aeolus observations was found to be most pronounced in jet regimes, around large-scale circulation systems, and convectively active areas in the tropics. In the troposphere, the pattern of systematic changes appeared to be fairly constant over time. However, the equatorial stratosphere showed large systematic changes in the zonal wind analysis varying in time during the OSE period. All of these regions have above-average systematic analysis errors and poor observational coverage.

The largest forecast error reduction was found for the 2-3 day wind and temperature forecasts in the tropical upper troposphere and lower stratosphere and in the Southern Hemisphere. In the Northern Hemisphere, the Aeolus HLOS wind observations were found to have a less pronounced, but still relatively large, average impact compared to other observing systems. The verification with other conventional observations showed a mean relative reduction in short-range forecast error between 0.1% and 0.6% in the Northern Hemisphere and up to 1.6% in the tropics and the Southern Hemisphere. When verifying against the ECMWF Reanalysis 5th Generation (ERA5) reanalysis, forecast errors of the zonal wind, temperature, and geopotential up to five days lead time were found to be reduced by 2-4% on global average and even up to 5-8% around the tropical tropopause.

The **fourth research question** underlying this thesis concerns dynamical scenarios and processes that are related to particularly high impact. Regions with a very large reduction in forecast error in the OSE period were found in the equatorial band in the lower stratosphere and around the eastern Pacific at the tropospheric jet levels. The shift in the oscillatory phase of two important large-scale tropical circulation systems - the QBO and the ENSO - appeared to be associated with this large forecast error reduction due to the Aeolus observations. In August 2020, the stratospheric jet changed from east to west, which was found to be related to an improvement in the zonal wind forecast of about 10-15%. Further investigation suggested that the large impact in the equatorial band around 50 hPa was largely amplified by a special QBO range bin setting that has been adjusted to account for atmospheric winds up to altitudes of 25 km one day per week. This would mean that the improvements are mainly due to good measurements of the upper atmosphere and improved detection of vertically propagating waves. However, a longer accompanying experiment would be necessary for a precise assessment, especially since the stratosphere generally exhibits large uncertainties in NWP models.

In addition to the equatorial stratosphere, the tropical troposphere in the Pacific Ocean was found to be characterized by large-scale dynamical variability in August 2020. As indicated by the Oceanic Niño Index (ONI), the state of the Southern Oscillation changed from normal to the La Niña phase during this month. The associated strengthening of upper and middle tropospheric wind patterns in the eastern Pacific region, which is related to the zonal Walker circulation, was favorably captured by Aeolus.

Furthermore, the influence of Aeolus observations on midlatitude dynamics has been investigated. Although continents are already comparably well observed by other observation types, the impact study results showed that HLOS winds have a relatively large beneficial impact. However, the spatial distribution displayed that the effects are partially masked by fluctuations in the three-month mean flow. Systematically positive impact particularly stood out in storm track regions in the Southern Hemisphere, but some average improvements could also be seen in the Northern Hemisphere. Hovmöller diagrams were used to examine the spatiotemporal evolution of forecast error reduction, focusing

on oceanic regions and the midlatitude Rossby waveguide. Several cases of improvements associated with extratropical transition (ET) and the subsequent interaction with the midlatitude waveguide were found. The analysis of the tropical cyclone case Fay showed that the Mie channel of Aeolus quite well observed the divergent outflow during the onset of ET. Improvements in forecast quality of 500-hPa geopotential could be traced along the developing RWP propagating to Europe. Either the better coverage of upper troposphere outflow is linked to latent heat release or/and the reduction of uncertainties in the dry baroclinic upper-level flow dynamics were believed to cause the positive impact on the associated downstream development. Additional examples of ET events (Hurricanes Laura and Paulette and Typhoons Bavi and Maysak) support and motivate the potential of space-based lidar observation to impact the forecast quality of such scale-interacting dynamical processes. Furthermore, large forecast error reduction was found in the Southern Hemisphere around the development of an RWP likely associated with cyclogenesis in the lee of the Andes. Overall, the dynamical scenarios presented provide a good basis to lead the way for detailed future research on the impact of satellite-based DWL observations on NWP.

6.2 Outlook

This thesis addresses important challenges to the global observing system identified by the scientific community. Open research questions related to the optimal use of the Aeolus wind observations in NWP have been answered and potential pathways for a significant reduction of forecast errors through these additional space-based wind profile measurements have been discussed. The overall very large reduction in forecast errors and observed benefits for specific important dynamical systems motivate the exploitation of the Aeolus observations and support the preparation of a follow-on mission that the European Organisation envisages for the Exploitation of Meteorological Satellites (EUMETSAT). 4% improvements in NWP, as detected by the Aeolus observations, contribute an additional 2.6 billion euro to European GDP over a lifetime of 3.5 years (London Economics Space Team, 2022). Consequently, follow-on Aeolus operations have the potential to build on the existing mission success for the European society. The validation statistics of this thesis show which error sources and dependencies a future DWL satellite mission should expect and how these errors can be optimally reduced.

Future studies are proposed, in particular, to deepen the investigation of dynamic scenarios that lead to a significantly large impact of Aeolus on NWP predictions. Large-scale convective circulation systems in the tropics, such as the QBO and the ENSO, typically have high teleconnections with other atmospheric systems, e.g., through other oscillation phenomena in the extratropics or wave activity. Therefore, a poor representation of the variability of the large-scale tropical flow can lead to large uncertainties in many parts of the world. In addition to short- and medium-range NWP, seasonal and sub-seasonal forecasts are expected to benefit from the potential of the Aeolus observations to better represent the initial state of fluctuations in such large-scale circulation systems. Therefore, long-term research studies are suggested to also assess the weekly to monthly forecast skill. In addition, a longer OSE would be required to extend the investigation of tropical cyclone events. Tropical cyclones are not common events and the nature of sampling by Aeolus, which is only one single instrument on one satellite, makes it difficult to obtain

statistically significant results. Furthermore, it is proposed to deepen the investigation of the influence of HLOS winds on the interaction of small- or mesoscale convective systems with the upper-level baroclinic flow. Studying the influence of Aeolus on increased forecast errors or even forecast busts associated with these scenarios, in combination with feature-based diagnostics, would allow to evaluate the impact on the error growth representation. So far, the causes of forecast busts in the Northern Hemisphere are much better understood compared to the Southern Hemisphere. Therefore, a better assessment of the large impact found in the southern parts of the world would be of great interest, such as around storm track areas in the Indian Ocean, on the eastern side of Australia, and the region southeast of the Andes. Other regions and features that have not yet been studied in detail but show a large reduction in forecast error through the assimilation of Aeolus wind observations in the OSE are the polar regions, the Himalayan region, and parts of East Asia.

Appendix A

Contribution of journal publications to this dissertation

This dissertation includes results from a journal article. Table A.1 provides an overview of the contribution of the articles Martin et al. (2021a), Martin et al. (2022a) and Martin et al. (2022b) to this dissertation. The table lists all sections that are based on content from the publication.

Table A.1: *Contribution of journal publications to this dissertation.*

Martin et al. (2021a)	Martin et al. (2022a)	Martin et al. (2022b)
Sec. 3.1	Sec. 3.2	Sec. 3.2
Sec. 4.1	Sec. 5.1	Sec. 5.2
Sec. 4.2		
Sec. 4.3		

List of Abbreviations

Abbreviation	Description
3D-Var	Three-Dimensional Variational Data Assimilation
4D-Var	Four Dimensional Variational Data assimilation
A-TReC	Atlantic THORPEX Regional Campaign
A2D	ALADIN Airborne Demonstrator
ACCD	Accumulation Charge-Coupled Devices
ADM	Atmospheric Dynamics Mission
AEJ	African Easterly JET
ALADIN	Atmospheric Laser Doppler Instrument
AMV	Atmospheric Motion Vector
ASCAT	Advanced SCATterometer
ATOVS	Advanced TIROS Operational Vertical Sounder
BS	Beam Slitter
CCD	Charge-Coupled Device
COSMO	COnsortium for Small-scale MOdeling
COSMO-DE	COSMO limited-area model for Germany
CP	Commissioning Phase
DISC	Aeolus Data Innovation and Science Cluster
DLR	Deutsches Zentrum für Luft- und Raumfahrt
DUDE	Down Under Dark Experiment
DWD	Deutscher Wetterdienst
DWL	Doppler Wind Lidar
EADS	European Aeronautic Defence and Space Company
ECMWF	European Centre for Medium-Range Weather Forecast
EKF	Extended Kalman Filter
EnKF	Ensemble Kalman Filter
ENSO	El Niño-Southern Oscillation
ERA5	ECMWF Reanalysis 5th Generation
ESA	European Space Agency
ET	extratropical transition
ETKF	Ensemble Transform Kalman Filter
EUMETSAT	European Organisation for the Exploitation of Meteorological Satellites
EVAA	Experimental Validation and Assimilation of Aeolus observation
FWHM	Full-Width at Half Maximum
GCOS	Global Climate Observing System
GOS	Global Observing System
GRUAN	GCOS Reference Upper-Air Network

HLOS	Horizontal Line-Of-Sight
ICON	Icosahedral Nonhydrostatic global model
ICON-LEM	ICON Large Eddy Model
IFS	Integrated Forecast System
ITCZ	InterTropical Convergence Zone
KF	Kalman Filtering
L2B	level-2B
LAWS	Laser Atmospheric Wind Sounder
LETKF	Local Ensemble Transform Kalman Filter
LOS	Line-Of-Sight
MAD	Median Absolute Deviation
MJO	Madden-Julian-Oscillation
MPI-M	Max Planck Institute for Meteorology
NASA	National Aeronautics and Space Administration
NCEP	National Centers for Environmental Prediction
NMC	National Meteorological Center
NRL	Naval Research Laboratory
NRT	Near-Real-Time
NWP	Numerical Weather Prediction
OI	Optimum Interpolation
OSE	Observing System Experiment
PBL	Planetary Boundary Layer
PDGS	Payload Data Ground Segment
QBO	Quasi-Biennial Oscillation
T-PARC	THORPEX Pacific Asian Regional Campaign
TEJ	Tropical Easterly Jet
THORPEX	The Observing System Research and Predictability Experiment
TIROS	Television Infra-red Observing System
TRO	Transmit-Receive Optics
UV	Ultraviolet
VarQC	Variational Quality Control
WMO	World Meteorological Organization
WRF	Weather Research and Forecasting Model

List of Figures

Bibliography

Anstey, J. A., T. P. Banyard, N. Butchart, L. Coy, P. A. Newman, S. Osprey, and C. J. Wright, 2021: Prospect of Increased Disruption to the QBO in a Changing Climate. *Geophysical Research Letters*, **48 (15)**, e2021GL093 058, doi:10.1029/2021GL093058.

Anstey, J. A. and T. G. Shepherd, 2014: High-latitude influence of the quasi-biennial oscillation. *Quarterly Journal of the Royal Meteorological Society*, **140 (678)**, 1–21, doi:10.1002/qj.2132.

Baars, H., A. Herzog, B. Heese, K. Ohneiser, K. Hanbuch, J. Hofer, Z. Yin, R. Engelmann, and U. Wandinger, 2020: Validation of Aeolus wind products above the Atlantic Ocean. *Atmospheric Measurement Techniques*, **13 (11)**, 6007–6024, doi:10.5194/amt-13-6007-2020.

Baker, W. E., G. D. Emmitt, F. Robertson, R. M. Atlas, J. E. Molinari, D. A. Bowdle, J. Paegle, R. M. Hardesty, R. T. Menzies, T. N. Krishnamurti, R. A. Brown, M. J. Post, J. R. Anderson, A. C. Lorenc, and J. McElroy, 1995: Lidar-Measured Winds from Space: A Key Component for Weather and Climate Prediction. *Bulletin of the American Meteorological Society*, **76 (6)**, 869 – 888, doi:10.1175/1520-0477(1995)076<0869:LMWFSA>2.0.CO;2.

Baldwin, M. P., L. J. Gray, T. J. Dunkerton, K. Hamilton, P. H. Haynes, W. J. Randel, J. R. Holton, M. J. Alexander, I. Hirota, T. Horinouchi, D. B. A. Jones, J. S. Kinnersley, C. Marquardt, K. Sato, and M. Takahashi, 2001: The quasi-biennial oscillation. *Reviews of Geophysics*, **39 (2)**, 179–229, doi:10.1029/1999RG000073.

Bauer, P., A. Thorpe, and G. Brunet, 2015: The quiet revolution of numerical weather prediction. *Nature*, **525 (7567)**, 47–55, doi:10.1038/nature14956.

Bedka, K. M., A. R. Nehrir, M. Kavaya, R. Barton-Grimley, M. Beaubien, B. Carroll, J. Collins, J. Cooney, G. D. Emmitt, S. Greco, S. Kooi, T. Lee, Z. Liu, S. Rodier, and G. Skofronick-Jackson, 2021: Airborne lidar observations of wind, water vapor, and aerosol profiles during the NASA Aeolus calibration and validation (Cal/Val) test flight campaign. *Atmospheric Measurement Techniques*, **14 (6)**, 4305–4334, doi:10.5194/amt-14-4305-2021.

Berbery, E. H. and V. R. Barros, 2002: The hydrologic cycle of the la plata basin in south america. *Journal of Hydrometeorology*, **3 (6)**, 630 – 645, doi:10.1175/1525-7541(2002)003<0630:THCOTL>2.0.CO;2.

Bishop, C. H., B. J. Etherton, and S. J. Majumdar, 2001: Adaptive Sampling with the Ensemble Transform Kalman Filter. Part I: Theoretical Aspects. *Monthly Weather Review*, **129 (3)**, doi:10.1175/1520-0493(2001)129<0420:ASWTET>2.0.CO;2.

Borne, M., P. Knippertz, M. Weissmann, A. Martin, M. Rennie, and A. Cress, 2022: Impact of Aeolus wind lidar observations on the representation of the West African monsoon circulation in the ECMWF and DWD modeling systems.

Bouttier, F. and G. Kelly, 2001: Observing-system experiments in the ECMWF 4D-Var data assimilation system. *Quarterly Journal of the Royal Meteorological Society*, **127 (574)**, 1469–1488, doi:10.1002/qj.49712757419.

Burgers, G., P. J. Van Leeuwen, and G. Evensen, 1998: On the Analysis Scheme in the Ensemble Kalman Filter. *Monthly Weather Review*, **126**, 1719–1724, doi:10.1175/1520-0493(1998)126<1719:ASITEK>2.0.CO;2.

Chapnik, B., G. Desroziers, F. Rabier, and O. Talagrand, 2004: Properties and first application of an error-statistics tuning method in variational assimilation. *Quarterly Journal of the Royal Meteorological Society*, **130 (601)**, 2253–2275, doi:10.1256/qj.03.26.

Courtier, P., P. Gauthier, and F. Rabier, 1992: Study of preparation for the use of Doppler wind lidar information in meteorological assimilation systems. **ESA CR(P)-3453**.

Cress, A. and W. Wergen, 2001: Impact of profile observations on the German Weather Service's NWP system. *Meteorologische Zeitschrift*, **10 (2)**, 91–101, doi:10.1127/0941-2948/2001/0010-0091.

Desroziers, G., L. Berre, B. Chapnik, and P. Poli, 2005: Diagnosis of observation, background and analysis-error statistics in observation space. *Quarterly Journal of the Royal Meteorological Society*, **131 (613)**, 3385–3396, doi:10.1256/qj.05.108.

Desroziers, G. and S. Ivanov, 2001: Diagnosis and adaptive tuning of observation-error parameters in a variational assimilation. *Quarterly Journal of the Royal Meteorological Society*, **127 (574)**, 1433–1452, doi:10.1002/qj.49712757417.

Dirksen, R., M. Sommer, F. Immler, D. Hurst, R. Kivi, and H. Vömel, 2014: Reference quality upper-air measurements: GRUAN data processing for the Vaisala RS92 radiosonde. *Atmospheric Measurement Techniques*, **7 (12)**, 4463–4490, doi:10.5194/amtd-7-3727-2014.

Doviak, R. J. and D. S. Zrnić, 1993: *Doppler Radar and Weather Observations (Second Edition)*. Academic Press, doi:10.1016/B978-0-12-221422-6.50019-X.

ESA, 1989: Laser Sounding from Space. **ESA SP-1108**.

ESA, 1995: ESA Doppler Wind Lidar Workshop. **ESA WPP-05**, 312 pp.

ESA, 1999: Atmospheric dynamics mission. Mission Selection Rep. **ESA SP-1233(4)**.

ESA, 2008: ADM-Aeolus Science Report. **ESA SP-1311**, 121 p., URL `https://earth.esa.int/documents/10174/1590943/AEOL002.pdf,`.

ESA, 2016: ADM-Aeolus Mission Requirements Documents. **ESA EOP-SM/2047**, 57 p., URL `http://esamultimedia.esa.int/docs/EarthObservation/ADM-Aeolus_MRD.pdf`.

Evensen, G., 1994: Sequential data assimilation with a nonlinear quasi-geostrophic model using Monte Carlo methods to forecast error statistics. *Journal of Geophysical Research: Oceans*, **99 (C5)**, 10 143–10 162, doi:10.1029/94JC00572.

Eyre, J. R., S. J. English, and M. Forsythe, 2020: Assimilation of satellite data in numerical weather prediction. Part I: The early years. *Quarterly Journal of the Royal Meteorological Society*, **146 (726)**, 49–68, doi:10.1002/qj.3654.

Folger, K. and M. Weissmann, 2014: Height correction of Atmospheric Motion Vectors using satellite lidar observations from CALIPSO. *Journal of Applied Meteorology and Climatology*, **53 (7)**, 1809–1819, doi:10.1175/JAMC-D-13-0337.1.

Frehlich, R. and R. Sharman, 2004: Estimates of Turbulence from Numerical Weather Prediction Model Output with Applications to Turbulence Diagnosis and Data Assimilation. *Monthly Weather Review*, **132 (10)**, 2308 – 2324, doi:10.1175/1520-0493(2004)132<2308:EOTFNW>2.0.CO;2.

Garrett, K., H. Liu, K. Ide, R. N. Hoffman, and K. E. Lukens, 2022: Optimization and impact assessment of Aeolus HLOS wind assimilation in NOAA's global forecast system. *Quarterly Journal of the Royal Meteorological Society*, **148 (747)**, 2703–2716, doi:10.1002/qj.4331.

Gaspari, G. and S. E. Cohn, 1999: Construction of correlation functions in two and three dimensions. *Quarterly Journal of the Royal Meteorological Society*, **125 (554)**, 723–757, doi:10.1002/qj.49712555417.

Geer, A. J., P. Bauer, and P. Lopez, 2010: Direct 4D-Var assimilation of all-sky radiances. Part II: Assessment. *Quarterly Journal of the Royal Meteorological Society*, **136**, 1886–1905, doi:10.1002/qj.681.

Giorgetta, M. A., R. Brokopf, T. Crueger, M. Esch, S. Fiedler, J. Helmert, C. Hohenegger, L. Kornblueh, M. Köhler, E. Manzini, T. Mauritsen, C. Nam, T. Raddatz, S. Rast, D. Reinert, M. Sakradzija, H. Schmidt, R. Schneck, R. Schnur, L. Silvers, H. Wan, G. Zängl, and B. Stevens, 2018: ICON-A, the Atmosphere Component of the ICON Earth System Model: I. Model Description. *Journal of Advances in Modeling Earth Systems*, **10 (7)**, 1613–1637, doi:10.1029/2017MS001242.

Goody, R. M. and J. C. G. Walker, 1972: *Atmospheres*. Englewood Cliffs, N.J.: Prentice-Hall.

Grams, C. M., S. C. Jones, C. A. Davis, P. A. Harr, and M. Weissmann, 2013: The impact of typhoon jangmi (2008) on the midlatitude flow. part i: Upper-level ridgebuilding and modification of the jet. *Quarterly Journal of the Royal Meteorological Society*, **139 (677)**, 2148–2164, doi:10.1002/qj.2091.

Gray, L. J., J. A. Anstey, Y. Kawatani, H. Lu, S. Osprey, and V. Schenzinger, 2018: Surface impacts of the Quasi Biennial Oscillation. *Atmospheric Chemistry and Physics*, **18 (11)**, 8227–8247, doi:10.5194/acp-18-8227-2018.

Gray, W. M., 1984: Atlantic Seasonal Hurricane Frequency. Part I: El Niño and 30 mb Quasi-Biennial Oscillation Influences. *Monthly Weather Review*, **112 (9)**, 1649 – 1668, doi:10.1175/1520-0493(1984)112<1649:ASHFPI>2.0.CO;2.

Gray, W. M., J. D. Sheaffer, and J. A. Knaff, 1992: Influence of the Stratospheric QBO on ENSO Variability. *Journal of the Meteorological Society of Japan. Ser. II*, **70 (5)**, 975–995, URL `https://doi.org/10.2151/jmsj1965.70.5_975`.

Gu, Z. and W. Ubachs, 2014: A systematic study of Rayleigh-Brillouin scattering in air, N2, and O2 gases, journal = The Journal of Chemical Physics. **141 (10)**, 104 320, doi: 10.1063/1.4895130.

Hersbach, H., B. Bell, P. Berrisford, S. Hirahara, A. Horányi, J. Muñoz-Sabater, J. Nicolas, C. Peubey, R. Radu, D. Schepers, A. Simmons, C. Soci, S. Abdalla, X. Abellan, G. Balsamo, P. Bechtold, G. Biavati, J. Bidlot, M. Bonavita, G. De Chiara, P. Dahlgren, D. Dee, M. Diamantakis, R. Dragani, J. Flemming, R. Forbes, M. Fuentes, A. Geer, L. Haimberger, S. Healy, R. J. Hogan, E. Hólm, M. Janisková, S. Keeley, P. Laloyaux, P. Lopez, C. Lupu, G. Radnoti, P. de Rosnay, I. Rozum, F. Vamborg, S. Villaume, and J.-N. Thépaut, 2020: The ERA5 global reanalysis. *Quarterly Journal of the Royal Meteorological Society*, **146 (730)**, 1999–2049, doi:10.1002/qj.3803.

Hohenegger, C. and C. Schär, 2007: Predictability and Error Growth Dynamics in Cloud-Resolving Models. *Journal of the Atmospheric Sciences*, **64 (12)**, 4467 – 4478, URL `10.1175/2007JAS2143.1`.

Hólm, E., 2008: Assimilation Algorithms. ECMWF, URL `https://www.ecmwf.int/node/16931`.

Horel, J. D. and J. M. Wallace, 1981: Planetary-Scale Atmospheric Phenomena Associated with the Southern Oscillation. *Monthly Weather Review*, **109 (4)**, 813 – 829, URL `10.1175/1520-0493(1981)109<0813:PSAPAW>2.0.CO;2`.

Horányi, A., C. Cardinali, M. Rennie, and L. Isaksen, 2015a: The assimilation of horizontal line-of-sight wind information into the ECMWF data assimilation and forecasting system. Part I: The assessment of wind impact. *Quarterly Journal of the Royal Meteorological Society*, **141 (689)**, 1223–1232, doi:10.1002/qj.2430.

Horányi, A., C. Cardinali, M. Rennie, and L. Isaksen, 2015b: The assimilation of horizontal line-of-sight wind information into the ECMWF data assimilation and forecasting system. Part II: The impact of degraded wind observations. *Quarterly Journal of the Royal Meteorological Society*, **141 (689)**, 1233–1243, doi:10.1002/qj.2551.

Hoskins, B. J. and K. I. Hodges, 2005: A new perspective on southern hemisphere storm tracks. *Journal of Climate*, **18 (20)**, 4108 – 4129, doi:10.1175/JCLI3570.1.

Hoskins, B. J. and D. J. Karoly, 1981: The Steady Linear Response of a Spherical Atmosphere to Thermal and Orographic Forcing. *Journal of Atmospheric Sciences*, **38 (6)**, 1179 – 1196, URL 10.1175/1520-0469(1981)038<1179:TSLROA>2.0.CO;2.

Houtekamer, P. and H. Mitchell, 1998: Data Assimilation Using an Ensemble Kalman Filter Technique. *Monthly Weather Review - MON WEATHER REV*, **126**, 796–811, doi:10.1175/1520-0493(1998)126<0796:DAUAEK>2.0.CO;2.

Hunt, B., E. Kostelich, and I. Szunyogh, 2007: Efficient data assimilation for spatiotemporal chaos: A local ensemble transform Kalman filter. *Physica D: Nonlinear Phenomena*, **230 (1-2)**, 112–126, doi:10.1016/j.physd.2006.11.008.

Iwai, H., M. Aoki, M. Oshiro, and S. Ishii, 2021: Validation of Aeolus Level 2B wind products using wind profilers, ground-based Doppler wind lidars, and radiosondes in Japan. *Atmospheric Measurement Techniques*, **14 (11)**, 7255–7275, doi:10.5194/amt-14-7255-2021.

Iza, M., N. Calvo, and E. Manzini, 2016: The Stratospheric Pathway of La Niña. *Journal of Climate*, **29 (24)**, 8899 – 8914, URL 10.1175/JCLI-D-16-0230.1.

Janjic, T., N. Bormann, M. Bocquet, J. A. Carton, S. E. Cohn, S. L. Dance, S. N. Losa, N. K. Nichols, R. Potthast, J. A. Waller, and P. Weston, 2018: On the representation error in data assimilation. *Quarterly Journal of the Royal Meteorological Society*, **144 (713)**, 1257–1278, doi:10.1002/qj.3130.

Jones, S. C., P. A. Harr, J. Abraham, L. F. Bosart, P. J. Bowyer, J. L. Evans, D. E. Hanley, B. N. Hanstrum, R. E. Hart, F. Lalaurette, M. R. Sinclair, R. K. Smith, and C. Thorncroft, 2003: The Extratropical Transition of Tropical Cyclones: Forecast Challenges, Current Understanding, and Future Directions. *Weather and Forecasting*, **18 (6)**, 1052 – 1092, doi:10.1175/1520-0434(2003)018<1052:TETOTC>2.0.CO;2.

Jury, M. R., B. Pathack, and B. Parker, 1999: Climatic Determinants and Statistical Prediction of Tropical Cyclone Days in the Southwest Indian Ocean. *Journal of Climate*, **12 (6)**, 1738–1746, URL http://www.jstor.org/stable/26244387.

Kalnay, E., 2003: *Atmospheric modeling, data assimilation and predictability*. Cambridge University Press.

Keller, J. H., C. M. Grams, M. Riemer, H. M. Archambault, L. Bosart, J. D. Doyle, J. L. Evans, T. J. Galarneau, K. Griffin, P. A. Harr, N. Kitabatake, R. McTaggart-Cowan, F. Pantillon, J. F. Quinting, C. A. Reynolds, E. A. Ritchie, R. D. Torn, and F. Zhang, 2019: The Extratropical Transition of Tropical Cyclones. Part II: Interaction with the Midlatitude Flow, Downstream Impacts, and Implications for Predictability. *Monthly Weather Review*, **147 (4)**, 1077 – 1106, doi:10.1175/MWR-D-17-0329.1.

Kelly, G. and J.-N. Thépaut, 2007: Evaluation of the impact of the space component of the Global Observing System through Observing System Experiments. 16–28, doi:10.21957/ct50muxpx4.

Klein, P. M., P. A. Harr, and R. L. Elsberry, 2000: Extratropical Transition of Western North Pacific Tropical Cyclones: An Overview and Conceptual Model of the Transformation Stage, journal = Weather and Forecasting. **15 (4)**, 373 – 395, doi: 10.1175/1520-0434(2000)015<0373:ETOWNP>2.0.CO;2.

Krisch, I., N. P. Hindley, O. Reitebuch, and C. J. Wright, 2022: On the derivation of zonal and meridional wind components from Aeolus horizontal line-of-sight wind. *Atmospheric Measurement Techniques*, **15 (11)**, 3465–3479, doi:10.5194/amt-15-3465-2022.

Laloyaux, P., M. Bonavita, M. Dahoui, J. Farnan, S. Healy, E. Hólm, and S. T. K. Lang, 2020a: Towards an unbiased stratospheric analysis. *Quarterly Journal of the Royal Meteorological Society*, **146 (730)**, 2392–2409, doi:10.1002/qj.3798.

Laloyaux, P., M. Bonavita, M. Dahoui, J. Farnan, S. Healy, E. Hólm, and S. T. K. Lang, 2020b: Towards an unbiased stratospheric analysis. *Quarterly Journal of the Royal Meteorological Society*, **146 (730)**, 2392–2409, doi:10.1002/qj.3798.

London Economics Space Team, 2022: Aeolus Value of Information Study. URL `https://londoneconomics.co.uk/wp-content/uploads/2022/08/LE-ESA-FR-Final-Report-Aeolus-FINALS2C01072022.pdf`.

Lorenc, A. C., 1986: Analysis methods for numerical weather prediction. *Quarterly Journal of the Royal Meteorological Society*, **112 (474)**, 1177–1194, doi:10.1002/qj.49711247414.

Lorenc, A. C., T. Graham, I. Dharssi, B. Macpherson, N. Ingleby, and R. Lunnon, 1992: Preparation for the use of Doppler wind lidar information in meteorological assimilation systems. **ESA CR(P)-3454**.

Lux, O., C. Lemmerz, F. Weiler, U. Marksteiner, B. Witschas, S. Rahm, A. Geiß, and O. Reitebuch, 2020: Intercomparison of wind observations from the European Space Agency's Aeolus satellite mission and the ALADIN Airborne Demonstrator. *Atmospheric Measurement Techniques*, **13 (4)**, 2075–2097, doi:10.5194/amt-13-2075-2020.

Lux, O., C. Lemmerz, F. Weiler, T. Kanitz, D. Wernham, G. Rodrigues, A. Hyslop, O. Lecrenier, P. McGoldrick, F. Fabre, P. Bravetti, T. Parrinello, and O. Reitebuch, 2021: ALADIN laser frequency stability and its impact on the Aeolus wind error. *Atmospheric Measurement Techniques*, **14 (9)**, 6305–6333, doi:10.5194/amt-14-6305-2021.

Marseille, G., A. Stoffelen, and J. Barkmeijer, 2008a: A cycled sensitivity observing system experiment on simulated Doppler wind lidar data during the 1999 Christmas storm 'Martin'. *Tellus A: Dynamic Meteorology and Oceanography*, **60A (2)**, 249–260, doi: 10.1111/j.1600-0870.2007.00290.x.

Marseille, G., A. Stoffelen, and J. Barkmeijer, 2008b: Impact assessment of prospective spaceborne Doppler wind lidar observation scenarios. *Tellus A: Dynamic Meteorology and Oceanography*, **60A (2)**, 234–248, doi:10.1111/j.1600-0870.2007.00289.x.

Marseille, G. J., J. de Kloe, U. Marksteiner, O. Reitebuch, M. Rennie, and S. de Haan, 2022: NWP calibration applied to Aeolus Mie channel winds. *Quarterly Journal of the Royal Meteorological Society*, **148 (743)**, 1020–1034, doi:10.1002/qj.4244.

Martin, A., M. Weissmann, and A. Cress, 2022a: Impact of assimilating Aeolus observations in the global model ICON: A global statistical overview.

Martin, A., M. Weissmann, and A. Cress, 2022b: Investigation of links between dynamical scenarios and particularly high impact of Aeolus on NWP forecasts.

Martin, A., M. Weissmann, O. Reitebuch, M. Rennie, A. Geiß, and A. Cress, 2021a: Validation of Aeolus winds using radiosonde observations and numerical weather prediction model equivalents. *Atmospheric Measurement Techniques*, **14 (3)**, 2167–2183, doi:10.5194/amt-14-2167-2021.

Martin, Z., S. W. Son, A. Butler, H. Hendon, H. Kim, A. Sobel, S. Yoden, and C. Zhang, 2021b: The influence of the quasi-biennial oscillation on the Madden–Julian oscillation. *Nature Reviews Earth & Environment*, **2**, 477–489, doi:10.1038/s43017-021-00173-9.

Parrish, D. F. and J. C. Derber, 1992: The National Meteorological Center's Spectral Statistical-Interpolation Analysis System. *Monthly Weather Review*, **120 (8)**, 1747 – 1763, doi:10.1175/1520-0493(1992)120<1747:TNMCSS>2.0.CO;2.

Pourret, V., M. Šavli, J. Mahfouf, D. Raspaud, A. Doerenbecher, H. Bénichou, and C. Payan, 2022: Operational assimilation of Aeolus winds in the Météo-France global NWP model ARPEGE. *Quarterly Journal of the Royal Meteorological Society*, **n/a (n/a)**, doi:10.1002/qj.4329.

Pu, Z., L. Zhang, and G. D. Emmitt, 2010: Impact of airborne Doppler wind lidar profiles on numerical simulations of a tropical cyclone. *Geophysical Research Letters*, **37 (5)**, doi:10.1029/2009GL041765.

Reitebuch, O., 2012a: The spaceborne wind lidar mission ADM-Aeolus. *Atmospheric Physics*, Springer, 815–827.

Reitebuch, O., 2012b: Wind lidar for atmospheric research. *Atmospheric Physics*, Springer, 487–507.

Reitebuch, O., C. Lemmerz, E. Nagel, U. Paffrath, Y. Durand, M. Endemann, F. Fabre, and M. Chaloupy, 2009: The Airborne Demonstrator for the Direct-Detection Doppler Wind Lidar ALADIN on ADM-Aeolus. Part I: Instrument Design and Comparison to Satellite Instrument. *Journal of Atmospheric and Oceanic Technology*, **26 (12)**, 2501 – 2515, doi:10.1175/2009JTECHA1309.1.

Reitebuch, O., C. Lemmerz, O. Lux, U. Marksteiner, S. Rahm, F. Weiler, B. Witschas, M. Meringer, K. Schmidt, D. Huber, I. Nikolaus, A. Geiss, M. Vaughan, A. Dabas, T. Flament, H. Stieglitz, L. Isaksen, M. Rennie, J. de Kloe, G. Marseille, A. Stoffelen, D. Wernham, T. Kanitz, A. Straume, T. Fehr, J. von Bismarck, R. Floberghagen, and T. Parrinello, 2020: Initial Assessment of the Performance of the First Wind Lidar in Space on Aeolus. *EPJ Web Conf.*, **237**, 01 010, doi:10.1051/epjconf/202023701010.

Rennie, M. and L. Isaksen, 2020: The NWP impact of Aeolus Level-2B winds at ECMWF. *Technical Memorandum ECMWF*, **(864)**, doi:10.21957/alift7mhr.

Rennie, M., L. Isaksen, F. Weiler, J. de Kloe, T. Kanitz, and R. Reitebuch, 2021: The impact of Aeolus wind retrievals on ECMWF global weather forecast. *Quarterly Journal of the Royal Meteorological Society*, 1–32, doi:10.1002/qj.4142.

Rennie, M., D. Tan, E. Andersson, A. Poli, P.and Dabas, D. Kloe, J., G.-J. Marseille, and A. Stoffelen, 2020: Aeolus Level-2B Algorithm Theoretical Basis Document. URL `https://earth.esa.int/eogateway/documents/20142/37627/Aeolus-L2B-Algorithm-ATBD.pdf`.

Rhodin, A., H. Anlauf, R. Potthast, H. Lange, T. Janjic-Pfander, S. Hollborn, C. Schraff, T. Steinert, A. Schomburg, E. Bauernschubert, A. Walter, M. Bender, A. Cress, R. Faulwetter, C. Köpken-Watts, M. Lange, G. Paul, H. Reich, K. Stephan, O. Stiller, S. May, M. Pondrom, U. Ulrich Blahak, L. Neef, L. U. S. Welzbacher, C. Bach, K. Khosravian, M. Weissmann, H. W. Bitzer, R. Gray, A. Perianez, J. Ambadan, E. Lange, S. Declair, D. Pingel, O. Schmid, and N. Fischer, 2022: Documentation of the Data Assimilation Coding Environment (DACE).

Riboldi, J., C. M. Grams, M. Riemer, and H. M. Archambault, 2019: A Phase Locking Perspective on Rossby Wave Amplification and Atmospheric Blocking Downstream of Recurving Western North Pacific Tropical Cyclones. *Monthly Weather Review*, **147 (2)**, 567 – 589, doi:10.1175/MWR-D-18-0271.1.

Rodwell, M. J., L. Magnusson, P. Bauer, P. Bechtold, M. Bonavita, C. Cardinali, M. Diamantakis, P. Earnshaw, A. Garcia-Mendez, L. Isaksen, E. Källén, D. Klocke, P. Lopez, T. McNally, A. Persson, F. Prates, and N. Wedi, 2013: Characteristics of Occasional Poor Medium-Range Weather Forecasts for Europe. *Bulletin of the American Meteorological Society*, **94 (9)**, 1393 – 1405, doi:10.1175/BAMS-D-12-00099.1.

Rogers, J. C., 1984: The Association between the North Atlantic Oscillation and the Southern Oscillation in the Northern Hemisphere. *Monthly Weather Review*, **112 (10)**, 1999 – 2015, URL `10.1175/1520-0493(1984)112<1999:TABTNA>2.0.CO;2`.

Ruppert, D. and D. S. Matteson, 2015: *Statistics and Data Analysis for Financial Engineering*. 2d ed., Springer, New York, NY, doi:10.1007/978-1-4939-2614-5.

Seidel, D. J., B. Sun, M. Pettey, and A. Reale, 2011: Global radiosonde balloon drift statistics. *Journal of Geophysical Research: Atmospheres*, **116 (D7)**, doi:10.1029/2010JD014891.

Selz, T. and G. C. Craig, 2015: Upscale Error Growth in a High-Resolution Simulation of a Summertime Weather Event over Europe. *Monthly Weather Review*, **143 (3)**, 813 – 827, URL `10.1175/MWR-D-14-00140.1`.

Selz, T., M. Riemer, and G. Craig, 2022: The transition from practical to intrinsic predictability of midlatitude weather. *Journal of the Atmospheric Sciences*, URL `10.1175/JAS-D-21-0271.1`.

Shepherd, T., I. Polichtchouk, R. Hogan, and A. Simmons, 2018: Report on Stratosphere Task Force. *ECMWF Technical Memoranda*, **(824)**, doi:10.21957/0vkp0t1xx.

Stoffelen, A., G. J. Marseille, F. Bouttier, D. Vasiljevic, S. de Haan, and C. Cardinali, 2006: ADM-Aeolus Doppler wind lidar Observing System Simulation Experiment. *Quarterly Journal of the Royal Meteorological Society*, **132 (619)**, 1927–1947, doi:10.1256/qj.05.83.

Tan, D. G. H., E. Andersson, M. Fisher, and L. Isaksen, 2007: Observing-system impact assessment using a data assimilation ensemble technique: application to the ADM–Aeolus wind profiling mission. *Quarterly Journal of the Royal Meteorological Society*, **133 (623)**, 381–390, doi:10.1002/qj.43.

Tan, D. G. H., E. Andersson, J. D. Kloe, G.-J. Marseille, A. Stoffelen, P. Poli, M.-L. Denneulin, A. Dabas, D. Huber, O. Reitebuch, P. Flamant, O. L. Rille, and H. Nett, 2008: The ADM-Aeolus wind retrieval algorithms. *Tellus A: Dynamic Meteorology and Oceanography*, **60 (2)**, 191–205, doi:10.1111/j.1600-0870.2007.00285.x.

Thépaut, J.-N., R. Hoffman, and P. Courtier, 1993: Interactions of Dynamics and Observations in a Four-Dimensional Variational Assimilation. *Monthly Weather Review*, **121**, doi:10.1175/1520-0493(1993)121<3393:IODAOI>2.0.CO;2.

van Leeuwen, P. J., 2016: Data Assimilation Training in collaboration with the ECMWF. Faculdade de Engenharia da Universidade do Porto, URL `http://www.met.reading.ac.uk/~darc/training/ecmwf_collaborative_training/da_methods2016`.

Šavli, M., J. de Kloe, G.-J. Marseille, M. Rennie, N. Žagar, and N. Wedi, 2019: The prospects for increasing the horizontal resolution of the Aeolus horizontal line-of-sight wind profiles. *Quarterly Journal of the Royal Meteorological Society*, **145 (725)**, 3499–3515, doi:10.1002/qj.3634.

Šavli, M., V. Pourret, C. Payan, and J.-F. Mahfouf, 2021: Sensitivity of Aeolus HLOS winds to temperature and pressure specification in the L2B processor. *Atmospheric Measurement Techniques*, **14 (6)**, 4721–4736, doi:10.5194/amt-14-4721-2021.

Žagar, N., 2004: Assimilation of Equatorial Waves by Line-of-Sight Wind Observations. *Journal of the Atmospheric Sciences*, **61 (15)**, 1877 – 1893, doi:10.1175/1520-0469(2004)061<1877:AOEWBL>2.0.CO;2.

Žagar, N., N. Gustafsson, and E. Källén, 2004a: Dynamical response of equatorial waves in four-dimensional variational data assimilation. *Tellus A: Dynamic Meteorology and Oceanography*, **56 (1)**, 29–46, doi:10.3402/tellusa.v56i1.14389.

Žagar, N., N. Gustafsson, and E. Källén, 2004b: Variational data assimilation in the tropics: The impact of a background-error constraint. *Quarterly Journal of the Royal Meteorological Society*, **130 (596)**, 103–125, doi:10.1256/qj.03.13.

Weiler, F., M. Rennie, T. Kanitz, L. Isaksen, E. Checa, J. de Kloe, N. Okunde, and O. Reitebuch, 2021: Correction of wind bias for the lidar on board Aeolus using telescope temperatures. *Atmospheric Measurement Techniques*, **14 (11)**, 7167–7185, doi:10.5194/amt-14-7167-2021.

Weiler, F., T. Kanitz, D. Wernham, M. Rennie, D. Huber, M. Schillinger, O. Saint-Pe, R. Bell, T. Parrinello, and O. Reitebuch, 2020: Characterization of dark current signal

measurements of the ACCDs used on-board the Aeolus satellite. *Atmospheric Measurement Techniques Discussions*, 1–39, doi:10.5194/amt-2020-458.

Weissmann, M., R. Busen, A. Dörnbrack, S. Rahm, and O. Reitebuch, 2005: Targeted Observations with an Airborne Wind Lidar. *Journal of Atmospheric and Oceanic Technology*, **22**, 1706–1719, doi:10.1175/JTECH1801.1.

Weissmann, M. and C. Cardinali, 2007: Impact of airborne Doppler lidar observations on ECMWF forecasts. *Quaterly Journal of the Royal Meteorological Society*, **133**, 107–116, doi:10.1002/qj.16.

Weissmann, M., R. H. Langland, C. Cardinali, P. M. Pauley, and S. Rahm, 2012: Influence of airborne Doppler wind lidar profiles near Typhoon Sinlaku on ECMWF and NOGAPS forecasts. *Quaterly Journal of the Royal Meteorological Society*, **138**, 118–130, doi:10.1002/qj.896.

Weitkamp, C., 2005: *Lidar: range-resolved optical remote sensing of the atmosphere*, Vol. 102. Springer Science & Business.

Wirth, V., M. Riemer, E. K. M. Chang, and O. Martius, 2018: Rossby Wave Packets on the Midlatitude Waveguide—A Review. *Monthly Weather Review*, **146 (7)**, 1965 – 2001, doi:10.1175/MWR-D-16-0483.1.

Witschas, B., C. Lemmerz, A. Geiß, O. Lux, U. Marksteiner, S. Rahm, O. Reitebuch, and F. Weiler, 2020: First validation of Aeolus wind observations by airborne Doppler Wind Lidar measurements. *Atmospheric Measurement Techniques*, **13 (5)**, 2381–2396, doi:10.5194/amt-13-2381-2020.

Witschas, B., C. Lemmerz, and O. Reitebuch, 2012: Horizontal lidar measurements for the proof of spontaneous Rayleigh–Brillouin scattering in the atmosphere. *Appl. Opt.*, **51 (25)**, 6207–6219, doi:10.1364/AO.51.006207.

WMO, 1996: Guide to Meteorological Instruments and Methods of Observation - 6th edition. **WMO-No. 8**, 681 pp.

WMO, 1998: Preliminary Statement of Guidance Regarding How Well Satellite Capabilities Meet WMO User Requirements in Several Applications Areas. *WMO Satellite Reports SAT-21*, **WMO/TD No 913**.

WMO, 2012: WIGOS: WMO Integrated Global Observing System; Final report of the Fifth WMO Workshop on the Impact of Various Observing Systems on Numerical Weather Prediction. *WMO Tech. Rep.*, **2012-1**, 23 pp.

Zängl, G., D. Reinert, P. Rípodas, and M. Baldauf, 2015: The ICON (ICOsahedral Non-hydrostatic) modelling framework of DWD and MPI-M: Description of the non-hydrostatic dynamical core. *Quarterly Journal of the Royal Meteorological Society*, **141 (687)**, 563–579, doi:10.1002/qj.2378.

Danksagung

Allen voran möchte ich mich bei meinem Doktorvater Martin Weissmann bedanken. Lieber Martin, Danke für vier Jahre stete Unterstützung - sowohl auf fachlich als auch auf menschlicher Ebene. Ich schätze die Ratschläge die du mir mitgegeben hast, die Diskussionen mit Dir und vor allem Deine motivierenden Worte sehr. Die Arbeit mit Dir hat mir immer sehr viel Freude bereitet. Danke, für die tollen Erfahrungen und Alles was ich durch Dich lernen durfte und vor allem, dass du mich mit an die Universität Wien genommen hast. Ich habe die Zeit in dieser wundervollen Stadt sehr genossen!

Ein besonderer Dank gilt der gesamten Aeolus Community - vor allem den Aeolus Mitarbeiter:innen der ESA, des ECMWF, DLR und natürlich dem kompletten EVAA Team. Die Konferenzen mit Euch waren eine wunderbare Erfahrung. Unsere Treffen und Gespräche haben mir immer sehr viel Input und Motivation gegeben. Besonders hervorheben möchte ich an dieser Stelle Oliver Reitebuch und Alexander Geiss. Lieber Oliver und lieber Alex, vielen Dank, dass ihr mir immer mit Rat und Tat zur Seite gestanden habt und stets ein offenes Ohr und so viel Interesse an meiner Arbeit gezeigt habt! Die wertvollen Kommentare und Vorschläge von Euch haben mich immer sehr weitergebracht. Ein weiterer großer Dank geht an Alexander Cress vom DWD und Michael Rennie vom ECMWF für die Bereitstellung von Experimentdaten und wichtigen Informationen zu ihrer Verwendung und Interpretation.

Meinem Zweitgutachter, George Craig, möchte ich sehr für die hilfreichen Ratschläge, sowie für die Begutachtung dieser Doktorarbeit danken.

Ein großer Dank gilt all meinen Kolleg:innen, Büroplatznachbar:innen und Korrekturleser:innen in München, Wien und Karlsruhe: Leonhard, Stefan, Theresa, Tobi, Philipp, Stefano, Maurus, Lukas, Martin und Kathi - um nur einige zu nennen. Ihr habt alle einen so wichtigen Beitrag zu dieser Arbeit und vor allem einem stets angenehmen Arbeitsalltag gleistet. Es hat immer Spaß gemacht mit Euch zu diskutieren, zu grübeln und vor allem zu lachen - auch außerhalb der Uni. Liebe Barbara, Deine unbeschwerte und so herzlich ehrliche Art hat mich während meiner Zeit in München immer freudig gestimmt.

Zu guter Letzt, möchte ich mich bei der seelisch größten Stütze bedanken: meinen Eltern, meiner Schwester mit ihren drei kleinen Sonnenscheinen, meinen Freunden und dem wunderbarsten Menschen, Merlin. Danke fürs da sein, fürs an mich glauben und unterstützen.

This doctoral thesis was carried out in the frame of the German Aeolus Calibration and Validation team EVVA (Experimental Validation and Assimilation of Aeolus observations) and funded by the German Federal Ministry for Economic Affairs and Energy (BMWi). The presented work includes preliminary data (not fully calibrated/validated) of the Aeolus mission that is part of the European Space Agency (ESA) Earth Explorer Program. This includes the wind products from before the public data release in May 2020. The processor development, improvement and product reprocessing preparation are performed by the Aeolus DISC (Data, Innovation and Science Cluster), which involves DLR, DoRIT, ECMWF, KNMI, CNRS, S&T, ABB and Serco, in close cooperation with the Aeolus PDGS (Payload Data Ground Segment).